PEDECIBA-BIOLOGÍA
Doctoral Thesis in Biological Sciences
Subarea Biophysics

NEW DEVELOPMENTS IN ELASTOGRAPHY APPLIED TO MUSCLE BIOMECHANICS

MSc. Gustavo Adolfo Grinspan Segal

Thesis advisor:
Dr. Nicolás Benech

Thesis co-advisors:
Dr. Liliam Fernandes de Oliveira
Dr. Andrés Pomi

Jury:

Dr. Carlo Biancardi (President)
Dr. Ruben Daniel Peluffo
Dr. Thomas Gallot

September 25, 2024
Montevideo, Uruguay.

INDEX

Acknowledgements

I would like to thank several people and institutions for supporting and making this work possible. All of them, from their respective places, were very important to carry out this work.

I thank my thesis advisors, Dr. Nicolás Benech, Dr. Andres Pomi, and Prof. Liliam Fernandes de Oliveira, for guiding me through this process and sharing all their experience and knowledge in their respective specialties. Their dedication to discussing ideas, planning the work, and constant support were fundamental to carrying out this work. I also thank the Laboratory of Ultrasound Acoustics of the Faculty of Sciences, for their support and confidence concerning this interdisciplinary line of research. To the Laboratory of Movement Analysis and Exercise Physiology of the Federal University of Rio de Janeiro, Brazil. Especially to Prof. Liliam Fernandes de Oliveira and Maria Clara Brandao, for their help, kindness, hospitality, and dedication in discussing ideas and working together, making the internships in their laboratory very fruitful and enjoyable. To all my coworkers of the Biophysics and Systems Biology Section of the Faculty of Sciences, for their teachings, opportunities, and unconditional support, which have greatly enriched me as a teacher and researcher. To the Scientific Research Sectorial Committee (CSIC-UdelaR), and the Postgraduate Academic Committee (CAP-UdelaR), for the financial support received for carrying out this work. To my family, my parents Sofia and Gabriel, and my sister Erika, for the unconditional support and love they have always given me. To my lifelong friends, Benja, Esteban, Diego, and Ilana, for their friendship, warmth, and human quality. To my wife, Lucila, for taking care of me, supporting me unconditionally and choosing me to be her life partner. Finally, to my children, Emilia and Bruno (whose birth we are awaiting with great happiness), for filling my life with love, sweetness, and fun.

I want to express my gratitude to all of you, without whom it would have been impossible to carry out this work, and even more, to go through all these years of career.

ABSTRACT

Skeletal muscle contraction is a complex phenomenon involving several biochemical, bioelectrical, and biomechanical processes. Such processes occur at different scales, from the micro to the macro level, given as a final result the force production. Electromyography and dynamometry have been the most widely used methods to study the biomechanical properties of skeletal muscle. More recently, elastography has begun to be applied to account for its mechanical properties. Thus, this technique, initially described as a complementary tool for the medical diagnosis of certain pathologies, has added a new dimension to the biomechanical study of this tissue. Particularly, it accounts for the skeletal muscle as a soft solid, thus enabling studying the different processes and physiological phenomena associated with the change of its shear elastic modulus.

In this context, the main goal of the present thesis is to provide new theoretical, practical, and methodological frameworks to continue delving into the study of muscle biomechanics through elastography. The text begins by introducing the main concepts related to structural and physiological aspects of muscle contraction. Furthermore, it addresses the principles on which elastography is based to model and measure the shear elasticity of skeletal muscle *in vivo* and non-invasively. Then, the load-sharing between the elbow flexor synergistic muscles is addressed through the characterization of the dynamics of the relative longitudinal deformation of each muscle, by combining the acousto-elasticity theory, the short-range stiffness principle, and the ligand-binding approach. This provides a new framework to assess skeletal muscle contraction, which involves macro and microscopic aspects of force production. Therefore, it was also incorporated into the development of a static optimization model to calculate the contributions of individual muscle forces to the total torque. In this regard, the thesis contributes significantly to this long-standing challenge in biomechanics.

On the other hand, the thesis also assessed the time-dependence of muscle synergism between the elbow flexors muscles. As the reference shear wave elastography methods are not suitable for this purpose, we designed a new version of a non-ultrasound surface wave elastography method (developed previously by our group at the Laboratory of Ultrasound Acoustics of the Faculty of Sciences (UdelaR)), which has a higher sampling rate and allows to measure in more than one muscle simultaneously. In this concern, the thesis shows how this new realization of such a method extends the current experimental conditions to perform elastographic measurements on skeletal muscle. This has the potential to widen the scope of elastography-driven research in biomechanics.

In summary, the thesis makes important contributions to muscle biomechanics and opens up future lines of research in this field. In this regard, the text concludes by describing the general conclusions and the perspectives for future studies, based on the findings and developments of the present work.

CHAPTER 1

INTRODUCTION TO SKELETAL MUSCLE STRUCTURE AND FUNCTION

1 – INTRODUCTION

Elastography comprises a non-invasive methodology for the study of the mechanical properties of materials. Particularly, in biomechanics, it has provided a valuable non-invasive/destructive alternative to classical stress-strain tests performed from muscle tissue biopsies. In this way, it has given a novel dimension to this field of study, becoming the reference methodology for the characterization of the mechanical properties of skeletal muscle in vivo. Thus, in this first Chapter, the fundamental aspects on which the field of muscle elastography is based will be addressed. In this sense, we will begin by describing the basic structural and functional aspects of the muscle related to the problems addressed in the thesis.

There are three types of muscle: skeletal muscle, cardiac muscle, and smooth muscle. Of these, skeletal muscle as a whole has the particularity of representing approximately 40% of body weight (Heymsfield et al., 2005), and is responsible for executing all voluntary movements of the body. It acts as a true biological machine, capable of converting the chemical energy derived from reactions between organic substrates and oxygen into mechanical work and heat. Its particular physiology and internal organization determine a series of exclusive characteristics of this tissue. In this sense, its most interesting property is the capacity to contract under electrical stimulation, derived from the control carried out by the voluntary nerves. This leads to important changes in its structure and mechanical properties, which during the last

century and up to the present, have been the subject of numerous investigations in different laboratories around the world.

2 - GENERAL STRUCTURE OF SKELETAL MUSCLE

The organizational hierarchy of skeletal muscle is determined by structures visible both in the range of definition of the human eye, as well as others whose visualization requires the use of the optical microscope (definition in the range of 0.2μm) or even electron microscopy (0.002μm). Such hierarchical levels are shown in Figure 1.1. As can be seen, the individual units that make up the muscle are the *muscle fibers*, each of which is a multinucleated cell. These fibers are arranged in *fascicles* of various sizes within the muscle. Connective tissue plays an important role in this regard, as it forms an inner lining that fills the spaces between the muscle fibers within each fascicle (*endomysium*). In turn, each fascicle is surrounded by a stronger connective tissue sheath (*perimysium*), and the entire muscle is surrounded by an even stronger sheath (*epimysium*). Thus, when muscle tissue is considered together with its adjacent connective tissues (*fasciae*), it is structurally analogous to a "fiber-reinforced composite material," which is a very common material in engineering. Therefore, muscle consists of an extracellular matrix made up of an active component (muscle fibers, which generate forces and support loads) and two passive components (the basal lamina and muscle fasciae) (Zatsiorsky and Prilutsky, 2012; Huijing, 1999).

Collectively, bundles of muscle fibers may extend from one end of the muscle to the other but often do so for only part of the total length of the muscle, finishing at tendons or other connective tissue intersections. Such fibers are elongated in shape and have a relatively constant diameter varying from 10-60μm (Fung, 1993). The length is generally a few millimeters and can reach a few centimeters in long muscles. The spatial arrangement of the fibers in the muscle can be quite variable, determining the *anisotropic*

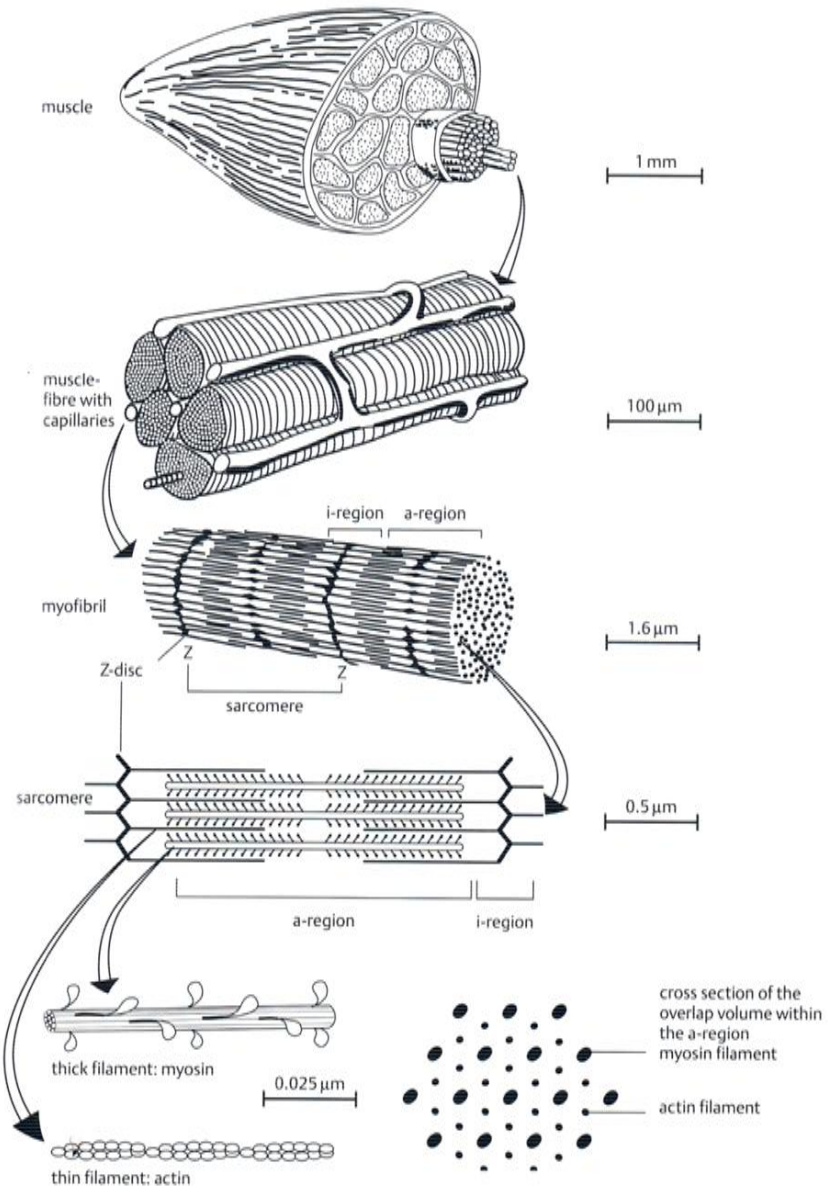

Figure 1.1. Organizational hierarchy of skeletal muscle. The fascicles forming the muscle are composed of bundles of muscle fibers. Most of the fibers' cytoplasm is occupied by myofibrils formed by actin and myosin protein myofilaments, which are the basis of the contractile machinery of the muscle. Connective tissue fills the space between the elements of each organizational level. Taken from Brinckmann et al. (2002).

character of this tissue. In this sense, when the fibers extend parallel to the longitudinal axis of the muscle, they are said to have a *parallel* architecture. This particular architecture corresponds to an anisotropy type known as *transverse isotropy*, according to which the properties of the tissue are uniform in any direction perpendicular to an axis of symmetry. On the other hand, when the fibers are arranged at a certain angle of

inclination, they have a *pennate* architecture (Fig. 1.2). According to some studies, the pennation angle can vary between 0° and 30° (Lieber, et al., 1990; Kawakami et al., 1998). Some muscles with this type of architecture are characterized by a large cross-sectional area and short fibers, while others have a small area and long fibers (Fig. 1.3).

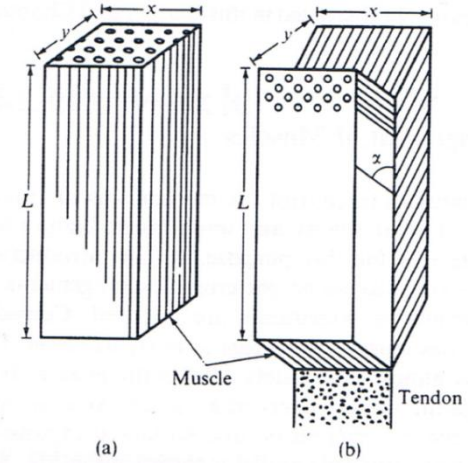

Figure 1.2. Representation of a muscle with parallel (a) and pennate (b) architecture. Adapted from Fung (1993).

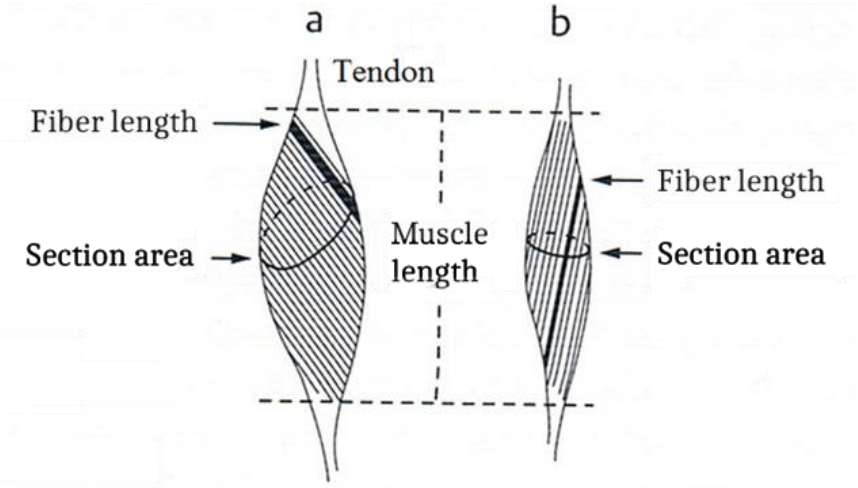

Figure. 1.3. Relationship between fibers' length and physiological section area of the muscle. a: muscle with short fibers and large section area. b: muscle with long fibers and a small physiological section. Adapted from Brinckmann et al. (2002).

These variations in the spatial structure of the fibers have important consequences for the muscles that possess them. Firstly, pennation determines different muscle responses to contraction. In this sense, muscles with parallel architecture tend to increase their lateral dimensions during contraction to maintain a constant volume,

while those with pennation do not experience such lateral expansion (Fung, 1993). On the other hand, the effective transfer of the work done by the fibers to the muscle also varies according to pennation. In the case of parallel muscles, they follow the linear behavior expected for a structure whose elements are arranged in series. In this sense, during contraction, the change in length of the muscle is equal to the change in length of the individual muscle fibers, just as the muscle force developed is equal to the sum of the force generated by each fiber. In contrast, the mechanics of the pennate muscles is more complicated. In this sense, the differential geometric arrangement of the fibers regarding the longitudinal axis of the muscle affects the relationship between the change in muscle length and that of the fibers. Likewise, if the pennation angle is ϕ only a fraction F' of the force F generated by the contraction of the fibers will be effectively transmitted in the direction of the tendon axis, as follows from the following expression:

$$|F'| = |F|.cos\,\phi \qquad (1.1)$$

Concerning the section area of the muscle and its association with the maximum force it can develop, this relationship is also influenced by the architecture of the fibers. To linearly correlate this quantity with the section area of the muscle, it is necessary to consider the physiological section area of the muscle, which is the sum of the areas of the individual fibers measured perpendicularly to their longitudinal direction (Figure 1.3) (Brinckmann et al., 2002).

When considering the level of organization comprising muscle fibers as the fundamental unit of muscle tissue, a classification of the different types of muscle fibers is usually described. This classification is based on the wide spectrum of contractile and metabolic properties that the fibers possess, being classified as fast or slow, oxidative or non-oxidative, glycolytic or non-glycolytic (Brooke and Kaiser, 1970; Punkt, 2002).

Table 1.1 details the three types of fibers often distinguished based on the above criteria. Likewise, the physiological properties of the muscle fibers determine the classification of the *motor units* (Kernell, 1986). The latter comprises the force-generating functional unit, constituted by an α-motor neuron and the muscle fibers innervated by it. Another interesting fact is the existence of regional differences according to the different types of muscle fibers. Thus, these define characteristic regions or domains, both along the longitudinal axis of the muscle and in its cross-section. Different studies have provided empirical data on this topic both in humans and other animal models (Johnson et al., 1973; Lexell et al., 1984, 1986; Punkt, 2002).

Table 1.1. Classification of muscle fibers according to their metabolism and contraction velocity.

Fiber type	Motor unit designation	Contraction velocity	Metabolic properties
Type I	Slow unit	Slow	Slow oxidative fiber
Type IIa	Fast fatigue-resistant unit	Fast	Fast oxidative glycolytic fibers
Type IIb	Fast-fatiguable unit	Fast	Fast glycolytic fibers

Beyond the metabolic differences, the ultrastructure underlying muscle fibers is common to all the fiber types described in Table 1. This ultrastructure is the fundamental basis of the process leading to muscle contraction and all the structural changes associated with it. Below, we will describe in detail the characteristics of this level of organization, as well as the complex molecular interactions that give rise to muscle contraction.

3 - MOLECULAR MECHANISM OF MUSCLE CONTRACTION

3.1 Ultrastructure of the muscle fibers

The fibers' cytoplasm is mostly occupied by a series of rows or *myofibrils*, each of them approximately 1 μm in diameter (Figure 1.4). These myofibrils show transverse

striation, determined by the presence of regions that are differentially stained with basic dyes such as hematoxylin. Thus, some areas stain weakly, receiving the name of *isotropic* or *I bands*. On the other hand, alternating with the I bands, other regions stain intensely, being called *anisotropic* or *A bands*. In the case of the I bands this division is due to a thin line called the *Z line*, while in the case of the A bands it is due to a clearer space called the *H band*. An interesting fact that occurs during muscle contraction, and that links the aforementioned structures, is that during this process the lateral dimensions of the I and H bands are reduced, while the A bands remain unchanged. In order to understand the basis of the transverse striation shown by the myofibrils, it is necessary to consider how they are constituted. In this sense, each myofibril is composed of a linear arrangement of protein *myofilaments*. These are in turn divided transversely by the Z line into discrete units arranged in series called *sarcomeres*. Such structures are of fundamental importance concerning the physiology and mechanics of muscle contraction since they constitute the anatomical and functional unit of the skeletal muscle. Each sarcomere has a length of approximately 2.5 μm, but its exact length depends on the force being exerted by the muscle and its state of excitation. Within each sarcomere, there are two clearly distinguishable types of myofilaments, thinner ones of around 5 nm in diameter and thicker ones of around 12 nm. The thinner filaments are *actin* molecules while the thicker ones are *myosin* molecules. These filaments are arranged in the sarcomere in such a way that the actin filaments are joined at one end to the Z line, while the other end is free and interdigitated with the myosin filaments. Thus, the transverse striation of the myofibrils can be understood: the A band corresponds to the band formed by the myosin filaments; the I bands are the regions of the actin filaments that do not overlap with the myosin filaments; the H bands are defined by the medial region of the A bands free of interdigitated actin filaments.

Another line, the *M-band*, is arranged transversely regarding the H-band, this being a thin strand interconnecting adjacent myosin filaments (Fung, 1993).

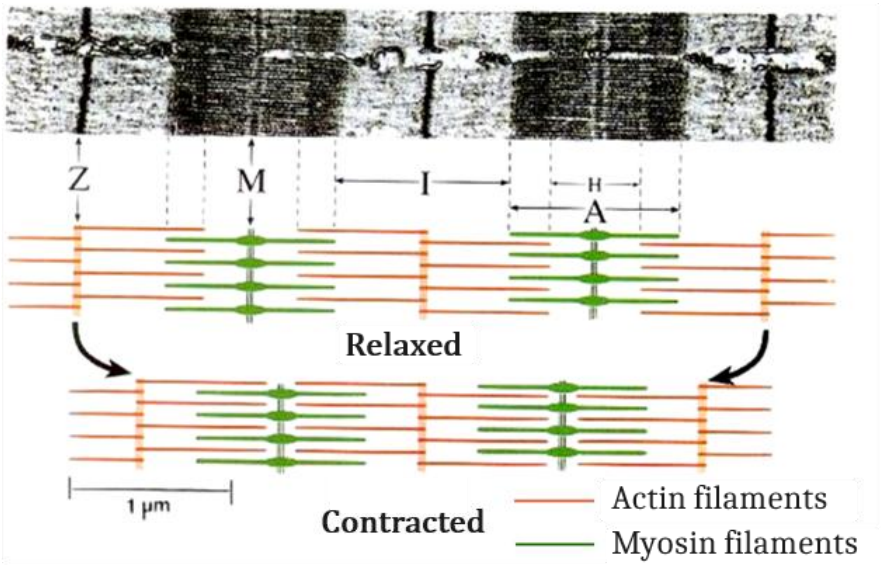

Figure. 1.4. Structure of myofibrils. The spatial arrangement of actin and myosin filaments along two sarcomeres is shown, noting that during contraction the I and H bands decrease in size, while the A band remains constant.

3.2 Molecular characteristics of the contractile filaments

3.2.1 Myosin filaments

The myosin filament is made up of 200 or more individual myosin molecules. As seen in Figure 1.5A, each of these molecules is made up of six polypeptide chains, two of which are heavy chains (molecular weight ~ 200,000 Da) and the other four light chains (molecular weight ~ 20,000 Da). The two heavy chains coil around each other in a spiral to form a double helix, which is called the *tail* of the myosin molecule. In turn, one end of each chain folds bilaterally to form a globular polypeptide structure called the myosin *head*. This structure plays an essential role in muscle contraction since it acts as an adenosine triphosphatase (ATPase) enzyme, cleaving the adenosine triphosphate (ATP) molecule and providing the resulting energy to the contraction process. Likewise, the four light chains are also part of the myosin heads, two in each.

These light chains help control the function of the head during muscle contraction (Guyton & Hall, 2016).

Figure 1.5B shows the clustering of myosin molecules that result in the assembly of the thick filament. As can be seen, the tails of the myosin molecules are grouped in the central portion to form the *body* of the filament, while the heads of the molecules are arranged on the sides of the filament. In addition, part of the body of each myosin molecule extends into the lateral region next to the head, forming an *arm* that separates the head from the body. The arms and heads that protrude in this manner are collectively referred to as *cross-bridges* (Guyton & Hall, 2016). These structures, which are distributed in all directions around the myosin filament, play a central role in the muscle contraction process and the associated force generation.

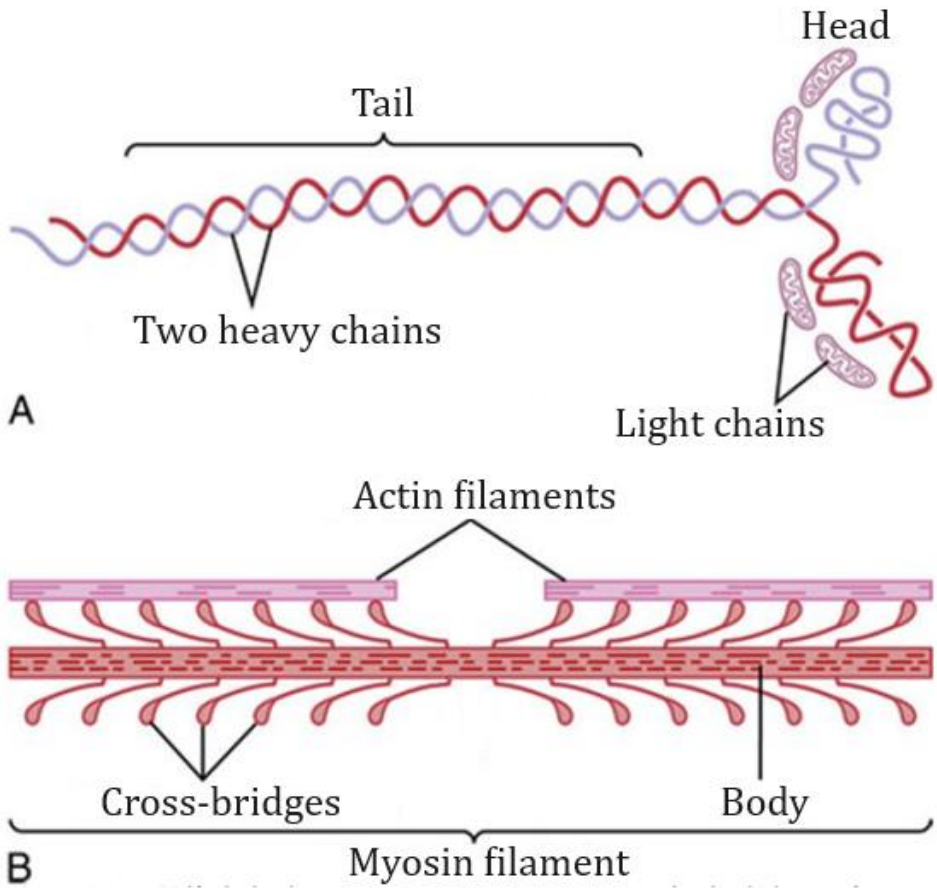

Figure. 1.5. A: Individual myosin molecule. B: Assembly of myosin molecules to form the myosin filament. Cross-bridges and interaction between myosin heads with adjacent actin filaments are shown. Taken from Guyton & Hal (2016).

3.2.2 Actin filaments

As shown in Figure 1.4, at the level of the sarcomeres, the bases of the actin filaments are strongly anchored at the Z-line, while the filament ends protrude in both directions into the spaces between the myosin filaments. These filaments are made up of two strands of the bicatenary F-actin protein, which in turn are polymers of the G-actin molecule. Like the myosin molecules, both strands are helically coiled. Each G-actin monomer is attached to an adenosine diphosphate (ADP) molecule, which is thought to constitute the *active sites* of the actin filaments with which the myosin cross-bridges interact to produce muscle contraction (Guyton & Hall, 2016).

The actin filament also contains the *tropomyosin* protein. These molecules are also helically coiled, arranging themselves around the F-actin helix. In the resting state, tropomyosin molecules coat the active sites of the actin filaments, inhibiting actin-myosin binding to produce muscle contraction. In turn, along with the tropomyosin molecules, there are other protein molecules called *troponin*. These molecules are complexes of three subunits, each of which has a specific function in the control of muscle contraction. Thus, *troponin I* has a high affinity for actin, *troponin T* for tropomyosin, and *troponin C* for calcium ions. This complex is thought to bind tropomyosin to actin, and the high affinity of troponin for calcium ions initiates the contraction process (Guyton & Hall, 2016). Figure 1.6 shows the previously discussed molecular details regarding the organization of actin filaments.

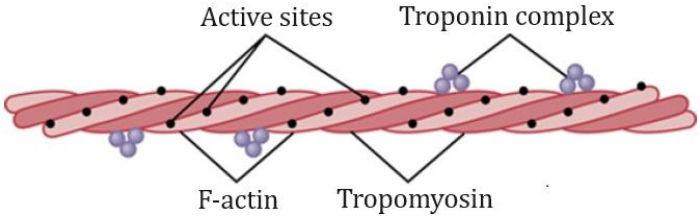

Figure. 1.6. Actin filament. The two strands of F-actin and the two strands of tropomyosin helically coiled together are observed, as well as the troponin complexes attached to the tropomyosin. Taken from Guyton & Hall (2016).

3.2.3 Activation and inhibition of actin filaments

Currently, it is thought that the troponin-tropomyosin complex inhibits the active sites of muscle actin filaments in the relaxed state. This inhibition would be accomplished by physically blocking the binding to the active sites. Thus, these sites cannot bind to the myosin filament heads to produce muscle contraction. This requires deactivation of the blocking effect of the troponin-tropomyosin complex, which is achieved by the presence of large amounts of calcium ions.

Although such an unblocking mechanism is not well understood, the current hypothesis is that when calcium ions combine with troponin C, the troponin complex undergoes a conformational change that would pull the tropomyosin molecule. This would move the tropomyosin molecule deeper into the groove between the two actin strands, thus uncovering the actin active sites (Guyton & Hall, 2016). This would enable the attraction of the myosin heads, whose ATPase activity would trigger the subsequent reactions that produce contraction. Although this mechanism is hypothetical, it highlights that the relationship between the troponin-tropomyosin complex and actin is calcium ion-dependent, which regulates the binding of actin active sites to myosin cross-bridges.

3.2.4 Interaction of activated actin filaments with cross-bridges and muscle contraction

Based on the structural and functional details previously analyzed, the theory of muscle contraction establishes that sarcomeres generate force through the interaction of actin and myosin filaments (Huxley, 1957, 1973, 1988; Huxley & Peachy, 1961). As soon as the actin filament is activated by calcium ions, the myosin heads are attracted to the actin active sites, thus determining the muscle contraction.

Although the precise mechanism by which this interaction between cross-bridges and actin produces contraction remains partly theoretical, one hypothesis for which

there is considerable data is the *sliding filament theory*. In that regard, Figure 1.7 shows the reversible binding of myosin heads according to that theory. When a head binds to an active point, this produces important changes at the level of intramolecular forces between the head and the myosin arm. This causes the head to move toward the arm, generating the *active stroke* that pulls the actin filament. Immediately after the displacement, the head automatically separates from the active site, recovering its original extended position. In this position, it combines with a new active site further down at the actin filament, a new active stroke is generated, and the actin filament advances another step (Guyton & Hall, 2016). In this manner, the successive union of the cross-bridges of the myosin filaments to the active points of the actin filament results in the reciprocal displacement of these filaments, which characterizes muscle contraction.

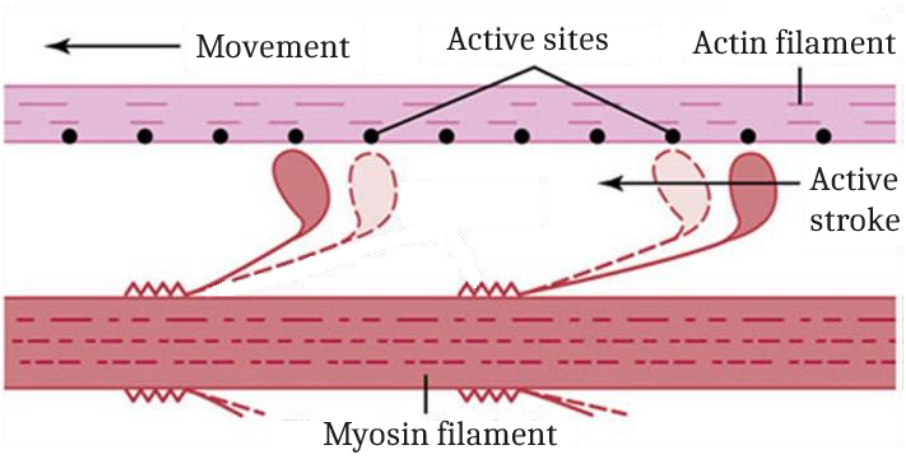

Figure. 1.7. Sliding filament mechanism of muscle contraction.

Thus, according to the theory of contraction, the shortening of the sarcomeres can only occur through the relative sliding of the myofilaments. The degree of their overlapping will be greater as the length of the muscle fiber decreases. Thus, the total shortening of a myofibril will be equal to the sum of the shortenings of the sarcomeres arranged in series. On the other hand, although at any moment of muscular activity we

can find cross-bridges attached to the actin filaments, separated from them or moving towards a new binding site, the generation of force at a given moment will depend exclusively on the number of active cross-bridges. The serial arrangement of the sarcomeres determines that the force generated by one unit is maintained and transmitted to the following units. Therefore, the force of the whole structure will be equal to the force of a single sarcomere. If the number of active cross-bridges is low, then the force developed will be low; if the number of active cross-bridges increases, the force will also do it (Brinckmann et al., 2002).

4 - TYPOLOGY OF MUSCULAR CONTRACTION

Skeletal muscles are designed to initiate movements, decelerate movements, resist external loads so that movement does not occur, and provide the organism with a substantial part of the heat it needs. In this sense, muscle activity can be static or dynamic. The former involves contraction while maintaining a constant muscle length. On the other hand, dynamic muscle activity is defined as contraction during which muscle length varies (Brinckmann et al., 2002). Concerning this, muscular contraction can be classified into three types, which we will detail below.

4.1 Isometric contraction

This type of muscle contraction is relevant in the framework of this thesis, since the results of the experiments and models described in Chapters 3, 4, and 5 account for it.

When a muscle develops force but its length remains constant and no movement occurs, the structure is in static equilibrium. This characterizes isometric contraction. Although there is no observable change in the length of the muscle-tendon complex, there is a shortening of the muscle fibers accompanied by a simultaneous elongation of the tendons. This determines that the total length of such a complex remains constant.

There is a relationship between the level of isometric force developed by the muscle and the type and proportion of activated motor units. This is based on research that sought, in the first place, to correlate the isometric force developed by the muscle with the physical characteristics of the axons recruited, and then to analyze the type of motor units that these axons innervate. In this sense, Henneman et al. (1965) observed that for low levels of isometric force, the axons recruited had the shortest axons and the lowest depolarization thresholds. On the other hand, as the force increased, the recruited axons were increasingly longer and had higher depolarization thresholds. This is now known as the *Henneman's size principle*. In later studies, Binder and Mendell (1990) showed that in general, short motor axons innervate slow motor units (Type I), and longer axons innervate fast motor units (Type IIa and IIb).

From these findings, the scheme shown in Figure 1.8 was proposed to explain the voluntary recruitment of motor units during isometric contraction. For low force levels, shorter motor axons with lower depolarization thresholds are activated first. Therefore, type I motor units are the earliest recruited. On the other hand, as the force level increases, most of the axons that follow them in length become activated, thus recruiting Type IIa units. During maximal effort, the longest axons are activated, thereby recruiting Type IIb fibers. This activation pattern seems reasonable since the most frequently activated motor units (Type I) are those that present the greatest resistance. On the other hand, the Type IIb motor units, whose activation frequency is much lower, present the least resistance. In addition to the above, the Type I units (which are the first to be recruited) develop the lowest tension, so that when contraction begins, little tension is generated. Thus, all of the above provide a mechanism that explains the physiological basis for the increase in tension during the isometric contraction (Brinckmann et al., 2002).

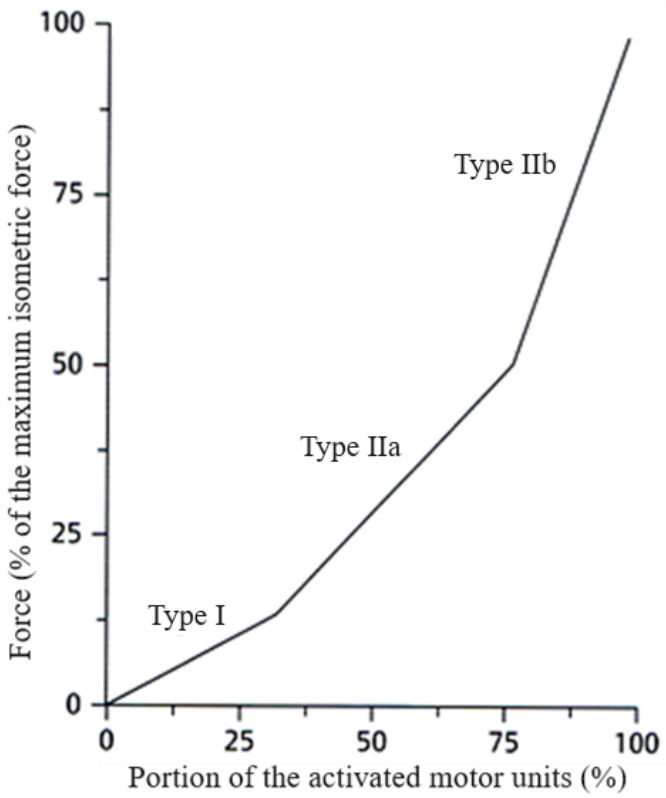

Figure. 1.8. Hanneman's size principle. Differential recruitment of the different types of motor units is observed regarding the level of isometric muscle strength. Taken from Brinckmann et al. (2002).

4.2 Concentric contraction

This type of contraction occurs when the muscle is able to shorten against a load, producing movement. The force developed under concentric muscle action is always less than the maximum isometric force, which is developed according to the optimal muscle length. The contraction velocity increases when the muscles work against small loads; when the load is reduced almost to zero, the muscle reaches its maximum contraction velocity (Hill, 1938). This speed is characteristic of each muscle and depends on the characteristics of the muscle architecture.

4.3 Eccentric contraction

If a muscle is activated in such a way that its length under an external load increases, the contraction is called *eccentric*. During this type of contraction the muscle stores elastic potential energy. Likewise, muscle force can far exceed the maximal

isometric force. The increase in force is due to the sum of active and passive resistive force. This passive force aims to restore muscle length when the muscle is stretched during activity and is a fundamental property for many daily movement patterns.

CHAPTER 2

MODELING AND MEASUREMENT OF THE MECHANICAL PROPERTIES OF SKELETAL MUSCLE

1 – INTRODUCTION

According to the classification usually given to solids in materials physics, skeletal muscle is a *soft solid*. This implies that its compressive elasticity is much greater than its shear elasticity. When a muscle is stretched beyond its resting length, it behaves like a deformable body. This means that the muscle is able to undergo appreciable changes in its shape due to the action of external forces, opposing a passive resistance to stretching. This term refers fundamentally to the opposition of resistance does not require the investment of metabolic energy. This produces a work that is stored in the body as elastic potential energy, thus determining an increase in its internal energy.

On the other hand, once the external force is removed, the muscle is able to recover its original size and shape, which reverts the increase in its internal energy. According to this, besides being deformable, the muscle is an elastic solid. Thus, elasticity is the mechanical property of certain materials to undergo reversible deformations when subjected to the action of external forces (Zatsiorsky and Prilutsky, 2012). Likewise, the muscle also presents nonlinear and viscoelastic behaviors, mainly attributable to the internal network of connective tissues and blood vessels that it possesses. In this sense, during small stretches, the fibers that compose this network become progressively tighter, until they can eventually become deformed as tension increases.

In this context, this Chapter will describe the elastic behavior of soft solids, of which skeletal muscle is one of the main exponents. Thus, emphasis will be placed on the models according to which the elastographic study of this tissue is theoretically framed. We will also describe the basic principles of shear wave elastography, which is

the reference elastographic methodology for the measurement of the mechanical properties of soft biological tissues. Finally, towards the end of the Chapter, we will review the state of the art of research in muscle biomechanics carried out with elastography, as well as the current challenges that motivate the present thesis.

2 – MECHANICAL PROPERTIES OF SOFT TISSUES: UNIDIMENSIONAL MODELS

2.1 Linear elasticity

Determining the elastic parameters of a soft solid must be carried out based on a rheological model of the material under study. Generally in elastography, the model used as a first approximation for estimating the elasticity of skeletal muscle is that of an elastic, linear, and isotropic medium (Benech, 2008). Therefore, we will dedicate the following paragraphs to explaining this model.

If considering a body subjected to an external extension force acting on a certain area of the body, this will experience a mechanical *tension* or *stress* given by the following expression:

$$\sigma = \mathrm{F}/\mathrm{A} \qquad (2.1)$$

where A is the cross-sectional area normal to the force. As can be seen from the corresponding dimensional analysis, σ is measured in N/m^2, i.e. pascals (Pa). When the cross-section is perpendicular to the direction of the force, the resulting stress is called *normal stress* or *compressive stress*, while when the force acts parallel to the cross-section it is called *shear stress*. On the other hand, the elongation resulting from the extension force acting on the body (*strain*) is defined as proportional to the initial length by the following dimensionless magnitude:

$$\varepsilon = d\mathrm{L}/\mathrm{L} \qquad (2.2)$$

where dL is the change in length and L is the initial length of the body. Thus, an elastic solid is characterized by fulfilling a linear relationship between the stress acting on the body and its corresponding deformation. Therefore, a stress-strain curve of this type of media typically shows that for low-stress values, the strain increases proportionally to the applied stress. This is represented by a straight line in the corresponding diagram. However, above a certain stress value called the "*elastic limit*", the relationship exhibits a non-linear behavior. The ratio of stress to strain in the linear part of the graph corresponds to the *modulus of elasticity* or *Young's modulus* "*E*" of the medium, which is measured in Pa (Figure 2.1). This magnitude characterizes the behavior of an elastic material according to the direction in which a force is applied. For a linear and isotropic elastic material, Young's modulus has the same value for tension as for compression, being a constant independent of the stress as long as it does not exceed the value of the elastic limit. The higher it is, the more stress is needed to produce a given stretch, which means that stiffer materials typically have a higher Young's modulus (Brinckmann et al., 2002).

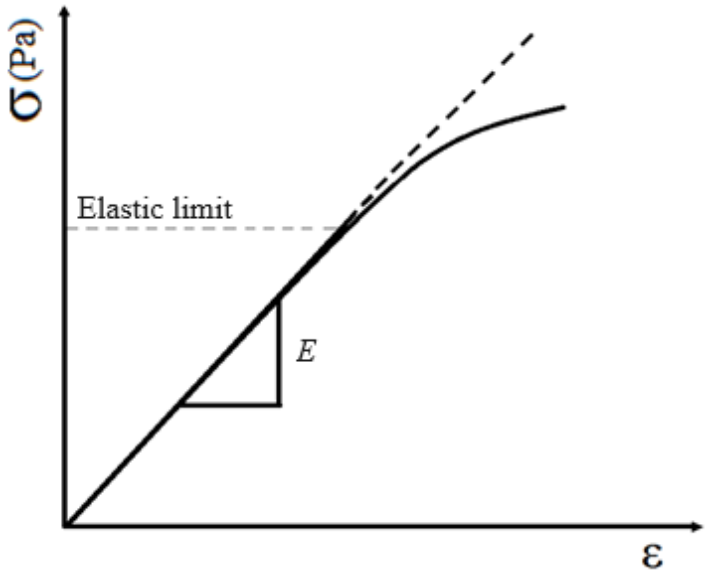

Figure 2.1. Typical stress-strain curve of linear elastic behavior. The slope of the graph in its linear part determines the Young's modulus "*E*" of the material. Beyond the "elastic limit," the behavior is nonlinear.

The law that explains the behavior of elastic solids is Hooke's law, whose expression in the case of a one-dimensional problem can be deduced from the linear part of Figure 2.1:

$$\sigma = E\varepsilon \qquad (2.3)$$

An alternative way to express Young's modulus is to use *Lamé's elastic constants*, λ and μ, representing the compressive and shear elasticities, respectively. Thus, the following expression is defined based exclusively on these constants (Landau and Lifshitz, 1970):

$$E = \mu\frac{(3\lambda + 2\mu)}{(\lambda + \mu)} \qquad (2.4)$$

The particular case where $\lambda >> \mu$ characterizes the soft solids. Among the most important exponents of this type of media are the soft biological tissues, such as skeletal muscle. From the relationship between Lamé's elastic constants for this type of media, their Young's modulus can be expressed as follows (Landau and Lifshitz, 1970):

$$E = \mu\frac{3\lambda+2\mu}{\lambda+\mu} \approx \mu\frac{3\lambda}{\lambda} = 3\mu \qquad (2.5)$$

This means that for soft tissues, such as skeletal muscle, Young's modulus is determined by the shear modulus of elasticity μ. In other words, the "hardness" in this type of tissue is determined by this parameter (Benech et al., 2012).

Another parameter to consider when dealing with elastic solids is the Poisson's modulus (v). It is usually used when the deformations on the material are large so that changes in its cross-sectional area cannot be neglected. In this way, the increase of stresses on the material is due to two interacting factors; the increase in the force and the reduction of the cross-sectional area. Thus, Poisson's modulus is used to quantify the

relative changes in transverse and axial stretching, and is related to Lamé's constants through the following expression (Benech et al., 2019):

$$v = \frac{\lambda}{2\lambda + \mu} \qquad (2.6)$$

In a soft solid $v \cong 1/2$.

2.2 Linear viscoelasticity

From the point of view of the physics of materials, in a relaxed state, the muscle is a *viscoelastic* material (Rack, 1966). This type of material typically exhibits a combination of the energy storage characteristics observed in elastic materials and the dissipation characteristics observed in viscous liquids. Thus, when these materials are subjected to external forces, they experience stresses that are derivative functions of stretching as a function of time (Rose, 1999).

As we have seen previously, Eq. (2.4) allows to calculate Young's modulus of an elastic solid from the elastic constants of Lamé λ and μ. However, materials that exhibit nonlinear and viscoelastic behavior, such as skeletal muscle, do not obey this equation. Figure 2.2 shows the typical stress-strain curve exhibited by this type of media. As can be seen, this curve can be divided into three regions: A-B, where there is an exponential increase in stress as strain increases; B-C, in which the relationship is practically linear; C-D, which shows the deviation from linearity for high strain levels (Fung, 1993). Of these regions, the A-B corresponds to the physiological range of the soft biological tissues. In this sense, it has been previously demonstrated that skeletal muscle exhibits increased rigidity as a mechanical response to increased stretching (Magnusson, 1998; Gajdosik, 2001). Meanwhile, regions B-C and C-D correspond to the additional resistance presented by the soft tissues, which operates as a safety factor (Fung, 1993).

As can also be seen in Figure 2.2, the representative value of Young's modulus for this type of media is estimated from the slope of the linear part of the graph (Fung, 1993).

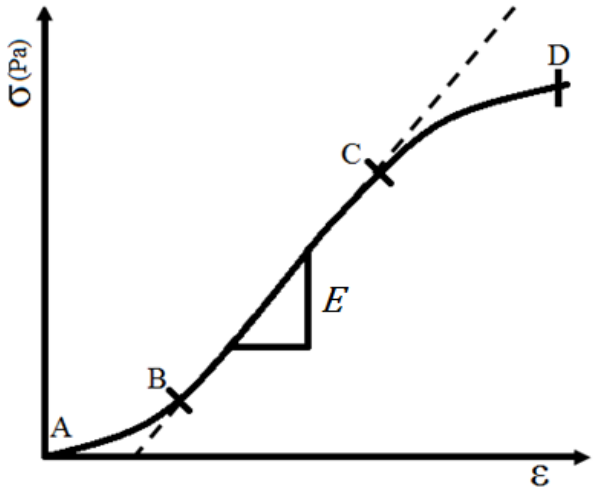

Figure 2.2. Typical stress-strain curve of a viscoelastic solid.

In addition to the typical stress-strain curve in Figure 2.2, the viscoelastic behavior of soft solids is also characterized by three main phenomena; (a) *creep*, (b) *stress relaxation*, (c) *hysteresis* (Fig. 2.3). The first manifests as an increase in the deformation of the body under a constant load, while the second manifests as a gradual decrease in the stress suffered by the body, also under a constant deformation over time. In the specific case of hysteresis, it manifests as the difference between the load and unload curves in a stress-strain cycle. Graphically, hysteresis is manifested as a loop in the stress-strain plot (called "*hysteresis loop*") and is defined as the ratio between the area of the loop and the area under the loading process curve (Fung, 1993; Zatsiorsky and Prilutsky, 2012). Such a phenomenon is due to the inability of the system to follow identical patterns after the application and withdrawal of a force. The area of such a loop represents the energy loss in the stretch-strain cycle, mainly due to the conversion of mechanical work into heat. It is important to note that while such a loop is quite small in tissues possessing elastin and collagen (e.g. tendons and ligaments), it is typically very large in skeletal muscle, denoting its greater viscoelasticity (Fung, 1993).

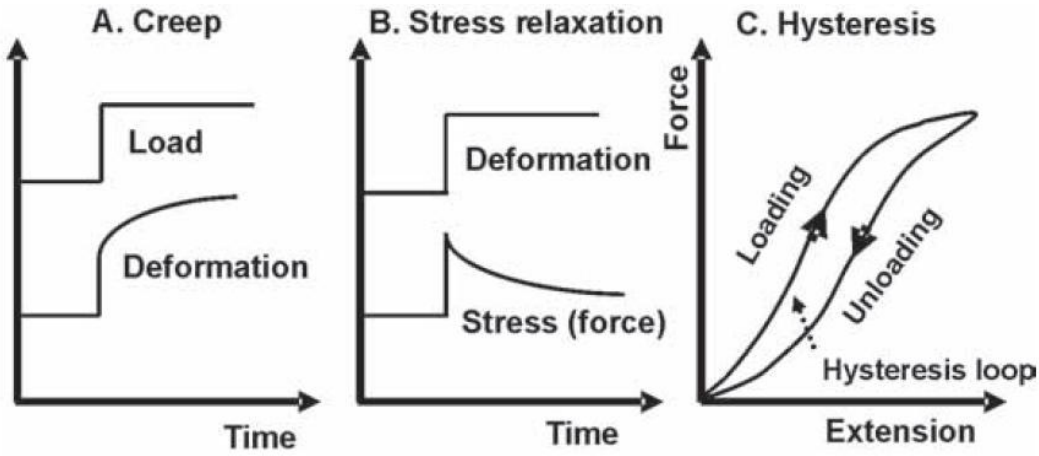

Figura 2.3. Main characteristics of the viscoelastic behavior of soft solids. Taken from Zatsiorsky et al. (2012).

2.3 Non-linear elasticity

As seen in Section 2.1, for a linear elastic material, there is always a constant relationship between the applied stress and the resulting strain, regardless of the magnitude of the stress and the strain. The stress-strain relation for such a material is, therefore, a straight line (Fig. 2.1), whose slope corresponds to the Young´s modulus of the media.

Any material not obeying the linear stress-strain relation described by Hooke's law (Ec. (2.3)) is said to behave as a non-linear elastic solid. In this regard, for such a type of media, the stress–strain relation may be written as (Fjær et al., 2008):

$$\sigma = E_1\varepsilon + E_2\varepsilon^2 + E_3\varepsilon^3 + \cdots \qquad (2.7)$$

This expression is a power series that captures the relationship between stress and strain when the behavior of the material cannot be described simply by a linear relationship. The first term of the series, $E_1\varepsilon$, represents the linear behavior of the material, being E_1 the Young's modulus introduced in Section 2.1. This term predominates when the deformation is small, and the material behaves as a linear elastic solid (see rounded area in Fig. 2.4). The quadratic term, $E_2\varepsilon^2$, introduces the first nonlinearity in the stress-strain relationship. This term becomes significant as the strain increases, indicating that

the relationship is not simply proportional and that the material response includes non-linear components. The cubic term, $E_3\varepsilon^3$, adds further non-linearities, describing a more complex material behavior. This term and those of higher order become important for large deformations when the material response diverges considerably from the linear behavior.

Figure 2.4 depicts a typical stress-strain curve of a non-linear elastic material. As can be seen, the ratio of stress to strain is not the same for all stresses. Therefore, Young´s modulus is no longer uniquely defined, not even for a specific stress level (Fjær et al., 2008). However, as mentioned above, Young's modulus of this type of material can be well approximated by Hook's law, in the case of small deformations. This is the range of deformations where the muscle operates during elasticity measurements at resting conditions. Some of the experiments in this thesis will be performed under such conditions.

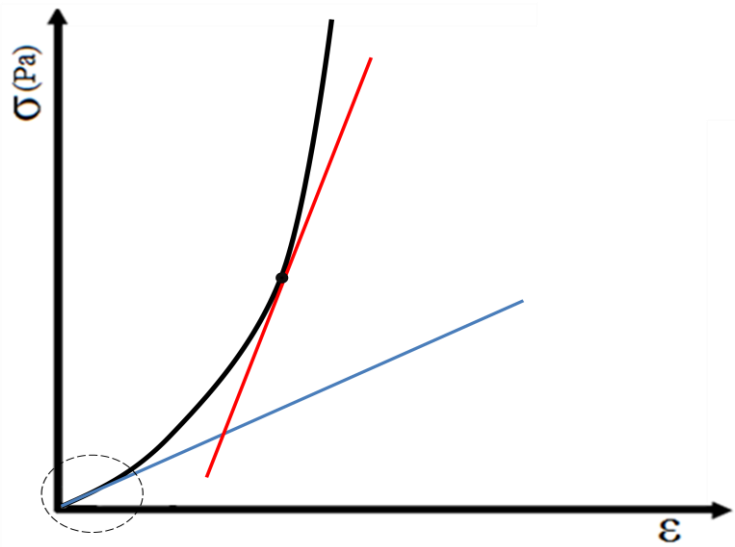

Figure 2.4. Typical stress-strain curve of non-linear elastic behavior. For low strains (dashed circle) the elastic behavior of the medium is according to Hook's law, and Young's modulus can be estimated from the slope of the blue line. For higher strains, the relationship between stress and strain is no longer unique for all stresses. As indicated by the red line, it is possible to obtain an instantaneous value of Young's modulus of the medium, by calculating the slope of the tangent line at different points of the stress-strain curve.

In the case of larger deformations in a non-linear elastic soft solid, the *instantaneous Young's modulus* at a specific point on the stress-strain curve can be calculated through the slope of the tangent line to that point (Fig. 2.4). In this way, the linear form of the stress-strain relations may be used far beyond the initial linear region. Thus, the Hooke's law may be written in a differential form (Fjær et al., 2008):

$$\Delta\sigma = E_{\tan}(\varepsilon)\Delta\varepsilon \qquad (2.8)$$

where $\Delta\sigma$ and $\Delta\varepsilon$ correspond to differential increments in stress and strain, respectively, and $E_{\tan}(\varepsilon)$ is the instantaneous value of Young's modulus. The above expression can represent a non-linear elastic material beyond the initial linear phase, subject to infinitesimal stresses, such as skeletal muscle during contraction. In this regard, several of the experiments to be carried out in this thesis fall within the above.

3 – MECHANICAL PROPERTIES OF SOFT TISSUES: THREE-DIMENSIONAL MODELS

If generalizing the problem of the stress vs. strain relationship to a three-dimensional elastic solid, the constitutive equation of the solid determined by Hooke's law can be expressed as follows (Royer and Deulesaint, 2000):

$$\sigma_{ij} = C_{ijkl}\,\epsilon_{kl} \qquad (2.9)$$

where Einstein's convention of repeated indices is applied. In this equation σ_{ij} is the stress tensor, ε_{kl} corresponds to the deformation tensor defined as $\varepsilon_{kl} = \frac{1}{2}\left(\frac{\partial u_k}{\partial x_l} + \frac{\partial u_l}{\partial x_k}\right)$, u_k is the component k = 1, 2, 3 of the displacement field, and C_{ijkl} is the stiffness or Cristoffel tensor that establishes the proportionality between stress and strain. The latter has 81 (3^4) elements representing elastic constants. However, since $\sigma_{ij} = \sigma_{ji}$ and $\varepsilon_{kl} = \varepsilon_{lk}$, this number is reduced to 36 independent coefficients. Furthermore, given the

symmetry of the derivative of the strain energy with respect to the stress tensor, this number is further reduced to 21 independent coefficients. Thus, the 21 independent elastic coefficients define the general anisotropic elastic solid. The symmetries of the elastic solid further reduce the independent elastic constants. To avoid working with a fourth-order tensor, it is usual to represent the independent constants of the stiffness tensor by two indices α and β, with values from 1 to 6 corresponding to a 6x6 matrix with the following convention:

$$(11) \leftrightarrow 1 \qquad (22) \leftrightarrow 2 \qquad (33) \leftrightarrow 3$$
$$(23) = (32) \leftrightarrow 4 \qquad (31) = (13) \leftrightarrow 5 \qquad (12) = (21) \leftrightarrow 6.$$

Thus, $C_{ijkl} = C_{\alpha\beta}$ with α related to (ij) and β related to (kl) (Benech et al., 2019; Carcione et al., 1988).

3.1 Isotropic solid

For an isotropic solid, the stiffness matrix takes the form (Royer and Deulesaint, 2000; Benech et al., 2019):

$$C_{\alpha\beta} = \begin{pmatrix} c_{11} & c_{12} & c_{12} & 0 & 0 & 0 \\ c_{12} & c_{11} & c_{12} & 0 & 0 & 0 \\ c_{12} & c_{12} & c_{11} & 0 & 0 & 0 \\ 0 & 0 & 0 & c_{44} & 0 & 0 \\ 0 & 0 & 0 & 0 & c_{44} & 0 \\ 0 & 0 & 0 & 0 & 0 & c_{44} \end{pmatrix} \qquad (2.10)$$

where $c_{11} = c_{12} + 2c_{44}$. Thus, an isotropic solid has only two independent elastic constants, c_{12} and c_{44}, which correspond to Lamé's constants λ and μ, respectively. They are related to the propagation velocity of the compression waves (V_L) and shear waves (V_T) (Benech et al., 2019). In particular, in the case of an isotropic solid, it is satisfied that $V_L \gg V_T$.

At this point, we should note that the model explained above is valid to explain the mechanical behavior of soft biological tissues, only when they can be assumed as isotropic solids (e.g., breast tissue, liver). As this thesis will focus on measuring the mechanical properties of skeletal muscle tissue, this model is not suitable due to the internal architecture of such tissue. Thus, it is necessary to extend the model for the case of a solid with transverse isotropy.

3.2 Transversely isotropic solid

As mentioned above, due to the parallel orientation of the muscle fibers, skeletal muscle can be modeled as a transversely isotropic material (Gennisson et al., 2003). Therefore, five independent elastic constants are needed to describe its elasticity. These types of material are characterized by an axis of symmetry such that the material properties are unchanged by rotation about this axis or reflections about any plane parallel to it. In the case of skeletal muscle, the symmetry axis is defined by the direction of the muscle fibers.

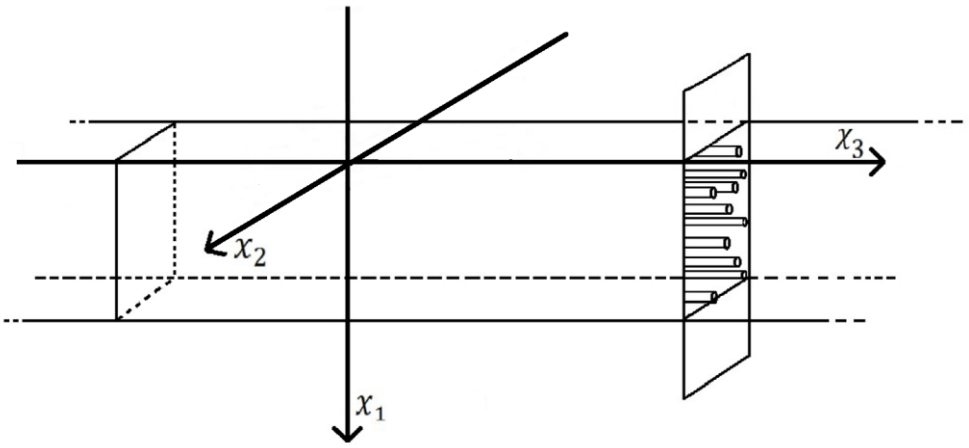

Figure 2.5. Orientation of the axes in a transversely isotropic solid. The axis of symmetry is defined by the orientation of the fibers. Adapted from Benech et al. (2019).

Let x_3 be the axis of symmetry, which is the axis of orientation of the muscle fibers, the axes x_1 and x_2 are perpendicular to it (Fig. 2.5). Using Voigt's notation for

this convention regarding the axes' orientation, the elastic tensor $C_{\alpha\beta}$ is given by (Royer y Deulesaint, 2000):

$$C_{\alpha\beta} = \begin{pmatrix} c_{11} & c_{11}-2c_{66} & c_{13} & 0 & 0 & 0 \\ c_{11}-2c_{66} & c_{11} & c_{13} & 0 & 0 & 0 \\ c_{13} & c_{13} & c_{33} & 0 & 0 & 0 \\ 0 & 0 & 0 & c_{44} & 0 & 0 \\ 0 & 0 & 0 & 0 & c_{44} & 0 \\ 0 & 0 & 0 & 0 & 0 & c_{66} \end{pmatrix} \qquad (2.11)$$

The relationship between σ and ϵ can also be expressed in terms of the compliance tensor $S = C^{-1}$ via $\epsilon_{ij} = S_{ijkl}\,\tau_{kl}$. The compliance tensor S can be expressed in terms of the elastic constants $c_{\alpha\beta}$ given in Eq. (2.11), but it is customary to express it in terms of the engineering constants, Young's modulus (E), Poisson's modulus (ν) and shear modulus (μ) as O'Donnel & Skovoroda (2004):

$$S = \begin{pmatrix} 1/E_T & -\nu_{TL}/E_T & -\nu_{LT}/E_L & 0 & 0 & 0 \\ -\nu_{TL}/E_T & 1/E_T & -\nu_{LT}/E_L & 0 & 0 & 0 \\ -\nu_{LT}/E_L & -\nu_{LT}/E_L & 1/E_L & 0 & 0 & 0 \\ 0 & 0 & 0 & 1/\mu_L & 0 & 0 \\ 0 & 0 & 0 & 0 & 1/\mu_L & 0 \\ 0 & 0 & 0 & 0 & 0 & 1/\mu_T \end{pmatrix} \qquad (2.12)$$

where L stands for longitudinal (along the muscle fibers) and T for transverse (perpendicular to the fibers). The five independent constants are reduced to three if the skeletal muscle is considered incompressible because, in this case, $\nu_{LT} = 1/2$ and $\nu_{TL} = 1 - E_T/2E_L$ (Rouze et al., 2021). Thus, we can choose any three independent from the tensor S, say E_L , μ_L and μ_T. As will be discussed below, the longitudinal and transversal shear moduli μ_L and μ_T can be assessed experimentally by elastography.

4 – MEASURING THE MECHANICAL PROPERTIES OF SKELETAL MUSCLE BY ELASTOGRAPHY

4.1 Considerations on skeletal muscle in elastography

As we have seen, skeletal muscle exhibits viscoelastic and nonlinear behavior. However, as mentioned previously, the general approach in elastography is to assume it to be a linear elastic solid with transverse isotropy. Therefore, before developing the characteristics of the main elastographic methods used in the literature, we will explain why such assumptions are made regarding the material nature of skeletal muscle.

First, considering the parallel architecture relative to the fiber arrangement of muscles such as the biceps brachii, the hypothesis of a material with transverse isotropy seems the most reasonable (Gennisson et al., 2003; Gennisson et al., 2005). Likewise, the hypothesis of linear material is classic in muscle elastography studies, which have been pioneers in estimating the shear elastic modulus of muscle using both ultrasound elastography (Bercoff et al., 2004a; Catheline et al, 2004; Deffieux et al., 2009; Gennisson et al., 2003; Gennisson et al., 2005, Nordez et al., 2008; Tanter et al., 2008) and magnetic resonance elastography (Dresner et al., 2001; Heers et al., 2003; Jenkyn et al., 2003; Uffmann et al., 2004).

As mentioned in the previous section, the elasticity of a soft tissue such as skeletal muscle is determined by the shear elastic modulus μ. Later, we will see that in elastography, such modulus is characterized by measuring the *shear wave* velocity in the tissue. In this way, since in this type of media the amplitude of shear waves is very small, non-linear effects can be neglected (Nordez et al., 2010). Likewise, the equations that allow estimating the shear elastic modulus consider the muscle as a purely elastic material. Thus, the influence of viscosity on the shear wave velocity estimates is neglected. This is based on previous studies, which have analyzed the influence of viscosity on the measurement of the velocity of this wave (Deffieux et al., 2009;

Catheline et al., 2004). In this regard, by using shear wave elastography, Deffieux et al. (2009) showed that when shear waves propagate longitudinally to the muscle fibers, they are practically non-dispersive. This means that under such conditions, the velocity of these waves is almost independent of the excitation frequency. These results agreed with those obtained by Catheline et al. (2004), using one-dimensional transient elastography on agar-gelatin phantoms and beef samples. Therefore, based on the above, the estimation of the shear elastic modulus in skeletal muscle is little affected by viscous effects, which can be neglected accordingly.

However, it should be mentioned that this topic continues to be developed at present. In this sense, recent efforts are tending to consider the viscoelastic character of soft solids, when estimating the elasticity from measurements of the shear wave velocity in the medium (Qiang et al., 2015; Kijanka et al., 2018; Greenleaf and Alizad, 2017; Carrascal et al., 2018).

4.2 Ultrasound elastography

In order to evaluate the shear elastic modulus of soft tissues, all existing ultrasound elastographic methods are based on the same principle: an external force is applied to the tissue and the resulting displacements are followed. According to how the external force is applied to excite the medium, ultrasound elastographic methods can be classified into two main types: *static* (or *quasi-static*) methods and *dynamic methods*.

Static elastography (Ophir, 1991) is the first ultrasound technique that made it possible to image the elasticity of biological tissues. The basis of the method consists of applying a constant tension to the tissue and measuring the component of the internal deformations thus produced in the direction of the ultrasound beam (Benech, 2004). Such deformation and the generated strain are estimated by a two-dimensional correlation of the ultrasound images (Gennisson et al., 2013). For its part, the elastic

modulus is given by Hooke's law which, as we have seen, links the stress acting on the body with its deformation in a purely elastic medium. In practice, as the applied stress is unknown, only the deformation is shown. The deformation map thus obtained is called an *elastogram*. This method has the advantage of being easy to implement but, as the stress distribution is unknown, it does not allow quantifying the elastic modulus of the medium in kilo-Pascals (kPa). However, it has been implemented in many commercial ultrasound imaging devices, as simple but indirect information on tissue stiffness.

On the other hand, in dynamic methods, a time-varying force is applied to the tissue. This can be either a short transient mechanical force or an oscillatory force with a certain frequency. In this sense, in a solid body, a time-varying mechanical perturbation will propagate as compression (or longitudinal) waves or as shear waves (Fig. 2.6). The former propagate very rapidly in the human body ($\sim$ 1500 m/s), and at ultrasonic frequencies ($\sim 10^6$ Hz) can be used to image the body. Meanwhile, typically at low frequencies (100 - 1000 Hz), shear waves predominate in soft solids. These are generated over the entire frequency range, but at high frequencies, the amplitude is so small that they are only detected very close to the source. They propagate more slowly than compression waves, and their velocity ($\sim$ 1 - 50 m/s) is directly related to the shear elastic modulus of the medium (μ). Particularly, as we have seen in Section 2.1, the Young's modulus of soft biological tissues can be approximated as three times such modulus (Eq. (2.5)).

Thus, dynamic elastography methods based on ultrasound are within the concept of Multiwave Imaging (Fink, 2010). According to this, such methods are based on combining the use of ultrasound waves with low-frequency waves, to take advantage of the "best" of each in optimizing contrast and resolution in imaging. Thus, the former represents a high spatial resolution, on the order of a millimeter or smaller, which

allows for recording the displacement of low-frequency waves. However, they show poor contrast, especially concerning the elastic properties of soft tissues. On the other hand, the low-frequency waves exhibit a high contrast in terms of elasticity changes of the medium, but poor spatial resolution. The combination of these two types of waves makes it possible to obtain a final result that exhibits high spatial resolution and high contrast (Benech, 2004).

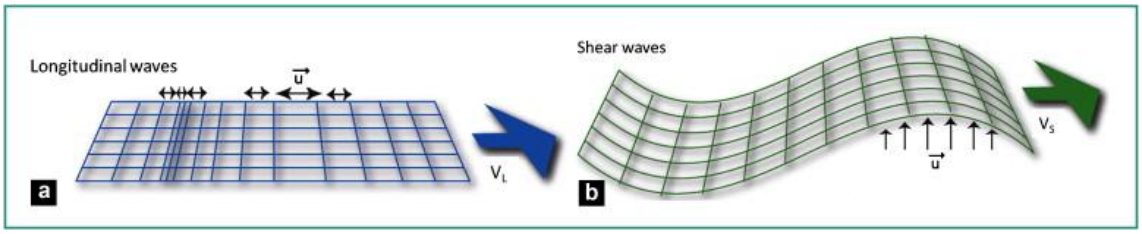

Figure 2.6. a: The compression wave propagates by successive volume changes of the medium. The wave propagates with velocity V_L principally parallel to the longitudinal displacements of the medium ($\vec{u}$). b: The shear wave propagates with velocity V_S mainly perpendicular to the successive displacements of the medium in the transversal direction. Taken from Gennisson et al. (2013).

In this way, dynamic elastography methods based on shear wave elastography (SWE) can produce a quantitative map of the shear elastic modulus with higher resolution than static methods. However, the use of dynamic methods requires a much more complex wave emission-reception system. Such a system must be able to generate the shear waves (using a mechanical vibrator or an ultrasonic radiation pressure generation system), as well as to obtain the images of the small displacements induced by them (through an ultrafast ultrasound or stroboscopic system) (Gennisson et al., 2013). The reader can find in Ryu & Jeong (2017) and Creze et al. (2018), a detailed and updated review of the concepts, basic principles, and applications of these methods to muscle biomechanics.

Among the dynamic elastography methods with the characteristics described previously, Supersonic Shear Imaging (SSI) (Bercoff et al., 2004b) has become the reference method in the muscle biomechanics field. In this thesis, SSI will be used for

the studies corresponding to Chapters 3 and 4, so the specific features of this method will be detailed below.

4.3. Supersonic Shear Imaging method

Two concepts intimately linked to the SSI method are *acoustic radiation force* and *ultrafast ultrasound imaging* Bercoff (2004a). In the following paragraphs, we will provide an overview of these concepts, which are at the basis of the SSI method.

As shown in Figure 2.7A, the ultrasound transducer of the SSI generates a local material displacement ("push") at a focal point through the acoustic radiation force effect. In this regard, the idea of the SSI is that the ultrasound beams are successively focused at different depths in the medium, thus generating local displacements ("pushing") at several internal positions (Fig. 2.7B). Thus, each focal beam generates shear waves that propagate spherically away from the source. As the electronics of the method allow moving the source (“push”) at a higher speed than the generated shear waves, the different spherical shear waves interfere constructively as a cone (Fig. 2.7B) (Bercoff et al., 2004c). This creates a plane wavefront (cylindrical in three dimensions) that can be visualized with the ultrafast ultrasonic imaging device (Fig. 2.7C). Thus, the acquired images allow to scanning the entire image plane with a very good temporal resolution in a single acquisition. This is generally done at a speed of 5000 images per second. Therefore, it is not necessary to repeat the acquisition several times by stroboscopy to acquire the entire displacement field. This allows performing a real-time image acquisition and a fast average of them to improve the image quality (Gennisson et al., 2013).

Therefore, the SSI method uses acoustic radiation pressure as a wave generator. The whole method, concerning both the shear wave excitation as well as the shear wave propagation imaging, is integrated into the ultrasound probe which contains the ultrasound

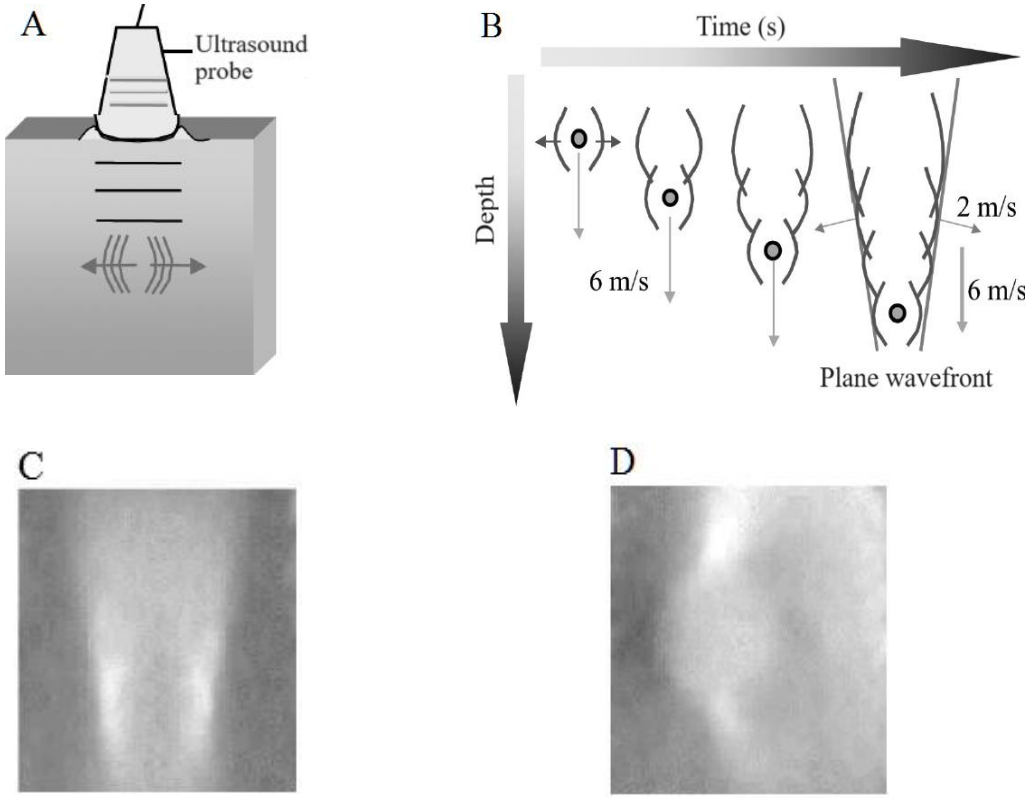

Figure 2.7. A: Push generated by the ultrasound transducer through the ultrasound radiation force effect. B: Local tissue displacements generated successively at various depths, generating shear waves propagating spherically outward from the source. C: Constructive interferences of the shear waves generate a plane wavefront. D: Deformation of a planar shear wave due to an inclusion in the medium. Adapted from Bercoff et al., (2004a).

imaging transducer array (Fig. 2.7A). The generated shear wave has an amplitude of tens of microns, which can be detected with a good signal-to-noise ratio using the acoustic speckle tracking algorithm and ultrafast imaging. Thanks to the above, the acquisition of the shear wave propagation can be displayed in real-time as a conventional ultrasound image (Fig. 2.7D). Therefore, the SSI can construct an elasticity map of the medium by estimating the shear wave velocity (V_s) between two image points through a time-of-flight algorithm, and then calculating the shear elastic modulus (μ) by:

$$\mu = \rho V_s^2 \qquad (2.13)$$

where ρ is the medium density which is assumed constant.

4.4 – Biomechanical applications of muscle elastography

4.4.1 State of the art

Elastography-based research on muscle biomechanics has been dominated mainly by the application of shear wave elastography methods. This has provided a novel way to measure the change in the mechanical properties of such tissue, thus driving a new approach in the studies on muscle biomechanics.

Before SSI became the reference methodology in muscle elastography, transient elastography (TE; Catheline et al., 1999) was applied for different purposes in muscle biomechanics studies. It is a dynamic elastography method from which the SSI is derived, so the two methods are closely related. Thus, for example, Gennisson et al. (2003) reported results of applying TE to quantify muscle elasticity as a function of the force developed by the muscle. They also studied the polarization of the propagation velocity of shear waves as a function of the orientation of the muscle fibers. Further, Gennisson et al. (2005) published results of this method used to estimate the viscosity of the biceps brachii muscle as a function of its anisotropy. This was carried out in conjunction with simultaneous recordings of its electrical activity, measured through surface electromyography (EMGs). In addition to these works, Nordez et al. (2008) also used TE to measure the local elasticity of the medial gastrocnemius muscle during passive ankle dorsiflexion. In this way, they found a linear relationship between this variable and the maximum passive torque developed, as well as good reproducibility of the results. Accordingly, their results suggested that passive torque changes after static muscle stretching are due to a significant increase in muscle length, while intrinsic musculo-articular mechanical properties remain unchanged.

Concerning the SSI, this method has become a widespread research tool in muscle biomechanics over the past two decades. Thus, we can mention different works

in which this method has been used to investigate several biomechanical aspects of skeletal muscle closely related to its elastic properties. For example, some authors have applied the SSI to assess differences in passive muscle shear elasticity after a force training program of trained vs. non-trained subjects, the passive behavior of individual muscles in different stretching positions, and regional differences in muscle elasticity after eccentric exercise (Lacourpaille et al., 2014; Le Sant et al., 2015; Mannarino et al., 2019; Avrillon et al., 2020). Liekewise, the application of SSI in skeletal muscle is also being considered for its clinical use in sports medicine (Creze et al., 2018). As for the applications of the SSI method that are more related to the present work, several studies have characterized the relation of muscle shear elasticity with joint angle, contraction intensity, and electromyography (EMG) activity level (Ateş et al., 2015; Bouillard et al., 2011; Gennisson et al., 2010; Nordez et al., 2010; Lapole et al., 2015; Yoshitake et al., 2014; Zimmer et al., 2023). Figure 2.8 shows an example of the above, where the SSI was used to measure the elasticity of the biceps brachii and brachialis muscles as a response to different load levels. On the other hand, other works have used the SSI to measure the changes in the muscle shear elastic modulus, both in normal and fatiguing conditions, in order to characterize the load sharing and the dynamics of muscle contraction of the synergistic muscles (Bouillard et al., 2011, 2012a, b). Furthermore, these were the first studies that tended to use elastography to estimate individual muscle forces from elasticity measurements (Hug et al., 2015a).

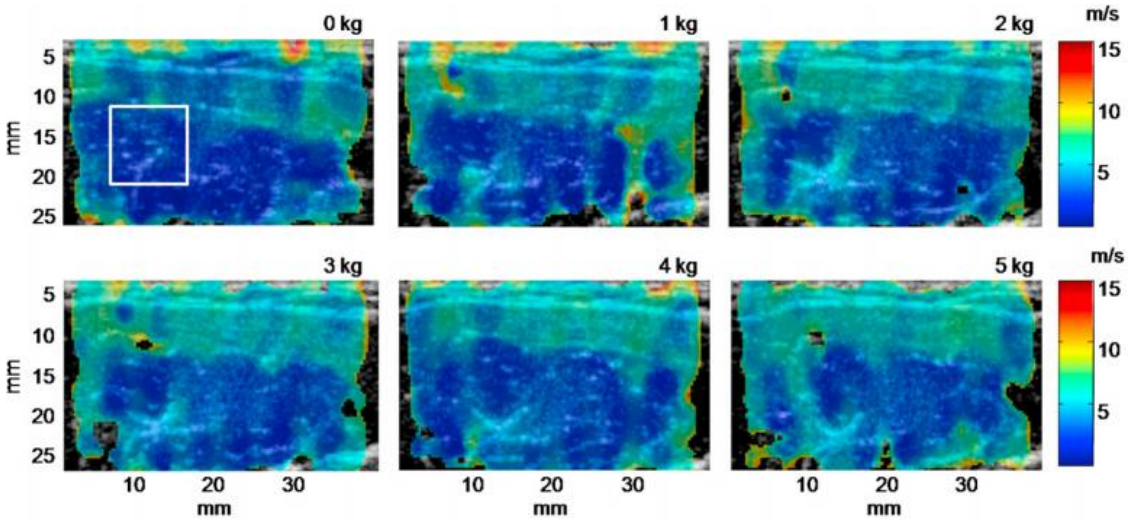

Figure 2.8. Maps of the shear modulus of elasticity in the brachialis and biceps brachii as a function of different loading conditions. Both muscles are easily distinguishable in each image as a function of the shear wave velocity measured by the SSI (top: biceps brachii; bottom: brachialis). Taken from Gennisson et al. (2010).

4.4.2 Current challenges and main thematic axes of the thesis

Previous studies on muscle elastography have shown the association between the mechanical properties and the physiology of skeletal muscle. In this regard, the shear elastic modulus provides valuable information about the different processes and biological phenomena associated with the intrinsic mechanical state of the tissue (Sarvazyan, 1993). However, due to the incipient application of elastographic methods in biomechanics, as well as their limitations, there are still many unknown aspects of muscle biomechanics that can be addressed by elastography.

The process of muscle contraction is well described at both the microscopic and macroscopic levels from the classic papers of the 1960s (Gordon et al., 1966; Huxley, 1957; Huxley et al., 1961). Besides, since the 1980s, it has been well-known that active cross-bridges during contraction and force generation are formed following specific ligand-binding dynamics, which have long been known in molecular receptors. Several works have shown the above in both isolated myofilaments and muscle fibers (Shchepkin et al., 2017; Lehman, 2017; Reshetnyak et al., 2012; Rao et al., 2009; Zot et

al., 2009; Tobacman & Butters, 2000; Lehrer & Geeves, 1998; Greene & Eisenberg, 1988; Lehrer & Morris, 1982; Greene & Eisenberg, 1980; Porter & Weber, 1979). Nevertheless, the correspondence between the change in muscle elasticity and the underlying contractile mechanisms is not well understood. This has not been studied either on isolated muscles or in more realistic conditions where they act coordinately with other synergistic muscles. The above may have deep biomechanical connotations regarding the muscle contraction dynamics during load sharing and force generation. Thus, this will be addressed in Chapter 3 by using the SSI method.

On the other hand, the estimation of individual muscle forces constitutes a long-standing challenge in muscle biomechanics. Beyond some efforts typically performed with electromyography, there is currently no accurate method able to estimate such forces during *in vivo* muscle action. In this sense, given the mechanical and non-electrical nature of the estimations performed with elastography as opposed to electromyography, the former is shown to be a more appropriate method for force estimation (Hug et al., 2015a, b). In this respect, in the last years, some works have made advances in this direction, showing the viability of elastography to be used for this purpose (Bouillard et al., 2011, 2012a; Hug et al., 2015a; Zonnino et al., 2019; Smith et al., 2023). Thus, based on the results of Chapter 3 concerning the dynamical behavior of synergistic muscles during load sharing, in Chapter 4 we develop a biomechanical model able to estimate the individual forces generated by them.

In addition to the above, it is unviable to carry out many other relevant research problems in biomechanics due to the current limitations of the elastographic methods. For example, in addition to their high cost, SWE methods need some infrastructure (e.g., a clinic or laboratory) to be used properly, making field applications unfeasible. So, elastography into biomechanical research is limited to specific applications

performed in clinics or laboratories. Likewise, SWE methods lack the ability to perform shear elasticity measurements on more than one muscle simultaneously. In addition, they have a limited sampling frequency (~ 1-2 Hz). This restricts the experimental protocols that can be performed with elastography. In particular, this determines that only one muscle can be measured at a time and that the tasks must be slow, controlled, and sufficiently long-lasting to obtain the necessary data for an adequate analysis. This limits the utility of elastography for biomechanical research and its applications to other related fields such as sports and medical sciences. As an example, current elastographic methods are unable to simultaneously assess the time-dependent change in the elasticity of a group of muscles as a result of different torque production rates. In this regard, in Chapter 5, we will address this problem, by enhancing a low-frequency surface wave elastography method previously developed by our group in the Laboratory of Acoustical Ultrasound (LAU) of the Faculty of Sciences (Univesity of the Republic (UdelaR), Uruguay) (Benech et al., 2019; Grinspan et al., 2021). We will show that this method overcomes the current limitations of SWE and extends the scope of elastography applications in muscle biomechanics.

Finally, Chapter 6 describes the general conclusions and future perspectives of the thesis. Thus, we discuss further research issues that arise from the work, and how they can be addressed by the concepts and methods developed throughout the text.

5 – CHAPTER CONCLUSIONS

Elastography is a novel methodology for investigating the mechanical properties of soft biological tissues. As we have seen, this approach makes it possible to estimate informative parameters on the intrinsic mechanical state of the tissue, such as its shear elastic modulus. In particular, the application of elastography to skeletal muscle has defined a new research field in muscle biomechanics. For such a purpose, the muscle is

usually modeled as a linear elastic, transversely isotropic solid, whose viscosity is often neglected.

The SWE is the main elastographic modality used in muscle biomechanics. Particularly, the SSI is considered the gold standard method, thus being the main technique currently used to assess the mechanical properties of skeletal muscles. They combine the propagation of high and low-frequency waves, allowing the estimation of the local elasticity of the medium with high spatial resolution. Nevertheless, they present some practical limitations which limit its application in biomechanics and related fields. As a result, low-frequency elastography methods have recently been described in the literature as an alternative to SWE.

Thus, elastography appears to be a valuable methodology to deepen the understanding of many unknown aspects of muscle biomechanics. In this sense, elastography has the potential to be used to infer different aspects concerning the dynamics of muscle contraction, load sharing, and force generation that have not been addressed previously. Besides, the temporal dependence of muscle action during the synergism could be studied by overcoming the current limitations of the elastographic methods regarding measuring several muscles simultaneously and at a higher sampling rate. The challenges mentioned above have the potential to widen the applications of elastography in biomechanics and related fields, thus motivating the works presented in the following Chapters of this thesis.

CHAPTER 3

CHARACTERIZING THE LOAD SHARING BETWEEN SYNERGISTIC MUSCLES BY A LIGAND-BINDING APPROACH AND ELASTOGRAPHY

1 – INTRODUCTION

As was explained in Chapter 1, skeletal muscle contraction is determined by cross-bridge formation between the myosin heads and the actin active sites. When the muscle contracts, it shortens, increasing its longitudinal shear elastic modulus (μ_L). In this regard, the skeletal muscle can be considered structurally analogous to a receptor-ligand system. As will be seen below, in such systems, the ligands are the molecules that allow the receptors to perform their biological function when attached to the binding sites, thus increasing the fraction between occupied and total sites according to specific ligand-binding dynamics. Since shortening and the related changes in muscle properties during its isometric contraction depend on cross-bridge formation, this system is suitable to be analyzed through this framework. However, the biomechanical studies driven by elastography have not yet addressed the link between muscle elasticity, force generation, and the binding dynamics among the myosin heads and the active sites of the actin filaments. We believe that elastography can be a valuable tool to characterize the contractile processes that underlie the specific muscle functions at the macroscopic scale.

In this context, this work aims to apply shear wave elastography (SSI method) and the ligand-binding framework to approach the possible intrinsic mechanisms behind muscle synergism. Based on the short-range stiffness principle and the acousto-elasticity theory, we define the coefficient C, which is directly related to the saturation fraction of molecular receptors and links the relative longitudinal deformation of the muscle to its μ_L. We show that such a coefficient can be obtained directly from μ_L

estimates, being able to characterize the dynamic changes in the longitudinal deformation (ξ_L) of muscle during the isometric contraction of the elbow flexors. Thus, it provides a new elastography-driven approach to understanding the possible underlying basis behind load sharing between synergistic muscles.

2 – MODELING THE RELATIONSHIP BETWEEN ξ_L AND μ_L FROM SHORT-RANGE STIFFNESS AND THE ACOUSTO-ELASTICTY THEORY

2.1 The short-range stiffness property

The initial response of an isometrically contracting muscle (Section 4.1 of Chapter 1) is characterized by a linear relationship between the change in muscle force and its length. This property, termed *short-range stiffness* (SRS), describes the initial response of a muscle to external perturbations in length before changes in activation mediated by reflex or voluntary mechanisms occur (Cui et al., 2008; Hu et al., 2011; Morgan, 1977; Rack y Westbury, 1974). SRS depends on both the force-dependent properties of the muscle fibers as well as the material properties of the passive tendon structures. The reader can find more information on the latter in Cui et al. (2008) and Morgan (1977). Since previous work has shown that SRS is mainly force-dependent (Morgan, 1977), in the following paragraphs we will focus on discussing the force-dependent contribution of the contractile structures responsible for generating the active force of the muscle.

As shown in Figure 3.1, this contribution can be calculated from a curve of force and length data as a function of time. Since the axial stress (σ_L) developed by the muscle is related to the force exerted by the muscle (F_m) through its cross-sectional area (A_T), a widely accepted model of SRS assumes that Young's modulus in the fibers' direction (E_L) is directly proportional to σ_L (Zonino et al., 2019):

$$E_L = \omega.\sigma_L = \omega.\frac{F_m}{A_T} \qquad (3.1)$$

where ω is a muscle-specific proportionality constant.

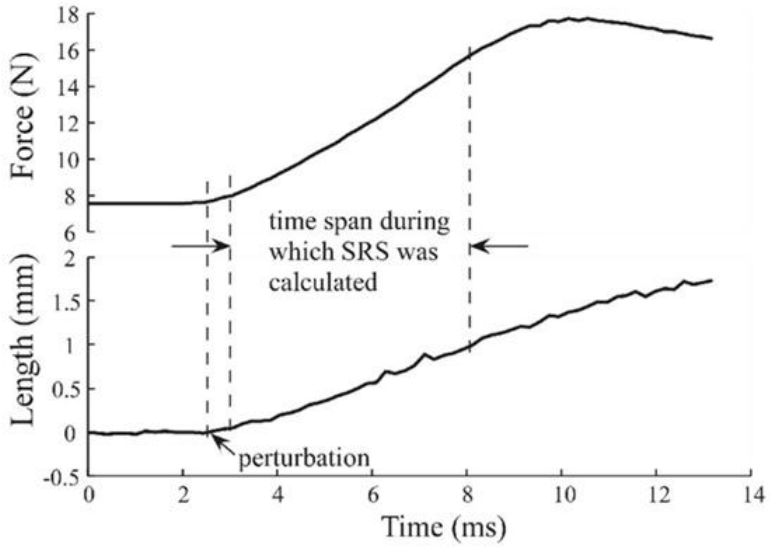

Figure 3.1. SRS calculation. The figure shows muscle force and length as a function of time during a perturbation (contraction induced by electrical stimulation). A linear regression is performed between the data within the linear portion of these curves. The SRS is calculated as the slope of this regression. Taken from Cui et al. (2008).

In turn, there is an empirical relationship between μ_L and E_L according to which (Eby et al., 2013):

$$E_L = \gamma \mu_L \qquad (3.2)$$

where γ is another proportionality constant of the muscle. Likewise, if we consider that the muscle presents basal values of μ_L and E_L when it is at rest, i.e. when it does not exert torque ($\tau = 0$), we can rewrite Eq. (3.2) as a function of τ:

$$E_L = \gamma\big(\mu_L(\tau) - \mu_L(0)\big) = \gamma \Delta\mu_L(\tau) \qquad (3.3)$$

Thus, by Eqs. (3.1) and (3.3), the SRS principle determines the following proportionality relationship between σ_L and μ_L, for a certain level of τ:

$$\sigma_L = -\frac{1}{\beta_\parallel}\Delta\mu_L(\tau) = -\frac{1}{\beta_\parallel}\big(\mu_L(\tau) - \mu_L(0)\big) \qquad (3.4)$$

where $\beta_\parallel$ is also a muscle proportionality constant.

The structural basis of the SRS depends on the overlap between actin and myosin filaments, that is, on the axial deformation of the muscle. This derives directly from the cross-bridge muscle model (Gordon et al., 1966; Huxley, 1957; Huxley et al., 1961), according to which it is possible to make some predictions about the variation of the SRS as a function of muscle conditions. According to this, the stiffness of the cross-bridge matrix (i.e., the stiffness of the contractile machinery of the muscle) is proportional to the number of attached cross-bridges. An increase in their number determines an increase in both E_L and μ_L (Blangé et al., 1972; Zonino et al., 2019). In this sense, the stiffness of the cross-bridge matrix is also proportional to F_m, since both are proportional to the number of active cross-bridges (Morgan, 1977). This relationship was previously derived by Blange et al. (1972) based on a model developed from measurements in rat muscle. Mathematically, this relationship can be written as (Morgan, 1977):

$$\Delta x_m = \alpha_0 . \frac{\Delta F_m}{F_m} \qquad (3.5)$$

where F_m is the isometric force, ΔF_m is a small change in isometric force, Δx_m is the associated change in the length of the cross-bridge matrix, and α_0 is a proportionality constant that depends on the properties of the cross-bridges and the number of sarcomeres in series. Therefore, all the above implies that the SRS is an intrinsic property of skeletal muscle, closely related to the amount of attached cross-bridges and muscle elasticity.

2.2 Acousto-elasticity of skeletal muscle

The acousto-elasticity theory relates the shear wave velocity to the axial strain (σ_L) on the muscle (Gennisson et al., 2007; Destrade et al., 2010). In this sense, it has recently been shown that this theory can be adapted to study the propagation of shear

waves in a homogeneous, incompressible, transversely isotropic solid and subject to axial strain, such as skeletal muscle during isometric contraction (Remeniéras et al., 2021).

According to what we have seen in Section 3.2 of Chapter 2, during a voluntary muscle contraction, the shortening of the fibers induces axial tension inside the tissue ($\sigma_{33} = \sigma_L$). This modifies its mechanical properties and causes the shear wave velocity (V_T) to become a function of σ_L. The relationship between V_T and σ_L can be found at the basis of the acousto-elasticity theory for transversely isotropic materials through the third-order expansion of the elastic strain energy in terms of the strain tensor (Remeniéras et al., 2021). The result of the above shows that it is possible to write the acoustic-elastic equation for the shear wave velocity as:

$$\rho V_L^{||2} = \mu_L(0) - \beta_{\parallel}\sigma_L(\tau) \qquad (3.6)$$

for the shear wave propagating parallel with respect to the muscle fibers, and

$$\rho V_T^{\perp 2} = \mu_T(0) + \beta_{\perp}\sigma_L(\tau) \qquad (3.7)$$

for such a wave propagating perpendicular to them. In these equations, ρ is the muscle density (1000 kg/m^3), $\mu_{L(T)}(0)$ is the value of the elastic shear modulus at rest (null external torque), while $\beta_{\parallel}$ and $\beta_{\perp}$ are coupling constants that depend on the second and third order parameters of the strain energy. Note that the acousto-elasticity theory and SRS converge in the same result regarding the axial stress, since σ_L can be obtained by solving it from Eq. (3.6), thus yielding the same expression as Eq. (3.4) (Grinspan et al., 2023).

Previous work has shown empirically that while $V_T^{||}$ changes significantly during an isometric contraction, $V_T^{\perp}$ has little or no variation (Remeniéras et al., 2021).

Experiments show that $\beta_{\parallel}$ is negative, indicating an increase of μ_L with strain. On the other hand, $\beta_{\perp}$ is also negative and one or two orders of magnitude smaller than $\beta_{\parallel}$, indicating a small softening in the transverse direction with strain. Related to the above, the contribution of μ_T can be neglected as a relevant variable for the muscle contractions studied in this thesis.

As far as E_L is concerned, it is expected to have a strong correlation with $V_T^{||}$. As the muscle contracts, it becomes more difficult to achieve a longitudinal deformation for a given stress value. Therefore, an increase in E_L during contraction is expected, as happens with $V_T^{||}$, since the muscle becomes stiffer. Although it is not possible to obtain this relationship theoretically, experimental works have shown a linear relationship between them (Eby et al., 2013). In this sense, assuming this behavior, it is possible to obtain an analogous expression to that of Eq. (3.3):

$$E_L(\tau) = \gamma \rho V_T^{||}(\tau)^2 = \gamma \mu_L(\tau) \qquad (3.8)$$

Thus, both the SRS and the theory of acousto-elasticity imply that of the three independent constants needed to describe the elastic behavior of the muscle (Section 3.2 of Chapter 2), only μ_L is relevant during an isometric contraction.

2.3 Unifying acousto-elasticity and SRS into a single coefficient

Muscle contraction is carried out by shortening the muscle fibers, which produces a longitudinal instantaneous strain $\epsilon_{33} = \xi_L$. If the normal stresses perpendicular to the fibers (σ_{11} and σ_{22}) are zero or negligible compared to σ_L, we can write:

$$\xi_L(\tau) = \frac{\sigma_L(\tau)}{E_L(\tau)} \qquad (3.9)$$

Using Eqs. (3.6) and (3.8), the relative longitudinal strain of muscle can be written as a function of μ_L as:

$$\xi_L = -\frac{1}{\beta_{\|}}\frac{\mu_L(\tau) - \mu_L(0)}{\gamma\mu_L(\tau)} = AC(\tau) \qquad (3.10)$$

where:

$$A = -\frac{1}{\beta_{\|}\gamma}\,, \qquad (3.11)$$

$$C(\tau) = \left(1 - \frac{\mu_L(0)}{\mu_L(\tau)}\right) \qquad (3.12)$$

Specifically, ξ_L measures the shortening of the muscle in a small portion determined by the spatial resolution of the system, of the order of one ultrasound wavelength (~ 300 μm, according to our experimental setup). As the sarcomeres are aligned in series along the fiber direction, ξ_L is representative of the longitudinal shortening of the whole muscle as a product of the overlap between the actin and myosin filaments and the increase of μ_L. In this regard, the coefficient $C(\tau) \in [0, 1]$ is directly proportional to the ξ_L and can be calculated from experimental data of μ_L measured by SSI.

3 – SKELETAL MUSCLE AS A MOLECULAR RECEPTOR

As pointed out in classic papers from the 1960s, the structural basis of the longitudinal deformation that characterizes muscle contraction depends on the overlap between actin and myosin filaments through the formation of cross-bridges (Gordon et al., 1966; Huxley, 1957; Huxley et al., 1961). In this regard, it is important to highlight the structural and functional analogy between cross-bridge formation and the ligand-binding behaviors exhibited by the molecular receptors. The main feature of these molecules is that they have one or more specific sites to bind their ligands, becoming a

receptor-ligand complex when saturated. Several works have shown that in the skeletal muscle, the formation of actin-myosin cross-bridges follows the same binding dynamics as the molecular receptors, depending on certain physiological factors closely related to muscle contraction (Shchepkin et al., 2017; Lehman, 2017; Reshetnyak et al., 2012; Rao et al., 2009; Zot et al., 2009; Tobacman & Butters, 2000; Lehrer & Geeves, 1998; Greene & Eisenberg, 1988; Lehrer & Morris, 1982; Greene & Eisenberg, 1980; Porter & Weber, 1979). In this regard, when skeletal muscle contracts, it develops force through the formation of cross-bridges, by increasing the fraction of the myosin heads attached to the actin active sites.

3.1 Basic concepts of the ligand-binding behavior of molecular receptors

Specific recognition and interaction between molecular receptors (R) and ligands (L) determine behavior, response, and regulation of essential functions in all living organisms (Cattoni et al., 2015). The binding of a ligand to its specific domain in the receptor is a process based on equilibrium, i.e., it is a reversible process from one state to the other so that the ligand binds to the receptor and dissociates from it equally. The kinetics of these interactions can be studied by the law of mass action. In this regard, the following reaction represents the simplest ligand-binding scheme for an unsaturated molecular receptor:

$$R + L \rightleftharpoons RL \implies K_a = \frac{[RL]}{[R][L]} = \frac{1}{K_d} \qquad (3.13)$$

where RL is the receptor-ligand complex and the square brackets denotes concentrations. The effectiveness of the receptor binding sites to bind their ligands is determined by the association and dissociation constants, K_a and K_d, respectively. The

high-affinity bindings have high K_a and low K_d, while the opposite happens for the low-affinity bindings.

One essential variable for identifying the properties of receptor-ligand interactions is the *saturation fraction* (Y). This is defined as the ratio between their occupied (saturated) and the total binding sites, which can be expressed in terms of the concentration of the reactants and products of Eq. (3.13) (Wyman & Gill. 1990):

$$Y = \frac{occupied\ sites}{total\ sites} = \frac{[RL]}{[R] + [RL]} \qquad (3.14)$$

This fraction is commonly measured by indirect methods. For example, the saturation fraction of the RL complex could be characterized by UV light absorbance measurements. Here, it is possible to obtain the saturation fraction of RL by measuring its light absorbance and comparing it with respect to a reference value (for example, the light absorbance of R).

Depending on how K_a behaves as the ligand concentration increases, receptors can be classified as hyperbolic or cooperative. In hyperbolic (H) receptors, the binding sites are independent and K_a remains constant as $[L]$ becomes higher. On the other hand, in cooperative receptors, K_a is modified as a function of $[L]$; if K_a increases, the receptor is cooperative positive (C+); if K_a decreases, the receptor is cooperative negative (C-). Therefore, receptor-ligand complexes are formed following cooperative or hyperbolic dynamics, depending on the characteristics of the association between the involved molecules (Wyman & Gill. 1990). In this sense, Figure 3.2 shows the different saturation curves $Y([L])$ exhibited for each receptor as a function of their specific ligand-binding behavior.

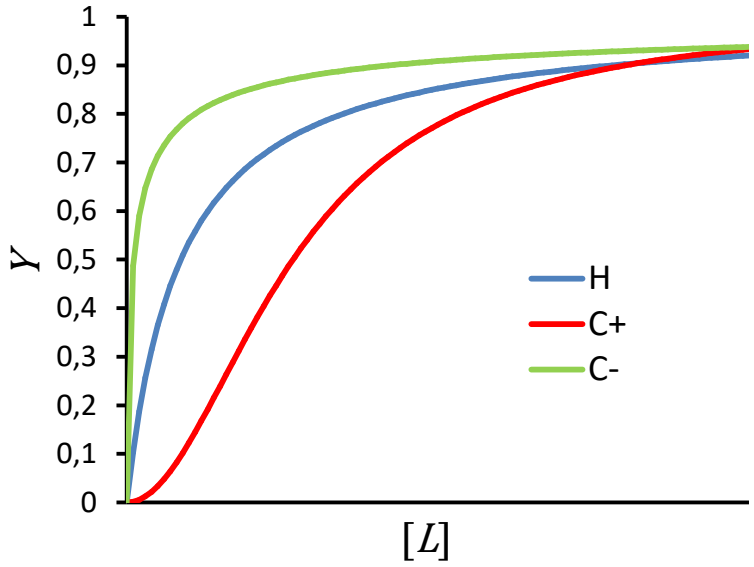

Figure 3.2. Typical saturation curves of the different ligand-binding behaviors exhibited by molecular receptors. A rectangular hyperbola characterizes the saturation curve of the hyperbolic (H) dynamic. A similar trend is present in the negative cooperative dynamics (C-), although mathematically, it does not conform to a rectangular hyperbola. On the other hand, a sigmoidal saturation curve characterizes the cooperative positive (C+) dynamic.

3.2 Relationship between the saturation fraction and $C(\tau)$

As noted previously, skeletal muscle can be considered analogous to a receptor-ligand system, as its contraction depends on the formation of cross-bridges by increasing the fraction of the myosin heads attached to the actin active sites. As shown in previous studies, the stiffness of the cross-bridge array at the sarcomere level is linearly related to the number of attached cross-bridges (Blangé et al., 1972; Morgan et al., 1977). Thus, according to the short-range stiffness principle (SRS), the axial shortening of the muscle during its isometric contraction increases its longitudinal shear elastic modulus (μ_L), being proportional to the attached cross-bridges (Zonnino et al., 2019). In addition, Van Eesbeek et al. (2010) have proposed that the SRS may indicate the amount of attached cross-bridges and the muscle contribution to joint stiffness.

Since μ_L is proportional to the amount of active cross-bridges, similar to the light absorbance measurements, the elastography could characterize the fraction of the attached actin-myosin cross-bridges as a function of the joint torque level. Thus, the

$\mu_L(0)$ value implies that the sarcomere has no or a basal proportion of attached cross-bridges, that is, $\mu_L(0) \sim [R]$. On the other hand, when the muscle contracts, a certain amount of cross-bridges are formed according to the torque level, and its μ_L varies with respect to the basal (resting) state such that $\Delta\mu_L(\tau) = \mu_L(\tau) - \mu_L(0) \sim [RL]$. In this way, it is possible to express Y in terms of μ_L:

$$Y = \frac{[RL]}{[R] + [RL]} \approx \frac{\mu_L(\tau) - \mu_L(0)}{\mu_L(0) + (\mu_L(\tau) - \mu_L(0))} = \frac{\Delta\mu_L(\tau)}{\mu_L(\tau)} = C(\tau) \qquad (3.15)$$

Therefore, the above shows that the saturation fraction of a molecular receptor corresponds to the $C(\tau)$ coefficient in the skeletal muscle, which can be characterized by elastography.

4 – STUDY OF CONTRACTILE DYNAMICS OF SYNERGISTIC ELBOW FLEXOR MUSCLES

4.1 Materials and methods

4.1.1 Subjects

Thirteen healthy male volunteers participated in the study (age 27.92 ± 6.90 yr, height 179.85 ± 3.31 cm, weight 84.69 ± 12.70 kg). They were informed about the methods, procedures, and the purpose of the study. All participants provided their written informed consent. The experimental design of the study was conducted according to the last version of the Helsinki statement and was approved by the Ethical Committee of the Faculty of Medicine (UdelaR, Uruguay, File No. 071140-001398-11).

4.1.2 Instrumentation

Ergometry

A research isokinetic dynamometer (Biodex System 4; Biodex Medical, Shirley, NY) was used to measure the angle and torque production of the elbow joint. During the

data collection, the volunteers were positioned with their right shoulder and elbow flexed at 90º and the forearm supinated. The elbow joint was aligned coaxially with the axis of the dynamometer (Figs. 3.3A and 3.3B).

Elastography

An Aixplorer ultrasonic scanner (Supersonic Imagine, Aix en Provence, France) with a linear transducer array (2-10 MHz, SuperLinear 10-2, Vermon, Tours, France) was used in SSI mode to obtain the shear elasticity map of the tissue. The measurements of this study were made in the biceps brachii (BB), brachioradialis (BR), and brachialis (BA) muscles, placing the echographic probe aligned regarding their shortening direction (x_3). As seen in Section 3.2 of Chapter 2, by considering the architecture of such muscles as a set of fibers arranged preferentially along the x_3, and orthogonally regarding the x_1 and x_2 directions (Fig. 2.5), the hypothesis of a transversely isotropic material is the most reasonable to model them. In addition, as discussed in Section 4.1 of Chapter 2, the muscle is assumed to be a purely elastic material, and the viscous effects are neglected. In this way, the longitudinal shear elastic modulus (μ_L) can be calculated through the shear wave velocity (V_s) measured in the fibers' direction ($V_s^{||}$) as:

$$\mu_L = \rho V_s^{||2} \qquad (3.16)$$

where ρ is the muscle density (assumed here to be 1000 kg/m^3).

Finally, maps of shear elastic modulus (Fig. 3.3C) were calculated at 1.7 Hz frequency repetition rate with a pixel resolution of 0.1 ×0.1 mm.

4.1.3 Protocol

Initially, the volunteers performed two maximal isometric voluntary elbow flexions (each lasting 5 s and resting 120 s between them) with the shoulder and elbow flexed at 90º to determine the maximal voluntary contraction (MVC). The highest MVC

value was used to normalize submaximal contractions. Then, volunteers were asked to perform six linear torque ramps (120 s rest between tasks) of isometric elbow flexion from 0-30% of MVC over 15 s. In order to correctly execute the torque ramps, they had to follow the path indicated on a monitor placed in front of them. The μ_L of BB, BR, and BA muscles was measured twice, in separate trials and random order, during the execution of the tasks. The ultrasonic scanner probe was carefully aligned with respect to the orientation of the muscle fibers. It was placed on the muscle belly, at 70% of the arm´s length distally from the acromion (BB) and 35% of the forearm length distally from the elbow (BR). As in Bouillard et al. (2012b) and Hodges et al. (2003), for the deep muscle (i.e., BA), it was placed in the medial and distal part of the arm, near the fold of the joint. To guarantee repeatability concerning the probe locations between trials, these were marked using a waterproof pen.

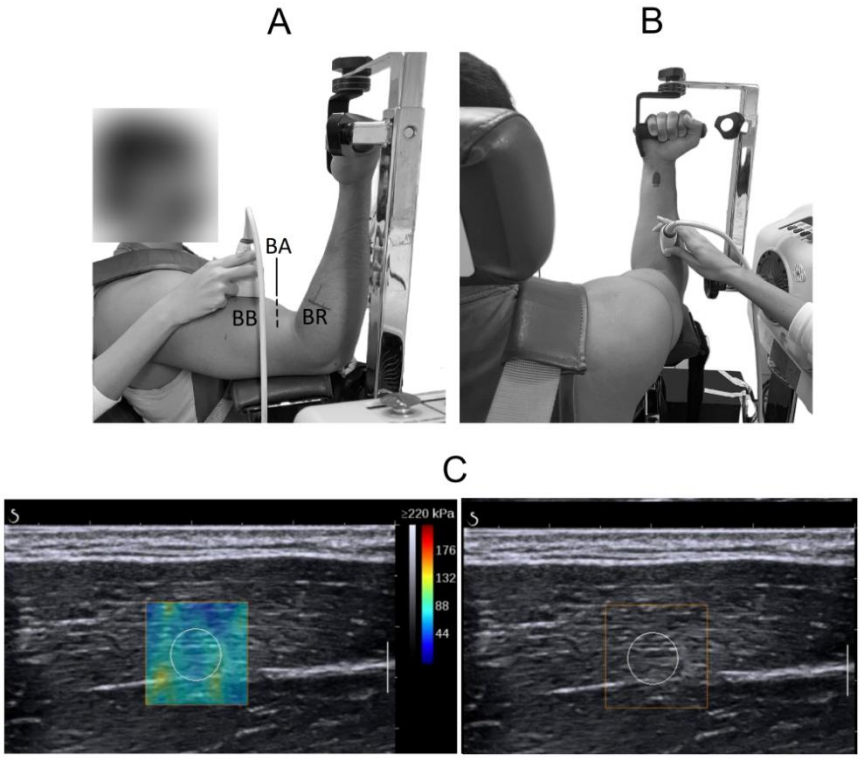

Figure 3.3. Examples of μ_L measurements. A, B: Placement of the ultrasound transducer over the free surface of the biceps brachii (BB) and brachioradialis (BR) muscles, respectively. C: Echographic image showing the ROI chosen for the measurements. At the right, the echographic image without the color map is shown. The colored region in the image at the left depicts the shear elasticity map according to the corresponding color scale. Scale bar = 0.5 cm.

4.1.4 Data analysis

For each volunteer, the mean values of $\mu_L(\tau)$ in each trial were calculated over a circular region of interest (ROI) of 1 cm in diameter placed in the middle of the elastic field (Fig. 3.3C). These data were synchronized by interpolating with the torque signal to obtain one value for every 1% MVC. Thus, for the three muscles, we calculated the $C(\tau)$ coefficients ($C_{BB}(\tau), C_{BR}(\tau), C_{BA}(\tau)$) in each trial between 0-30% MVC, as well as the averaged $\bar{C}(\tau)$ between the two trials.

4.1.5 Statistical analysis

To assess the intra-repeatability of the $C(\tau)$ coefficients obtained in both trials of the isometric flexion ramps, the intraclass correlation coefficient (ICC) was calculated for each muscle in all volunteers. On the other hand, we identified the threshold torque at which the $C(\tau)$ coefficients differed significantly from $C(0)$. We performed a repeated-measures ANOVA for each muscle (random factor: participant, between-participant factor: torque) by using PAST 3.21 (Hammer et al., 2001). As in Bouillard et al. (2012b), if a main effect was identified for torque (i.e., $C(\tau)$ changes significantly as torque increases), Duncan´s post-hoc test was applied to detect the first torque value at which the $C(\tau)$ was statistically different from $C(0)$ (we will call this point the "lower limit"). On the other hand, the "upper limit" was defined as that point followed by four smaller $C(\tau)$ values. The level of significance was set at $P < 0.05$.

4.1.6 Ligand-binding analysis

As $C(\tau)$ is directly related to the saturation fraction of the molecular receptors, we used conventional characterization methods of receptor-ligand systems to study the dynamical behavior of the elbow flexor muscles (Wyman & Gill. 1990) (Fig. 3.4). Appendices 1A and 1B provide further details about such methods. If C vs. τ

(considered as our "direct plot") describes a rectangular hyperbolic-like behavior, and the fits of all the following plots are linear with a determination coefficient (R^2) ≥ 0.90, the binding dynamics will be hyperbolic (H): 1/ C vs. 1/ τ (Lineweaver-Burk (LB) or double reciprocal plot); τ / C vs. τ (Langmuir-Hanes (LH) plot); C vs. C/τ (Scatchard (S) plot). On the other hand, if the direct plot shows a sigmoid curve and the fit of $ln(C/(1-C))$ vs. $ln(\tau)$ (Hill plot) is linear with R^2 ≥ 0.90, the binding dynamics will be cooperative (positive (C+) if slope > 1, negative (C-) if slope < 1) or non-cooperative (slope = 1). If the Hill plot has a slope less than 1, and the LB, LH, and S plots fit with R^2 ≥ 0.90, the behavior was classified as a H/C- indeterminacy, which is a common limitation when studying the interaction between receptors and ligands (Cattoni et al., 2015). We perform these analyses in the curve section delimited by the lower limit specified by Duncan´s test and the upper limit. Likewise, if the ICC values denoted a good intra-repeatability of the $C(\tau)$ coefficients between trials 1 and 2, the previous analyses were performed over the averaged $C(\tau)$ value of both trials ($\bar{C}(\tau)$).

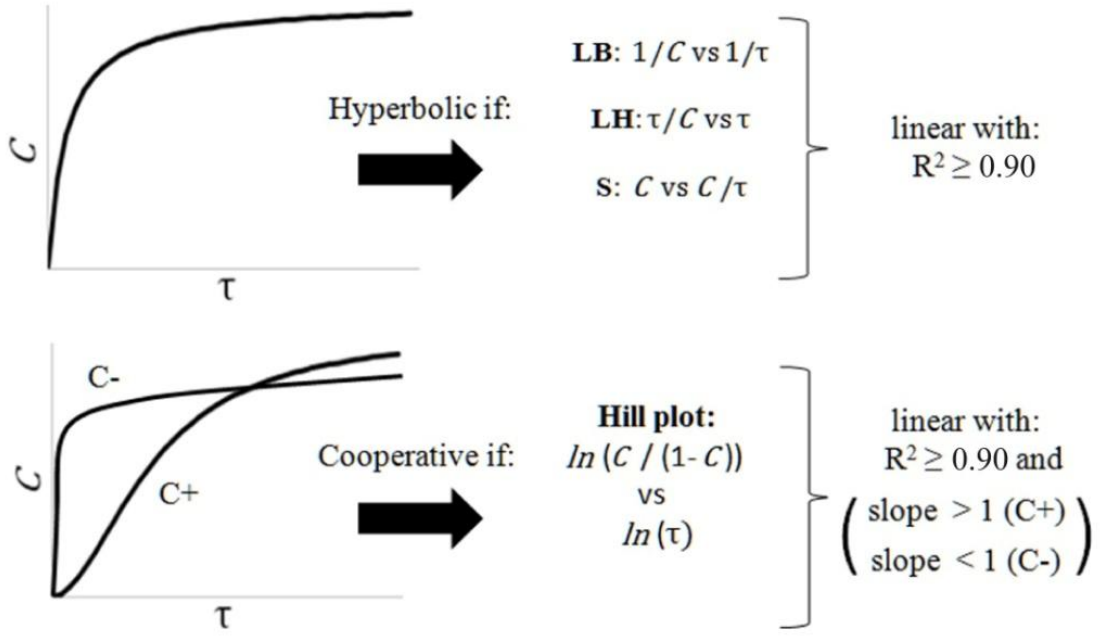

Figure 3.4. Classical rectification methods of the ligand-binding analysis. These methods were applied for the $C(\tau)$ coefficients calculated from the $\mu_L(\tau)$ values of the BB, BR, and BA muscles.

4.2 Results

From 0 to 30% MVC, the μ_L of the muscles displayed different behaviors regarding the elbow flexion torque. This can be observed by averaging the volunteers' results during the measurements (Fig. 3.5) and at the individual level (Fig. 3.6). Although the results showed some individual variability, a common trend was found. Thus, in general terms, the μ_L of the BB exhibited a slight or no increase between ~0-10% MVC, increasing rapidly between ~10-30% MVC. The BR did not show a significant change in μ_L between ~0-5% MVC, increasing its elasticity eight to nine times between ~5-20% MVC and remaining around a constant value between ~20-30% MVC. On the other hand, the BA showed a different behavior regarding the BB and BR. This muscle exhibited the earliest beginning of contraction, increasing moderately its μ_L between ~0-10% MVC, which did not change significantly between ~10-30% MVC. Table 3.1 summarizes the above regarding the average behavior of the shear elasticity for the BB, BR, and BA muscles as a function of the elbow flexion torque.

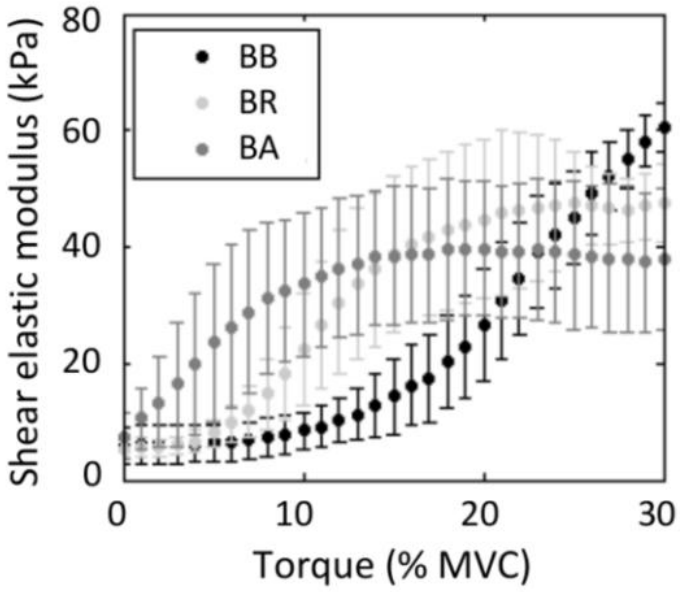

Figure 3.5. Average values and standard deviation (error bars) of $\mu_L(\tau)$ measurements for all volunteers.

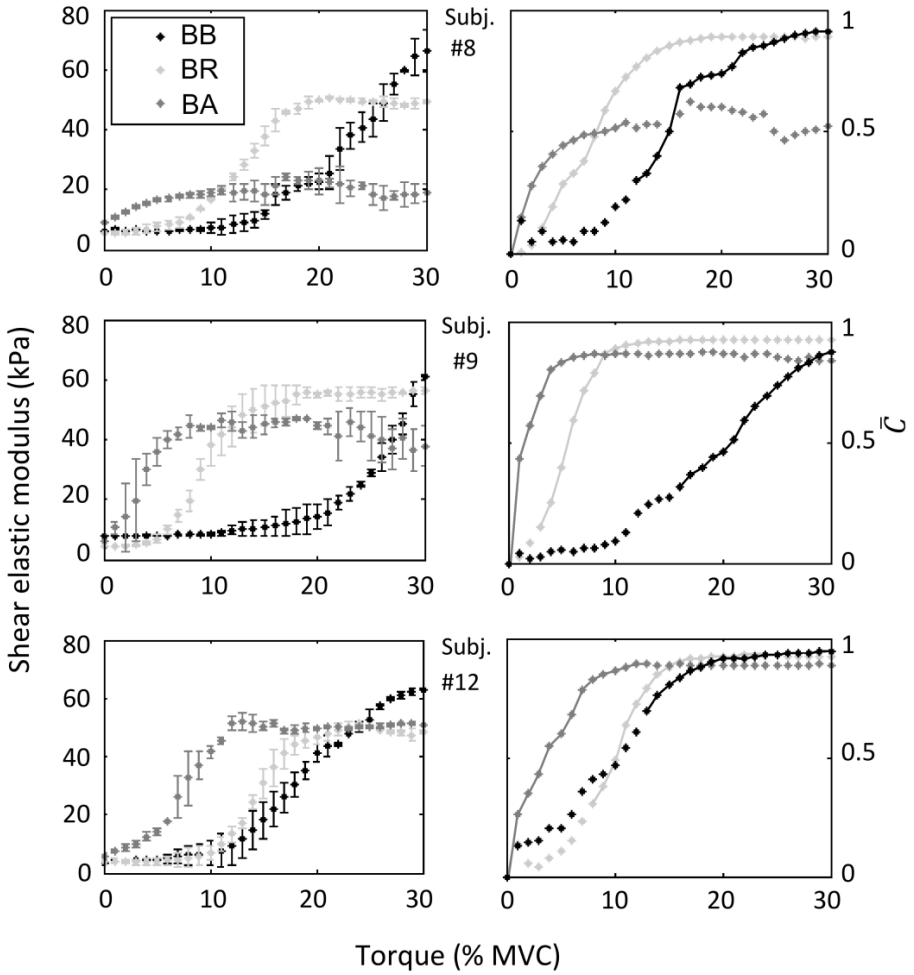

Figure 3.6. Three individual examples of the change in muscle elasticity regarding the elbow flexion torque for the BB, BR, and BA muscles. The error bar corresponds to the standard deviation of trials 1 and 2. The corresponding $\bar{C}(\tau)$ coefficients calculated from the mean value of $\mu_L(\tau)$ in trials 1 and 2 are also shown. The segments of the $\bar{C}(\tau)$ curves employed for the ligand-binding analysis, delimited by the calculated upper and lower limits, are denoted by solid lines.

Concerning the $C(\tau)$ coefficients calculated from the shear elasticity values between 0-30% MVC (Fig. 3.6 and Fig. 3.8A), the $C_{BB}(\tau)$ ranged from 0 to 0.90 ± 0.07 and 0 to 0.90 ± 0.06, while the $C_{BR}(\tau)$ did between 0 to 0.88 ± 0.05 and 0 to 0.88 ± 0.04 (first and second trials, respectively). Meanwhile, the $C_{BA}(\tau)$ varied between 0 to 0.78 ± 0.13 and 0 to 0.78 ± 0.12 (first and second trials, respectively). The high ICC obtained from these values denotes good reproducibility of the $C_{BB}(\tau)$, $C_{BR}(\tau)$, and $C_{BA}(\tau)$ coefficients, calculated from the respective $\mu_L(\tau)$ values obtained in both trials for all

volunteers (ICC_{BB} = 0.90 ± 0.08; ICC_{BB} = 0.97 ± 0.03; ICC_{BB} = 0.89 ± 0.11). In this sense, the averaged $\bar{C}(\tau)$ value for each muscle was representative of the two isometric flexion ramps. Therefore, in what follows, the analysis is performed based on the $\bar{C}_{BB}(\tau)$, $\bar{C}_{BR}(\tau)$, and $\bar{C}_{BA}(\tau)$ coefficients.

Table 3.1. μ_L values and standard deviations (between parentheses) among all volunteers for the BB, BR, and BA muscles during both isometric elbow flexion torque ramps.

		% MVC						
	μ_L (kPa)	0	5	10	15	20	25	30
BB	1st trial	5.78 (3.83)	6.32 (3.78)	9.13 (4.39)	14.38 (8.77)	26.81 (11.55)	44.71 (11.70)	61.07 (4.65)
	2nd trial	5.93 (2.81)	6.48 (2.92)	7.84 (2.70)	14.24 (4.63)	26.82 (9.96)	45.75 (10.32)	60.07 (6.52)
BR	1st trial	5.53 (1.64)	8.91 (3.30)	26.99 (11.09)	43.78 (12.08)	48.39 (9.89)	47.37 (6.38)	47.63 (7.03)
	2nd trial	5.27 (1.54)	7.16 (2.10)	19.98 (7.93)	36.58 (12.40)	44.12 (13.15)	49.28 (11.37)	48.19 (7.28)
BA	1st trial	8.40 (3.89)	24.51 (13.25)	36.22 (11.80)	40.94 (11.51)	43.43 (11.18)	44.11 (12.32)	42.66 (11.91)
	2nd trial	7.42 (3.55)	24.20 (12.48)	35.82 (11.62)	42.14 (14.07)	41.71 (12.96)	38.62 (14.45)	38.84 (14.87)

The repeated-measures ANOVA showed a significant main effect of the torque level regarding the shear elasticity for BB, BR, and BA muscles (*P* ranged from values < 1.0×10^{-5} to 0.026 in all cases). This implies that the $\mu_L(\tau)$ was significantly higher as elbow flexion torque increased. In this sense, Duncan´s test set that 11 ± 4 %MVC, 4 ± 2 %MVC, and 1 ± 1 %MVC were the averaged lower limits from which $\mu_L(\tau)$ differed significantly from rest, for BB, BR, and BA, respectively. On the other hand, the upper limits were determined at 30 ± 0 %MVC (BB), 22 ± 5 %MVC (BR), and 14 ± 5 %MVC (BA). In this way, the ligand-binding analysis revealed the presence of different contractile dynamics between the lower and upper limits of the $C_{BB}(\tau)$, $C_{BR}(\tau)$, and $C_{BA}(\tau)$ curves of all volunteers. Specifically, the BB and BR muscles show a C+ dynamic, while, depending on the volunteer, the BA muscle can present either a C+, C-,

or H dynamic. All of the above is depicted in Figure 3.7, as well as the results of the LB, LH, S, and Hill rectification methods that determine such binding behaviors.

A

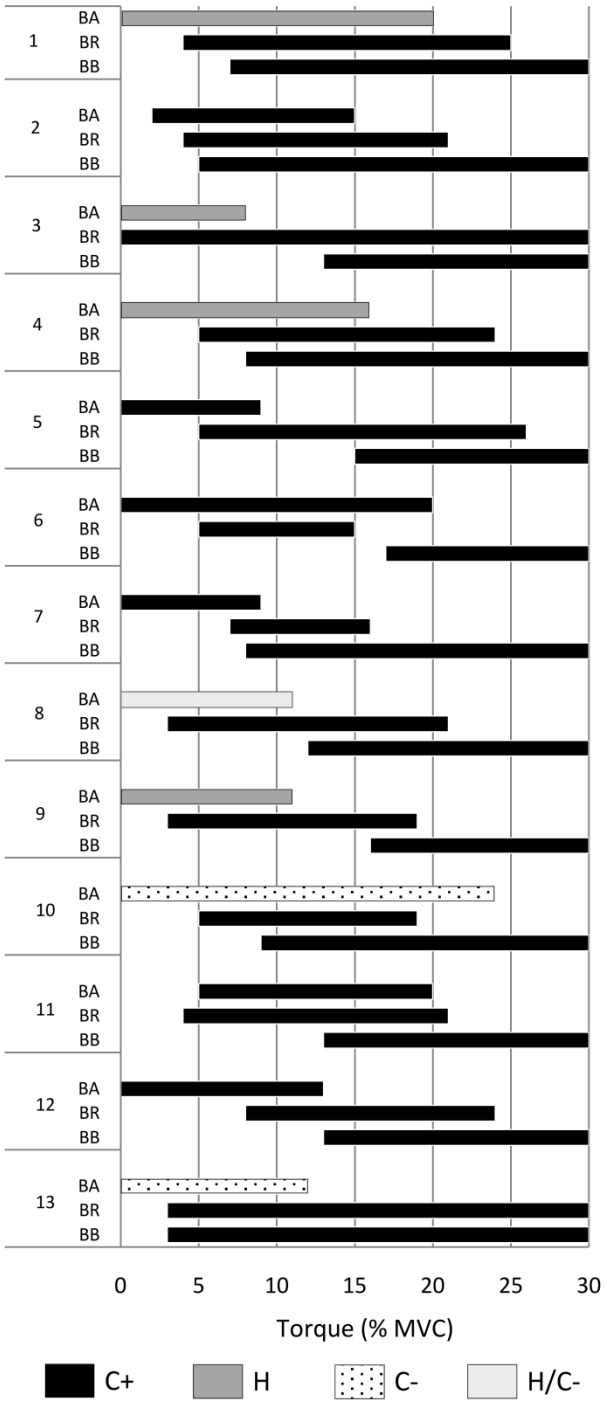

B

	R^2		
Hill (slope)	LB	LH	S
0.93 (1.05)	0.99	0.99	0.93
0.97 (1.48)	0.79	0.89	0.64
0.99 (2.16)	0.90	0.08	0.15
0.99 (1.71)	0.97	0.94	0.74
0.92 (2.21)	0.79	0.15	0.00
0.97 (2.28)	0.93	0.93	0.70
0.98 (1.02)	0.99	0.99	0.98
0.90 (1.57)	0.97	0.46	0.53
0.94 (3.72)	0.86	0.93	0.57
0.79 (0.41)	0.94	0.99	0.90
0.90 (1.60)	0.86	0.93	0.41
0.95 (2.42)	0.84	0.77	0.26
0.94 (1.45)	0.93	0.28	0.05
0.90 (1.77)	0.91	0.70	0.12
0.95 (5.08)	0.76	0.34	0.69
0.91 (1.56)	0.96	0.77	0.41
0.96 (2.98)	0.96	0.05	0.20
0.90 (4.05)	0.69	0.36	0.78
0.95 (1.22)	0.94	0.97	0.82
0.98 (2.77)	0.89	0.00	0.09
0.99 (2.84)	0.87	0.21	0.35
0.96 (0.74)	0.99	0.99	0.93
0.99 (2.35)	0.92	0.00	0.03
0.97 (3.51)	0.83	0.04	0.21
0.95 (0.97)	0.98	0.99	0.94
0.93 (2.41)	0.87	0.26	0.00
0.98 (4.50)	0.98	0.85	0.94
0.96 (0.84)	0.82	0.96	0.63
0.90 (2.50)	0.74	0.15	0.00
0.90 (2.31)	0.62	0.70	0.13
0.97 (2.85)	0.88	0.18	0.37
0.92 (1.61)	0.88	0.95	0.72
0.97 (4.72)	0.79	0.39	0.53
0.95 (1.39)	0.95	0.98	0.85
0.92 (3.26)	0.82	0.11	0.029
0.94 (2.26)	0.86	0.98	0.71
0.91 (0.79)	0.97	0.99	0.81
0.94 (1.30)	0.86	0.97	0.57
0.90 (2.00)	0.95	0.88	0.69

Figure 3.7. A: Binding dynamics as a function of the elbow flexion torque, resulting from the ligand-binding analysis performed between the lower and upper limits of $\bar{C}(\tau)$ curves for each muscle. B: R^2 values resulting from the LB, LH, S, and Hill rectification methods.

4.3 Discussion

Biomechanical and functional implications of μ_L and $C(\tau)$ in load sharing

The present work aimed to study the different contractile dynamics exhibited by the elbow flexor muscles during load sharing in isometric conditions. The SW elastography allowed the assessment of such phenomena by measuring the change of the shear elastic modulus of the BB, BR, and BA muscles as the joint torque increased. Thus, we provided additional evidence that supports the work of Bouillard et al. (2012b), who showed that at low contraction intensity levels (~ 0 - 15% MVC), torque is primarily produced by a preferential activity of BA and BR muscles (μ_L ranged from ~ 10 - 45 kPa and ~ 3 - 60 kPa, respectively), while the increase of torque between ~10 - 30% MVC is mainly due to BB (μ_L ranged from ~ 10 - 60 kPa). In this sense, as shown in Table 3.1 and Figures 3.5 and 3.6., our results concerning the torque-dependent behavior of the shear elasticity of these muscles agreed qualitatively and quantitatively with those of Bouillard et al. (2012b) and other previous studies (Grinspan et al., 2021; Lapole et al., 2015; Yoshitake et al., 2014; Nordez & Hug et al., 2010). As a general picture, the anatomical differences could account for these different behaviors among the BB, BR, and BA muscles. For example, at 90º elbow flexion, the BA has approximately half the lever arm of the BB (Murray et al., 1995; Marchese et al., 2001; Murray et al., 2002). Besides, it has a smaller cross-sectional area and is a uniarticular muscle that inserts next to the elbow joint. These features would be advantageous for developing precise movements at low force levels, thus guaranteeing the first effects of torque generation and joint stability. On the other hand, the BB and BR are biarticular muscles, supplementing the joint torque contribution with slightly higher force levels than BA to additionally stabilize the shoulder and wrist joints. The BB is able to increase the torque to higher levels, helped by their long-moment arm (Bouillard et al.,

2012b). Compared to BB and BA, the BR has the longest lever arm but the smallest cross-sectional area, thus playing an intermediate role concerning control and torque generation. This muscle is anatomically arranged differently from the BB and BA to provide joint stability by coaptation of the radius in the joint. As the BB, the BR is a biarticular muscle and ensures that the BB does not lift the radius head, expecting a low torque production from it. Thus, it accompanies the BB at the beginning of the contraction, maintaining a constant contribution afterward.

In addition to the inter-muscle anatomical differences, the inter-participant differences regarding the moment arms, cross-sectional areas, and the muscle recruitment thresholds can explain the variability of the shear elasticity vs. torque measurements across the volunteers (Hug et al., 2010; Bouillard et al., 2012b). On the other hand, the different fiber compositions of the muscles must also be considered. The percentage of type I fibers varies, within the 95% confidence limits, from 34-51% for BB surface fibers, 40-60% for BB deep fibers, and 30-53% for brachioradialis fibers. Concerning the type II fibers, these proportions are 49-66%, 39-60%, and 47-73%, respectively (Johnson et al., 1973). These differences in fiber-type distribution between muscles could also explain the different behaviors characterized.

This study provides a new conceptual framework for assessing the load distribution between synergistic muscles. The above, combined with measurements of $\mu_L(\tau)$, moment arms, and cross-sectional areas, can be of high interest to precisely study the compensations between individual muscle torques (Bouillard et al., 2012b). In this regard, the calculation of $C(\tau)$ coefficients from the $\mu_L(\tau)$ values and the subsequent addition of the ligand-binding framework into the load-sharing analysis revealed the presence of hyperbolic and cooperative behaviors. This finding complements, from a functional point of view, the previous comments regarding the anatomical features that

could explain the behavior of each muscle during the load sharing. In this way, our results clearly differentiate the behavior exhibited by the BA from those of the BB and BR. While the BA can display both H, C+, or C- dynamics associated with the torque production at low contraction intensity levels (~ 0 - 10% MVC), the BB and BR muscles only show C+ dynamics related to the intermediate-high efforts (~ 10 - 30% MVC) (Fig. 3.7). As we will discuss later, the causes for which the BA exhibits its particular behavior may reside in peculiarities inherent to its contraction mechanism. Nevertheless, we must also consider the possible incidence of the pennation angle to account for the BA results since the muscle shear elastic modulus decreases as this angle increases (Gennisson et al., 2010). This does not have an incidence in the BB muscle as this is a fusiform muscle, nor in the BR since its pennation angle is low (~ 2º) and is minimally affected by the contraction (Bouillard et al., 2012b; Lieber et al.,1992). On the contrary, in the BA muscle, the pennation increases by 7.7º from rest to 50% MVC, mostly at contraction intensities below 10% MVC (Hodges et al., 2003). Thus, as in Bouillard et al. (2012b), our measurements of μ_L may present some bias at the beginning of the contraction. The above could have influenced the $C_{BA}(\tau)$ calculated within ~ 0 - 10% MVC, where the H, C+, or C- dynamics appear. Further studies on shear wave propagation in pennate muscles are needed to obtain unbiased results by correcting the incidence of the pennation angle in the shear elastic modulus estimation.

Although it is common practice in muscle elastography to consider only the elastic properties of the muscle, these also exhibit viscoelastic properties. Therefore, the possible incidence of the viscosity in the results should also be discussed. In this respect, Rudenko et al. (2014) have shown that the dissipative properties of muscles are determined by the fourth-rank viscosity tensor, which, as the elastic properties, has two independent components. In our experimental protocol, two types of viscous behavior

play a role. The first one is a longitudinal viscosity associated with muscle contraction. Previous works performed in the gastrocnemius medialis and the soleus show that longitudinal viscosity effects are relevant in a time scale of ~ 10^{-1} s or lower (Desplantez et al., 1999). Therefore, the longitudinal viscosity effects can be neglected for contraction rates that comprise longer times. This is the case in our experiments since the total ramp time was 15 seconds, and we sampled the shear elasticity with a frame rate of 1.7 Hz. The second one is the shear viscosity, associated with the shear wave propagation after the "push" of acoustic radiation force. Previous works used Voigt's linear viscoelastic model to estimate the shear viscosity of biceps brachii from dispersion curves using an SSI device (Gennison et al., 2010). The results show that shear viscosity increases for loaded muscles concerning its rest position, from ~ 1 Pa·s at rest to ~ 3.5 Pa·s for muscles loaded with 4kg. However, the increase in viscosity does not produce a significant variation in the shear wave speed compared to the value obtained by neglecting the viscosity. In other words, the slope value of the shear wave speed vs. frequency curve is much lower than 1 (~ 1/600 $ms^{-1}Hz^{-1}$). Thus, the results and conclusions reported in our work are not biased by neglecting viscous effects in our model.

Leaving aside the above considerations, it is important to note that the same results are obtained when performing the analysis using the data provided by Bouillard et al. (2012b) (Fig. 3.8). Here, the rate of contraction was slower than our protocol, as the ramps were from 0 to 40 %MVC in 30 s. Nevertheless, the ligand-binding analysis for the data of Bouillard et al. (2012b) denotes the same dynamical behaviors as our results. This shows the consistency of the elastography-driven approach proposed in the present work to assess the different contractile dynamics that could be behind the muscle synergism of the elbow flexors muscles.

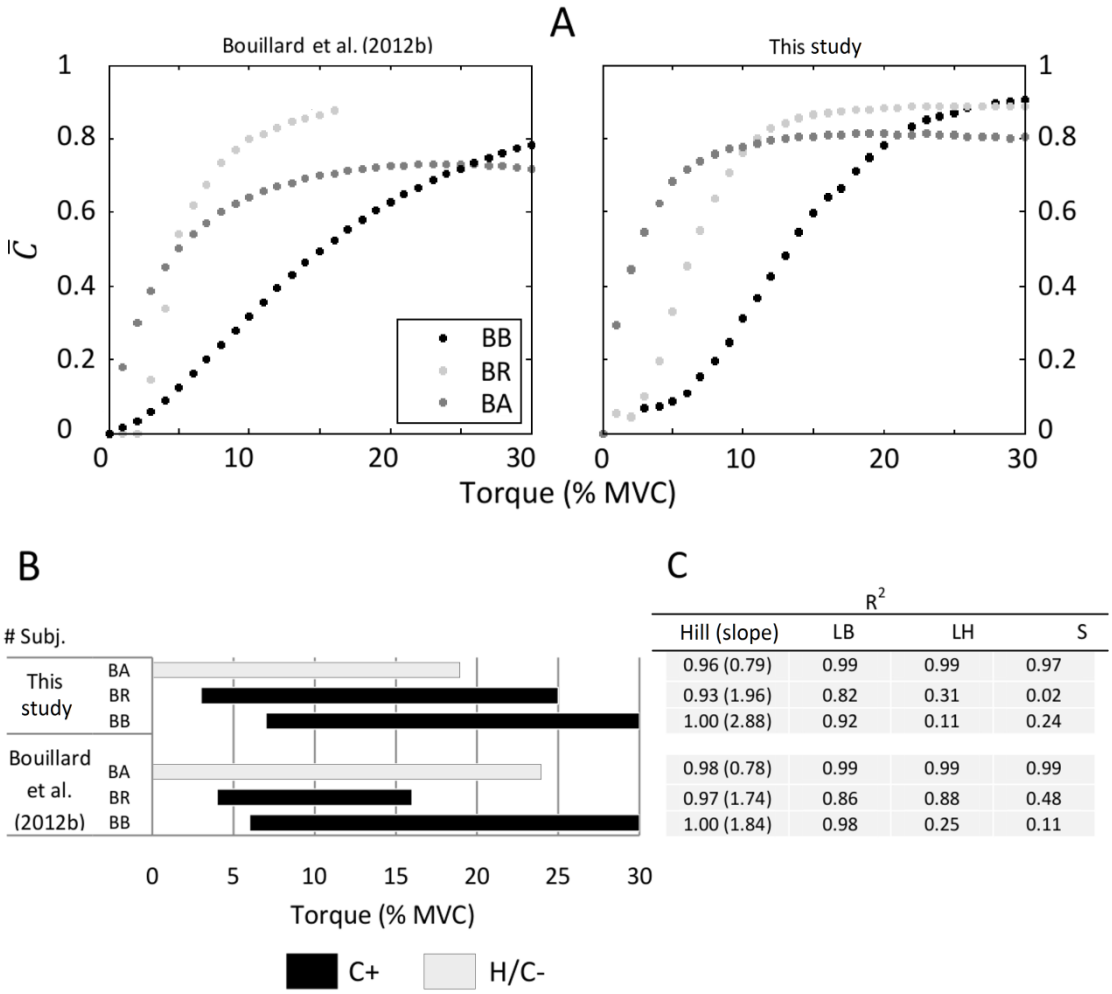

Figure 3.8. A: Comparison of the $\bar{C}(\tau)$ coefficients calculated from data of Bouillard et al. (2012b) and those of this study (mean values of Fig. 3.5). It should be noted that in Bouillard et al. (2012b), it was not possible to obtain μ_L values for BR beyond 16% MVC. B: Ligand-binding behaviors obtained from $\bar{C}(\tau)$ values in each study. C: R^2 values resulting from the LB, LH, S, and Hill rectification methods.

The biomechanical significance of $C(\tau)$

The present study sheds light on the nature of the coefficients $C(\tau)$. Equations (3.10) and (3.12) state that $C(\tau)$ coefficients are related to variables changing in the muscle fiber direction. They depend exclusively on the longitudinal shear elastic modulus (μ_L) and are directly proportional to the longitudinal strain of the muscle (ξ_L). According to the acousto-elasticity theory, the longitudinal stress in muscle varies linearly with respect to the square of the shear wave velocity in the fiber direction, and thus, with its μ_L (Gennisson et al., 2007; Destrade et al., 2010; Remeniéras et al., 2021).

Likewise, the SRS principle states that the longitudinal shortening of the muscle increases its Young´s moduli along the muscle fibers, which depends exclusively on μ_L (Zonnino et al., 2019; Eby et al., 2013; Section 2.2). Thus, the SRS principle and the acousto-elasticity theory link ξ_L and μ_L with the shear wave propagation and the contractile processes that determine the shortening in the longitudinal direction of skeletal muscle during the isometric contraction. In this way, the present work provides a novel manner to assess the relative longitudinal deformation of the muscle at increasing levels of isometric force by calculating $C(\tau)$ exclusively from elastography measurements.

From a functional point of view, the above could also have significance regarding the kinetics of the longitudinal shortening of muscle as the joint torque increases. In particular, it would imply that the length in the fibers' direction shortens at an increasing, constant, or decreasing rate, depending on whether the dynamics of $C(\tau)$ is C+, C-, or H, respectively. Thus, our results for the elbow flexors muscles imply that, at low contraction intensity levels (~ 0-15% MVC), the flexion torque is primarily produced by the BA muscle, which displays an H or C- dynamic, thus shortening at a constant or decreasing rate, respectively. On the other hand, the increase in torque after ~ 10-15% of MVC is mainly due to the BB and BR muscles, which follow a C+ dynamic characterized by an increasing rate of shortening. In this sense, these results imply that such shortening dynamics determine the torque-dependent changes in load sharing between the BB, BR, and BA muscles during the isometric flexion of the elbow joint. Besides, they could also account for explaining the non-linear relationship between electromyographic activity Vs. torque, in addition to the activation pattern of the motor units classically reported in previous works (Lawrence and De Luca,1983; Zhou and Rymer, 2004; Nordez and Hug, 2010).

Related to their direct proportionality concerning ξ_L, our results suggest that $C(\tau)$ could indicate the amount of the attached actin-myosin cross-bridges as a function of the joint torque level. In this regard, as we show in Section 3.2, such coefficients are closely related to the saturation fraction of molecular receptors (Y ∈ [0, 1]), which is measured by indirect methods (e.g., absorbance measurements) to characterize the ratio of occupied binding sites/total binding sites as the ligand concentration increases (Wyman & Gill. 1990). Besides, as discussed below, several previous ligand-binding studies performed on isolated myofilaments have shown the same dynamical behaviors as the $C(\tau)$ coefficients. Presumably, all the above could imply a link between the micro and macro-scale phenomena associated with muscle contraction, which derives from the SRS principle and the acousto-elasticity theory. This is in good agreement with previous work that has proposed that the SRS principle may provide a measure of the amount of the attached cross-bridges and the contribution of the muscle to joint stiffness (Van Eesbeek et al., 2010). In this respect, it should be noted that this type of micro-macro link has already been observed for other biomechanical properties of skeletal muscle. For example, the force-velocity relation of Hill´s muscle model (Hill, 1938) can be supported from a molecular perspective. This hyperbolic force-velocity relationship of muscle has been classically regarded as a pure empirical description of the macroscopic force-velocity data (Huxley, 1957; Huxley et al., 1971). However, recent works have established the relationship between the mechanical manifestation in terms of force-velocity data and the kinetics of the cross-bridge cycle driven by ATP hydrolysis, describing how the molecular events within such a process can be transformed into the hyperbolic Hill equation (Zhao et al., 2022; Seow & Seow, 2022).

Interpretations on the cross-bridges binding dynamics during muscle synergism

The appearance of ligand-binding behaviors, such as hyperbolic and cooperative dynamics, is highly significant. It is important to note that different molecular receptors, for example, hemoglobin and myoglobin, typically exhibit these behaviors. Such molecules have binding sites for their ligands, with specific affinity constants depending on the saturation level and the degree of allosteric modulation. This determines the kinetic behavior of the saturation fraction (Y) between the occupied and total binding sites as the ligand concentration increases. The above is analogous to what happens with the actin filament active sites and the myosin heads (subunit S1) during muscle contraction. Here, the actin-troponin-tropomyosin complex (regulated actin) determines muscle contraction and relaxation by mediating the interactions between the myosin heads and the actin filaments (Lehrer and Morris, 1982). The above depends on specific biochemical factors. Specifically, in absence of Ca^{2+}, such a complex causes the muscle to relax by inhibiting the acto-S1 ATPase activity and blocking the binding of S1 to actin. On the other hand, in the presence of Ca^{2+}, actin binds to the S1·ADP-Pi complex and activates ATPase, which accelerates phosphate loss and determines muscle contraction (Lehrer & Geeves, 1998; Greene and Eisenberg, 1988). Therefore, the actin-troponin-tropomyosin complex regulates the blockade of the actin active sites to myosin heads, thus modulating their binding affinity and the fraction of the myosin heads attached to the actin active sites (Haselgrove, 1973; Huxley, 1973). Since there is a direct relationship between the Y of a molecular receptor and the fraction of the myosin heads attached to the actin active sites, that is, $C(\tau)$ (Section 3.2), our results suggest that hyperbolic and cooperative behaviors (+/ -) exhibited by the longitudinal shortening of the BB, BR, and BA muscles during their synergistic action, could have its correlate at the molecular level. In this sense, a plausible interpretation for our results is that such

ligand-bind dynamics underlie the specific contraction pattern of each muscle, thus determining the intrinsic cross-bridge formation while load sharing as torque increases.

Previous works in solution and isolated muscle fibers could support this interpretation regarding the possible contractile intrinsic mechanisms involved in muscle shortening during synergism. Such studies have shown that receptor-ligand behaviors are manifested in the dynamics of actin-myosin interactions during the reciprocal sliding of the contractile myofilaments (Shchepkin et al., 2017; Lehman, 2017; Reshetnyak et al., 2012; Rao et al., 2009; Zot et al., 2009; Tobacman & Butters, 2000; Lehrer & Geeves, 1998; Greene & Eisenberg, 1988; Lehrer & Morris, 1982; Greene & Eisenberg, 1980; Porter & Weber, 1979). For example, Lehrer & Geeves (1998) showed that when the tropomyosin is bound to actin with a stoichiometry of 1 Tm/7 actin subunits, the ATPase activity versus [S1] becomes sigmoid, indicating C+ binding of S1·ATP to actin-tropomyosin. On the other hand, Greene and Eisenberg (1980) studied the binding of myosin heads to the unregulated and regulated actin in the presence of ADP. They found that the S1·ADP complex binds independently (hyperbolic) to the unregulated actin, but it can bind with C+ to regulated F-actin, both in the presence and absence of Ca^{2+}. In this respect, the density of attached myosin heads to actin per unit length of thin/thick filament overlap is tightly regulated by the concentration of this ion and by the kinetics of the interactions of the regulatory proteins to the actin (Mijailovich et al., 2019). For example, the elastic properties of skeletal muscle reside primarily on the protein titin, which binds to actin in the presence of Ca^{2+} (Linke et al., 1996). The above suggests a mechanism that can explain the dynamic response of the muscle to active changes in length (Nishikawa, 2020). Tropomyosin phosphorylation is another molecular mechanism that induces ligand-binding behaviors among contractile filaments in muscle. This was studied by Rao et al. (2009), who

carried out a force protocol related to the present study. Specifically, they measured the isometric force/length ratio versus the density of attached myosin heads during a linear force ramp, where the myosin molecules moved reconstituted actin filaments with phosphorylated or dephosphorylated tropomyosin. Their results showed that the actin filament is cooperatively activated by myosin when tropomyosin is phosphorylated. In contrast, when tropomyosin is dephosphorylated, the actin filament behaves hyperbolically. Thus, this work showed that phosphorylation is essential for long-range cooperative activation along the actin filaments. Concerning the C- behavior, Reshetnyak et al. (2012) studied that the binding of the myosin heads to one (state 1) or two (state 2) actin monomers depends on an association constant, which decreases as the myosin heads/actin ratio increases due to the growing steric restrictions. According to these authors, this C- transition from state 1 to state 2 might be associated with force generation and directed movement.

Based on the above, the results of the present work encourage further research to understand how the microscopic processes involved in muscle contraction are manifested at a macro-level in the whole muscle. In this context, we afford a new conceptual and experimental framework to extend the current applications of elastography in muscle biomechanics. Thus, we provide the first results assessing the longitudinal shortening of skeletal muscle through elastography and a ligand-binding approach, suggesting a plausible link to the molecular phenomena underlying muscle functions. On this matter, it should be pointed out that muscle contraction does not depend solely on the characteristics of the cross-bridge binding, so these molecular interpretations could partially explain the characterized muscle mechanical properties. In addition, we are aware that additional evidence from more direct characterization methods is needed to confirm the predictions of the present work regarding the

contractile dynamics at the sarcomere level. We believe the microendoscopy could be helpful in this regard (Sanchez et al., 2015; Chen et al., 2020; Adkins et al., 2022). Beyond these considerations, the data and methods described here could be the basis to continue delving into the implications of the ligand-binding behaviors in skeletal muscle biomechanics. For example, this work could contribute an advance regarding the estimation of individual muscle forces through elastography, as previous studies have proposed (Bouillard et al., 2012a; Bouillard et al., 2011; Hug et al., 2015a; Zonnino et al., 2019). This challenge will be addressed in the next Chapter of this thesis.

5 – CHAPTER CONCLUSIONS

The present chapter provides a new framework to assess load sharing during torque production by characterizing the longitudinal deformation of synergistic muscles through measurements of its shear elasticity. In particular, it describes a novel elastography-driven approach to characterize the distinctive role of each synergistic muscle in generating the total joint torque during the isometric flexion of the elbow joint. This approach allowed obtaining the $C(\tau)$ coefficients from the μ_L values of the BB, BR, and BA, which exhibited typical ligand-binding dynamics that could be related to the different functions of each muscle in force generation as torque increases. Specifically, the results suggest that the H, C+, and C- dynamics could be the underlying mechanisms, at the molecular level, of the contractile behavior of each synergistic muscle during the load-sharing. In addition, based on the direct relationship between $C(\tau)$ and the saturation fraction Y, our results also suggest that this coefficient could indicate the amount of cross-bridges attached as a function of torque. Therefore, the work presented in this chapter extends the applications of elastography by showing its potential usefulness in inferring contractile processes at different scales that determine the biomechanical properties of the whole skeletal muscle.

CHAPTER 4

ESTIMATION OF INDIVIDUAL MUSCLE FORCES THROUGH ELASTOGRAPHY

1 – INTRODUCTION

Understanding how the central nervous system manages the force sharing between muscles is critical in many fields, such as motor control, biomechanics, and robotics. This requires accurate quantification of the force produced by each muscle (Hug et al., 2015a). However, over the years, estimating the individual muscle forces has remained an unsolved problem in muscle biomechanics. Thus, as standard practice when assessing muscle forces, the net joint moment is measured by isokinetic dynamometry. However, the above quantifies the global force produced by all the muscles involved, not their individual contribution. In this regard, the lack of a suitable approach to calculate individual muscle forces currently represents a gap in our comprehensive understanding of muscle functions.

Muscle redundancy is a characteristic of the musculoskeletal system that involves having more muscles than degrees of freedom of movement. This grants the central nervous system (CNS) numerous options to perform a task (Kutch et al., 2011). Even single-joint motor tasks can theoretically be produced by an infinite number of combinations of individual muscle forces (Hug et al., 2015a). Thus, determining such forces is a classic indeterminate problem. In this sense, it is not possible to obtain a unique solution as the unknowns (individual muscle forces) outnumber the equations derived from the measurable properties of the system. Many approaches have been developed to solve this indeterminate problem. For example, in the elbow, the shared forces between synergistic muscles were previously estimated based on arbitrarily assumed ratios (Simpson et al., 1975; Nicol, 1977). Another simple alternative consisted

of reducing the excess of unknown variables by grouping functionally similar muscles (Messier et al., 1971). Other alternative methods were also formulated based on the hypothesis that the force distribution between muscles depends on their cross-sectional area during maximal forceful activities (Hui et al., 1987; Pauwels. 1980; Amis et al., 1980). These earlier efforts have served as a starting point for developing more sophisticated and comprehensive approaches.

One of these approaches has been the development of musculoskeletal models to quantify individual muscle forces. In this matter, Erdemir et al. (2007) provided an exhaustive review of them. Here, optimization approaches are employed to solve the indeterminate problem and assess the load sharing between muscles (An et al., 1984). In this sense, static optimization is one of the classic approaches in the literature (Raikova & Aladjov, 2003). It is characterized by searching for muscle forces that minimize a cost function and fulfill constraints, given basically by bounded muscle forces and equations of motion or joint moments. The cost functions are mathematical expressions assumed to model some physiological criteria optimized by the central nervous system during a particular activity (Ackermann & Schiehlen, 2009). Despite being computationally efficient, an important limitation of this approach is that it neglects essential aspects of muscle physiology concerning force production. In this regard, modified static algorithms have been developed as an alternative by considering the muscle activation and contraction dynamics, requiring a low computational effort (Erdemir et al., 2007; Ackermann and Schiehlen, 2009). However, their validity cannot be established due to the absence of experimental techniques to quantify and compare their predictions (Erdemir et al., 2007; Hug et al., 2015a).

In this regard, several studies have proposed using surface electromyography (EMGs) to characterize the individual muscle forces. For example, the pioneer works of

Messier et al. (1971) and Cnockaert et al. (1975) have used this methodology to estimate the individual forces of the biceps brachii, brachioradialis, and triceps brachii muscles during static tasks from the equilibrium moment equation about the elbow joint. They approached the indeterminate problem by assuming that the EMG activity of a skeletal muscle is directly related to the force it exerts, and that all the muscles contributing to flexion and extension of the elbow joint can be grouped and represented by the biceps and triceps brachii, respectively. More recently, other novel approaches, including processing using neural networks (Luh et al., 1999; Rosen et al., 1999; Wang & Buchanan, 2002; Schöllhorn et al., 2004) and EMG-driven models (Lloyd et al., 2003; Shao et al., 2009; Menegaldo et al., 2014), were also been proposed to calculate both joint moments as well as individual muscle forces. However, this approach is currently discussed due to the electrical nature of the EMG measures. Although EMG can be used to quantify the neural drive of muscles and, thus, to study the neural control of muscle coordination during isometric and dynamic contractions, the EMG signal is susceptible to many physiological and non-physiological factors. For example, the amplitude of the signals is affected by the placement of the electrodes and by the tissue conductivity (De Luca, 1997). Besides, due to the well-known force-length relationship, different muscle forces can be produced for the same activation levels if the muscle operates at different lengths. Furthermore, the EMG is not susceptible to the production of passive forces (Hug et al., 2015a). In addition, the presence of neuromuscular fatigue alters the relationship between EMG amplitude and force (Edwards et al., 1956). All of these factors limit the usefulness of EMG for accurately measuring muscle force. Consequently, the estimation of individual muscle force remains one of the main challenges in biomechanics (Hug et al., 2015a).

In this context, in recent years, elastography has begun to be widely used in muscle biomechanics research. Particularly, shear wave elastography (SWE), has provided a novel way to measure the change in the mechanical properties of such tissue, thus driving a new approach in the studies within this field. Currently, supersonic shear imaging (SSI) is the gold standard SWE methodology for characterizing the longitudinal shear elastic modulus (μ_L) of skeletal muscle *in vivo* and non-invasively (Bercoff et al., 2004a). The main advantage of this method is that it combines high-frequency ultrasonic waves with low-frequency waves (100 ~ 1000 Hz), thus exhibiting high spatial resolution (< 1 mm) and good contrast in the characterization of μ_L (Grinspan et al., 2021). Compared to the EMG, the mechanical and non-electrical nature of the estimates obtained through this methodology makes it a good alternative for estimating muscle forces.

Thus, previous studies have shown that μ_L is linearly related to both active and passive joint torques (Hug et al., 2015a). In this regard, Bouillard et al. (2011) showed the possibility of estimating the torque accurately from SSI measurements in the little finger abductor muscles, by assuming that the torque (τ) measured during isometric contractions is directly related to the force produced by the muscle. Besides, Ates et al. (2015) studied the relationship between muscle elasticity and torque during the isometric abduction of the little finger, demonstrating a linear relationship over the entire range of torque. On the other hand, Bouillard et al. (2012a) assessed the effect of fatigue for determining an index of individual muscle force from SSI measurements during an isometric fatiguing contraction, showing the ability of the shear elastic modulus to provide an accurate index of muscle force in such conditions. Likewise, this work also studied the relationship between the changes in muscle elasticity with muscle synergism and force production in the knee flexors and extensors muscles in fatiguing

conditions, showing its utility to document changes in load sharing during submaximal isometric fatiguing contraction. Similarly, Bouilard et al. (2012b) provided evidence of the torque-dependent changes in the load-sharing between the elbow flexor muscles under normal conditions, which partially explains the non-linear EMG-torque relationship classically reported for the biceps brachii muscle during isometric efforts. More recently, Zonino et al. (2019) and Smith et al. (2023) employed magnetic resonance elastography (MRE) to simultaneously measure the shear elasticity of forearm muscles and the torque applied by the wrist joint during isometric tasks. The results showed increases in the shear wave speed squared (SWSS) during varying levels of contraction and signs of co-contraction activation with agonist and antagonist activity. Such data were employed as inputs of a muscular model, in which the individual muscle force contributions are related to the corresponding SWSS and a set of muscle-specific proportionality constants. However, similarly to other works, the force results of this study were expressed in terms of normalized SWSS, not in Newtons. Thus, although the previously referred studies have provided the basis to continue delving into the application of elastography to estimate individual muscle forces, it is still necessary to develop a way to retrieve such forces in Newtons, directly from experimental values of muscle elasticity. In addition, as static optimization, the referred approaches do not consider dynamic aspects of muscle contraction, which are related to the change of μ_L as the muscle generates force.

Concerning the above, since the force developed by a muscle varies linearly regarding the muscle length (Granzier et al., 1991; Rassier et al., 1999; Maganaris, 2003), which depends on the degree of overlap of the actin and myosin filaments as the cross bridges form, the approach developed in Chapter 3 may be useful for calculating individual muscle forces. As has been seen, this approach integrates the receptor-ligand

binding framework related to the actin-myosin cross-bridges formation, with the SRS principle and the acousto-elasticity theory. Here, by calculating the coefficients $C(\tau)$ directly from experimental $\mu_L(\tau)$ data, it is possible to account for the dynamics of the longitudinal deformation due to the cross-bridges formation, which is the basis of the muscle force-generating mechanism. Thus, the objective of the present Chapter is to integrate this approach within a static optimization model based on elastography, which allows the calculation of the individual muscle forces during contraction. In this way, this new approach is applied to estimate the muscle forces developed during the isometric elbow flexion, thus providing a novel way to characterize the individual forces produced by the BB, BR, and BA muscles during their synergistic action.

2 – THEORY OF STATIC OPTIMIZATION

The static optimization is an efficient approach to address the indeterminate problem presented previously concerning the estimation of individual muscle forces. This makes it possible to solve the load-sharing problem for each instant independently. By considering the underdetermined system $Ax = b$, such an approach is based on the assumption of an instantaneous cost function $G(x)$. Here x is an admissible solution representing the vector of muscular forces that minimizes such a function at each moment (Heintz, 2006; Ackermann & Schiehlen, 2009).

Since skeletal muscles only generate positive forces, it is necessary to include some constraints to the system. In this way, this optimization problem can be formulated as follows (Heintz, 2006):

$$\begin{gathered} \text{minimize } G(x) \\ \text{subject to: } \begin{cases} h(x) = 0 \\ u(x) \leq 0 \end{cases} \end{gathered} \tag{4.1}$$

where $h(x)$ states a series of equality constraints and $u(x)$ a set of inequality constraints (Bertsekas, 2014). Here, the equations of equilibrium determine the equalities, while the possible muscle forces determine the inequalities.

A system based on equilibrium equations, $Ax = b$, together with a cost function, $G(x)$, can be solved with the help of Lagrange multipliers. This leads to:

$$L(x, \lambda) = G(x) + \lambda^T (Ax - b) \qquad (4.2)$$

where λ is a set of Lagrange multipliers. In this way, the minimum constrained solution is found by equating the differentials of the Lagrange equation to zero:

$$\begin{pmatrix} \frac{dL}{dx} \\ \\ \frac{dL}{d\lambda} \end{pmatrix} = 0 \qquad (4.3)$$

Thus, if we want to calculate the muscle forces around some joint of the upper limb according to the static optimization, it will be necessary to perform the procedure discussed previously such that minimize $G(x)$ subject to the following equality constraint:

$$\sum_{i=1}^{M} \vec{r}_i \times \vec{x}_i = \sum \vec{\tau}_{ext} \qquad (4.4)$$

where $\overrightarrow{x_i}$ is the muscular force of the *i*-muscle, $\overrightarrow{r_i}$ is the corresponding moment arm, and $\vec{\tau}_{ext}$ is the external joint torque. Note that the moment equilibrium constraint is written as one part reflecting the load carried by the system (b), and one part with the unknown muscular forces multiplied by their respective moment arms (Ax). Adding additional constraints, such as minimum or maximum values for the unknown forces, an extra set of Lagrange multipliers can be added to the Eq. (4.2):

$$L(x, \lambda) = G(x) + \lambda^T (Ax - b) + {\lambda_L}^T x_L \qquad (4.5)$$

For example, if the x_i are not allowed to become negative, the constraints $x_i \geq 0$ are introduced by including in x_L the components x_i.

On the other hand, when the set of variables and parameters makes the system underdetermined, it will be necessary to apply numerical methods to solve the indeterminacy problem under the static optimization approach. For example, one alternative is to use the Moore-Penrose pseudoinverse A+, which is a classical numerical method that solves an underdetermined system $Ax = b$, thus obtaining the solution x with minimum Euclidean norm (Strang, 1988). This approach has been previously used to assess muscle forces by Yamaguchi et al. (1995). Today, various software packages include optimization algorithms based on these and other numerical methods, which are widely used in several fields of science to address underdetermined problems through optimization theory.

3 – ESTIMATING INDIVIDUAL MUSCLE FORCES DURING ISOMETRIC ELBOW FLEXION THROUGH ELASTOGRAPHY

3.1 Elastography-driven static optimization model

The elbow joint during the isometric flexion was modeled by considering a one-degree-of-freedom joint in the sagittal plane. The shoulder and elbow flexion angle were set at 90º, and the forearm in a supine position (Figure 4.1). We modeled a linear torque ramp of isometric flexion from 0 to 30% MVC, as was performed experimentally in Chapter 3. Three synergistic flexor muscles (BB, BR, and BA) contract, transmitting forces to the elbow joint through the insertion tendon, thus producing the internal torques that distribute and balance the load. Concerning the previous Section, to find the individual muscular forces, it will be necessary to minimize the following function regarding the sum of such internal torques (τ_{int}):

$$G(x) = \sum \vec{\tau}_{int} = \sum_{i=1}^{3} \vec{F}_i \times \vec{r}_i \qquad (4.6)$$

where $i = (1, 2, 3)$ represent the BB, BR, and BA muscles, respectively. On the other hand, as in isometric and static conditions the net torque ($\vec{\tau}_N$) across the joint is zero, Eq. (4.6) must equal the sum of the external torques ($\vec{\tau}$). Due to position of the arm considered in the model, only the applied force ($\vec{F}$) contributes to $\vec{\tau}$. Thus, during the isometric elbow flexion at θ = 90º, the following balance equation must be satisfied:

$$\vec{\tau}_N = 0 \Rightarrow \vec{F}_{BB}.\vec{r}_{BB} + \vec{F}_{BR}.\vec{r}_{BR} + \vec{F}_{BA}.\vec{r}_{BA} = \vec{F}.\vec{L} = \vec{\tau} \qquad (4.7)$$

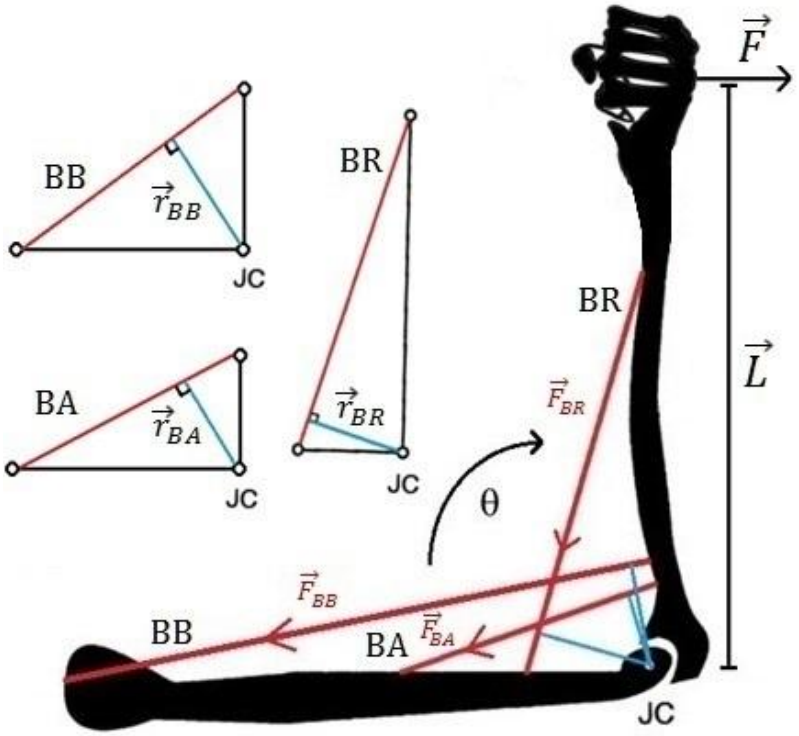

Figure 4.1. Isometric elbow flexion model. The force vectors and lever arms corresponding to the action of the biceps brachii, brachioradialis, and brachialis muscles are displayed ($\vec{F}_{\text{BB}}$, $\vec{r}_{BB}$; $\vec{F}_{\text{BR}}$, $\vec{r}_{BR}$; and $\vec{F}_{\text{BA}}$, $\vec{r}_{BA}$, respectively). JC: Joint center of rotation; θ: elbow flexion angle; $\vec{L}$: lever arm corresponding to the applied force ($\vec{F}$).

We also included the following inequality constraints regarding the maximal and minimal values of $\vec{F}_i(\tau)$:

$$0 \leq \left|\vec{F_i}(\tau)\right| \leq \left|\vec{F}_{i_{max}}\right| \qquad (4.8)$$

where $\left|\vec{F}_{i_{max}}\right|$ is the maximal (100% MVC) theoretical force developed by the corresponding muscle. We estimated plausible values of these forces by linear regression from the data provided by Smart et al. (2018) regarding the BB tendon stress Vs. elbow joint torque, as well as the cross-sectional areas of the insertion tendons of the BB, BR, and BA muscles provided by Giat et al. (1994). In this respect, we assumed the same mechanical properties for the tendons inserted at the elbow joint. The above yielded $\left|\vec{F}_{i_{max}}\right|$ values of 2060, 848, and 1507 N for the BB, BR, and BA muscles, respectively.

In this way, Eq. (4.6) was solved numerically as a function of the constraints of Eqs. (4.7) and (4.8), by using the function *fmincon* of the optimization toolbox of MATLAB (MathWorks Inc.). This function requires an initial approximate value of the individual forces for each torque level ($\vec{f_i}(\tau)$) to find the optimal solution. Thus, such forces were calculated using the $C_i(\tau)$ coefficients described in Chapter 3 as follows:

$$\vec{f_i}(\tau) = C_i(\tau).\overrightarrow{F_{m}}_{i_{max}} = \left(1 - \frac{\mu_L(0)}{\mu_L(\tau)}\right).\overrightarrow{F_{m}}_{i_{max}} \qquad (4.9)$$

Here, $\overrightarrow{F_{m}}_{i_{max}}$ is the maximal theoretical contractile force developed by the muscle belly, which was calculated as a function of the maximal theoretical stress of the skeletal muscle ($\sigma_{i_{max}}$) and the corresponding physiological cross-sectional area of the *i*-muscle belly ($PCSA_i$):

$$\left|\overrightarrow{F_{m}}_{i_{max}}\right| = PCSA_i.\sigma_{i_{max}} \qquad (4.10)$$

Concerning the value of $\sigma_{i_{max}}$, several studies has assigned values ranging from 220 to 360 kPa for mammalian muscles (Wells, 1965; Spector et al., 1980; Weijs and Hillen,

1985; Garner and Pandy, 2003). As in Garner and Pandy (2003), we assumed a $\sigma_{i_{max}}$ value of 330 kPa for the muscles of the upper limb.

In the text below, we will define the variables and parameters of the model as follows: $\vec{F}_i = |\vec{F}_i|$; $\vec{f}_i = |\vec{f}_i|$; $\overrightarrow{F_m}_{i_{max}} = \left|\overrightarrow{F_m}_{i_{max}}\right|$.

3.2 Data sources

The proposed model was applied to calculate the individual muscle forces of the BB, BA, and BR muscles during the isometric elbow flexion. In this regard, both τ and $C_i(\tau)$ values recorded in the thirteen subjects who performed the tasks of Chapter 3 were considered for this study. Concerning the values of $PCSA_i$, we estimated them from the corresponding echographic images obtained with SSI during the measurements performed at rest. In this regard, we considered the muscle as a cylinder whose diameter corresponds to the maximum muscle height obtained from such images. As the pennation angle of the BB, BR, and BA muscles is null or very low (0º, 2º, and 7.7º, respectively) during the contraction intensity range of the present study, we neglected their incidence for such a purpose (Lieber et al., 1992; Hodges et al., 2003). On the other hand, as the lever arms of the BB, BR, and BA muscles vary according to the elbow flexion angle (θ), these were estimated through (Marchese et al., 2001):

$$|\vec{r}_{BB}| = -2.9883.10^{-5}.\theta^3 + 1.8047.10^{-3}.\theta^2 + 4.5322.10^{-1}.\theta + 14.660 \quad (4.11)$$

$$|\vec{r}_{BR}| = -6.5171.10^{-5}.\theta^3 + 10.084.10^{-3}.\theta^2 + 1.6681.10^{-1}.\theta + 19.490 \quad (4.12)$$

$$|\vec{r}_{BA}| = -2.0530.10^{-5}.\theta^3 + 2.3425.10^{-3}.\theta^2 + 2.3080.10^{-1}.\theta + 5.5492 \quad (4.13)$$

The above equations express the lever arms and the elbow flexion angle in mm and degrees, respectively.

3.3 Statistical analysis

We calculated the mean values and standard deviations of the pre and post-optimized forces ($\vec{f_i}$ and $\vec{F_i}$, respectively) obtained for all subjects at six contraction intensity levels representative of the isometric elbow flexion ramps from which the elasticity of the BB, BR, and BA muscles was measured (5, 10, 15, 20, 20, 25 and 30% MVC). Besides, we conducted three two-sample t-tests for difference of means between the force values estimated by the model during the contraction range. Thus, in *t*-test 1, we perform intra-muscle comparisons of the $\vec{f_i}$ and $\vec{F_i}$ forces calculated between two consecutive levels. In t-test 2, we compare at the inter-muscular level both the $\vec{f_i}$ as well as the $\vec{F_i}$ values obtained at each of those levels. Finally, in *t*-test 3, intra-muscular comparisons of both forces were made for each of the contraction levels. The level of significance was set at $p < 0.05$.

4 – RESULTS

Figure 4.2 shows the results of the $\vec{f_i}$ forces as a function of joint torque for all subjects, calculated from the $C_i(\tau)$ and $\overrightarrow{F_m}_{i_{max}}$ values of the BB, BR, and BA muscles through Eq. (4.9). It also shows the net torque obtained from the balance between the internal torques generated by these forces, and the joint torque determined by the force applied on the dynamometer. As can be seen, between 0 - 30% MVC, the $\vec{f_i}(\tau)$ forces calculated for all subjects ranged from 0 – 177.44 ± 43.93 N (range of variation between 0 – 253.52 N), 0 – 52.94 ± 37.57 N (range of variation between 0 – 132.94 N), and 0 – 188.16 ± 76.58 N (range of variation between 0 – 288.44 N) for the BB, BR, and BA, respectively. Considering all subjects, the net torque ranged from ~ 10 to -30 N.m, varying between these values as the joint torque level increased between 0 and 30% MVC. In this sense, the internal torque determined by the $\vec{f_i}(\tau)$ forces was not enough to satisfy the equilibrium condition of Eq. (4.7) over the entire range of contraction intensity.

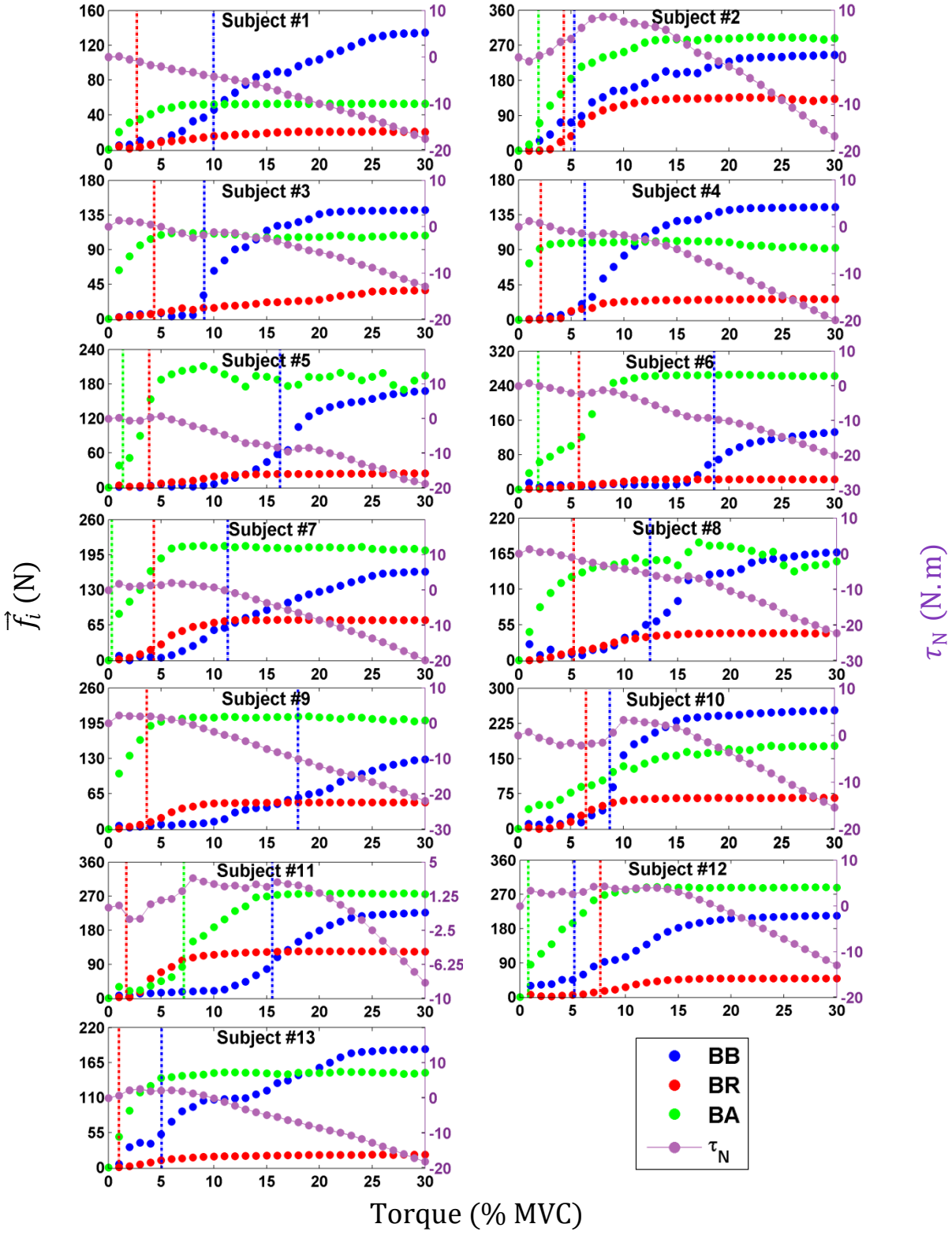

Figure 4.2. Initial approximates of force values calculated from eq. (37) in all subjects to optimize the estimation of individual muscle forces of the BB, BR, and BA muscles through the model. The net torque determined by the $\vec{f}_i$ and the external forces is also displayed, which is different from zero in all cases for each contraction intensity level. The vertical dashed lines indicate the C˜, calculated from Eq. (4.14) for each muscle with C+ behavior (same color code as $\vec{f}_i$).

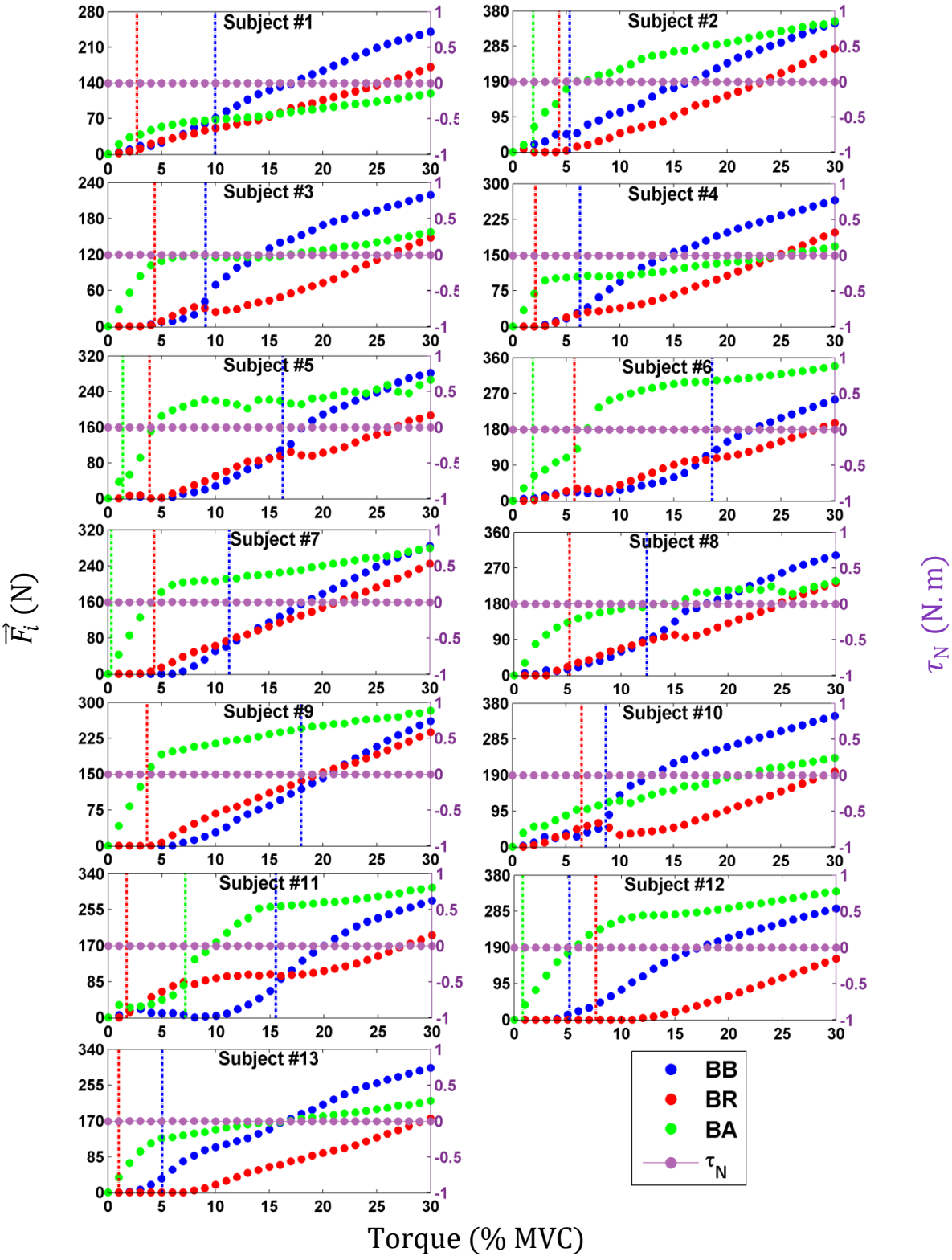

Figure 4.3. Individual muscular force values calculated by the model for the BB, BR, and BA muscles in all subjects. The net torque determined by the $\vec{F}_i$ and the external forces is zero in all cases for each contraction intensity level. The vertical dashed lines indicate the C˜, calculated from Eq. (4.14) for each muscle with C+ behavior (same color code as $\vec{F}_i$).

Table 4.1. Average values and standard deviations (between parentheses) of $\vec{f}_i$ and $\vec{F}_i$ forces obtained for BB, BR, and BA muscles of all subjects at six contraction intensity levels representative of the task.

	% MVC					
	5	10	15	20	25	30
$\vec{f}_{BB}$ (N)	21.24 (21.73)	65.94 (52.06)	109.12 (63.89)	149.62 (52.44)	170.26 (46.46)	177.44 (43.93)
$\vec{f}_{BR}$ (N)	18.91 (17.74)	44.29 (36.41)	50.98 (38.61)	52.14 (38.69)	53.01 (37.86)	52.94 (37.57)
$\vec{f}_{BA}$ (N)	130.86 (56.08)	176.15 (67.00)	186.56 (76.19)	190.59 (75.98)	188.05 (77.36)	188.16 (76.58)
$\vec{F}_{BB}$ (N)	17.22 (14.79)	66.48 (38.76)	128.25 (46.27)	191.20 (35.29)	241.43 (33.69)	282.03 (36.77)
$\vec{F}_{BR}$ (N)	16.73 (17.09)	46.02 (24.34)	78.19 (28.01)	111.28 (28.54)	154.23 (31.71)	201.71 (37.03)
$\vec{F}_{BA}$ (N)	127.96 (50.16)	176.49 (61.43)	198.58 (69.74)	216.70 (69.13)	232.75 (71.94)	253.86 (73.59)

Table 4.2. Results of *t*-test 1 showing intra-muscular comparisons of $\vec{f}_i$ and $\vec{F}_i$ values obtained from all subjects between two consecutive levels of contraction intensity along the isometric flexion ramps. $p < 0.05$.

	% MVC				
	5 vs. 10	10 vs. 15	15 vs. 20	20 vs. 25	25 vs. 30
$\vec{f}_{BB}$	0.00	0.00	0.04	0.15	0.34
$\vec{f}_{BR}$	0.02	0.33	0.47	0.48	0.50
$\vec{f}_{BA}$	0.04	0.36	0.45	0.47	0.50
$\vec{F}_{BB}$	0.00	0.00	0.00	0.00	0.00
$\vec{F}_{BR}$	0.00	0.00	0.00	0.00	0.00
$\vec{F}_{BA}$	0.02	0.20	0.26	0.28	0.23

Although such $\vec{f}_i(\tau)$ values are calculated to be used as inputs of the optimization algorithm, we will maintain them throughout the text since their biomechanical significance is addressed later in the discussion section.

As shown in Figure 4.3, using the $\vec{f}_i(\tau)$ values as initial approximations of the individual muscle forces yielded optimal solutions that determined null net torques for each contraction intensity level in all subjects. In this sense, the $\vec{F}_i(\tau)$ forces obtained by the model comprised values that ranged from 0 – 282.03 ± 36.67 N (range of variation

between 0 – 346.83 N), 0 – 201.73 ± 37.03 N (range of variation between 0 – 277.64 N), and 0 – 253.86 ± 73.59 N (range of variation between 0 – 352.39 N), for BB, BR, and BA, respectively. Table 4.1 shows the mean values of the $\vec{f}_i(\tau)$ and $\vec{F}_i(\tau)$, for six intermediate contraction intensity levels between 0 - 30% MVC.

Concerning the results of statistical analysis, Tables 4.2, 4.3, and 4.4 display the results of the *t*-test 1 to 3, respectively. In this sense, *t*-test 1 showed that although $\vec{f}_{\mathrm{BB}}$ and $\vec{f}_{\mathrm{BR}}$ do not change significantly from 20% and 10% MVC, respectively, the values of $\vec{F}_{\mathrm{BB}}$ and $\vec{F}_{\mathrm{BR}}$ show significant increases during the entire torque range. On the other hand, $\vec{f}_{\mathrm{BA}}$ and $\vec{F}_{\mathrm{BA}}$ behave similarly, as they only increase significantly up to 10% MVC. The inter-muscle comparisons of the force values performed in *t*-test 2 showed that the $\vec{f}_i$ and $\vec{F}_i$ values behave in a similar fashion. Thus, $\vec{f}_{\mathrm{BB}}$ and $\vec{F}_{\mathrm{BB}}$ differ significantly after ~10% MVC, $\vec{f}_{\mathrm{BR}}$, and $\vec{F}_{\mathrm{BR}}$ during the whole torque interval, while $\vec{f}_{\mathrm{BA}}$ and $\vec{F}_{\mathrm{BA}}$ do it from the beginning of contraction up to ~15% MVC. Finally, the cross intra-muscle comparisons carried out in *t*-test 3, revealed a significant change between the $\vec{f}_i$ and $\vec{F}_i$ forces after ~20, ~15, and ~25% MVC, for the BB, BR, and BA muscles, respectively.

Table 4.3. Results of *t*-test 2 showing inter-muscular comparisons of $\vec{f}_i$ and $\vec{F}_i$ values obtained from all subjects at six representative levels of contraction intensity along the isometric flexion ramps. $p < 0.05$.

	% MVC					
	5	10	15	20	25	30
$\vec{f}_{\mathrm{BB}}$ vs. $\vec{f}_{\mathrm{BR}}$	0.38	0.12	0.01	0.00	0.00	0.00
$\vec{f}_{\mathrm{BR}}$ vs. $\vec{f}_{\mathrm{BA}}$	0.00	0.00	0.00	0.00	0.00	0.00
$\vec{f}_{\mathrm{BA}}$ vs. $\vec{f}_{\mathrm{BB}}$	0.00	0.00	0.00	0.06	0.24	0.33
$\vec{F}_{\mathrm{BB}}$ vs. $\vec{F}_{\mathrm{BR}}$	0.47	0.06	0.00	0.00	0.00	0.00
$\vec{F}_{\mathrm{BR}}$ vs. $\vec{F}_{\mathrm{BA}}$	0.00	0.00	0.00	0.00	0.00	0.02
$\vec{F}_{\mathrm{BA}}$ vs. $\vec{F}_{\mathrm{BB}}$	0.00	0.00	0.00	0.13	0.35	0.12

Table 4.4. Results of *t*-test 3 showing intra-muscular comparisons of $\vec{f}_i$ and $\vec{F}_i$ values obtained from all subjects at six representative levels of contraction intensity along the isometric flexion ramps. $p < 0.05$.

	% MVC					
	5	10	15	20	25	30
$\vec{f}_{BB}$ vs. $\vec{F}_{BB}$	0.29	0.49	0.20	0.01	0.00	0.00
$\vec{f}_{BR}$ vs. $\vec{F}_{BR}$	0.38	0.44	0.03	0.00	0.00	0.00
$\vec{f}_{BA}$ vs. $\vec{F}_{BA}$	0.45	0.49	0.34	0.18	0.07	0.02

5 – DISCUSSION

Force development of elbow flexors during the isometric contraction

The present study aimed to develop a biomechanical model able to estimate the individual muscle forces of a synergistic muscle set during load sharing. This model is based on the formalism developed in Chapter 3. As we have seen, such formalism combines the acousto-elasticity theory, the short-range stiffness principle, and the ligand-binding dynamics of the actin-myosin cross-bridges. Thus, the resulting $C_i(\tau)$ coefficients describe the dynamics of the longitudinal shortening of each muscle, which is intrinsically associated with force generation during an isometric contraction (Grinspan et al., 2023)[1]. Such coefficients are the key element of the present model since they are considered for calculating the inputs of the static optimization algorithm through Eq. (4.9). i.e., the initial approximate values corresponding to the $\vec{f}_i$ forces.

As can be seen in Figure 4.2 and Tables 4.1 and 4.2, both the individual and mean values of $\vec{f}_i$ vs. joint torque denoted the same changes as those revealed by the shear elasticity in the measurements of Chapter 3 and the previous work of Bouillard et al. (2012b). Thus, for the lower contraction intensity levels that characterize the beginning of the isometric linear torque ramps (~ 0 - 10 % MVC), the torque is

[1]This paper details the results of Chapter 3.

produced mainly by the BA muscle which rapidly increases the exerted force from 0 to ~ 180 N on average. For its part, the BB and BR muscles have a lower contribution to total torque for this contraction intensity level, since their $\vec{f}_i$ values vary between ~ 0 - 70 and ~ 0 - 45 N, respectively (Figure 4.2 and Table 4.1). As is shown in Table 4.2, for 10% MVC, both the $\vec{f}_{BB}$, $\vec{f}_{BR}$, and $\vec{f}_{BA}$ are significantly higher than at lower torque levels. On the other hand, the results of the present Chapter also showed a change concerning the behavior of the $\vec{f}_i$ values from ~10% MVC. In this way, from this point until the end of the ramp, the $\vec{f}_{BB}$ showed a sustained increase from ~ 70 to 180 N, on average, being steeper between ~ 10 - 20% MVC. In contrast, the $\vec{f}_{BR}$ and $\vec{f}_{BA}$ did not show a significant increase from 10% MVC, remaining practically constant around values of ~ 50 and 185 N on average up to 30% MVC, respectively. Therefore, as shown in Bouillard et al. (2012b) and Grinspan et al. (2023) through shear elasticity and $C_i(\tau)$ estimates, the above also suggest a change in the relative contribution of each muscle to the total torque between ~ 10 - 30% MVC. However, this only reflects the change in load-sharing relative to the specific force generated by the longitudinal shortening of each muscle.

As we said previously, the static optimization algorithm of the present model uses both the joint torque and the $\vec{f}_i$ values as inputs. As a result, the model retrieved plausible individual muscle force $\vec{F}_i$ values expressed in N, which null the net torque across the elbow joint for all loading conditions as observed in Figure 4.3. Nevertheless, except for the BA, the $\vec{F}_i$ values of BB and BR muscles denoted some differences regarding their joint torque dependence compared to the $\vec{f}_i(\tau)$ curves (Figure 4.3, Tables 4.1 and 4.2). Particularly, while the $\vec{f}_{BB}$ values increased significantly from 0 to ~20% MVC, the $\vec{F}_{BB}$ exhibited a significant increase regarding lower torque levels during the

entire contraction intensity, varying between 0 to ~ 280 N on average. Concerning $\vec{F}_{\mathrm{BR}}$, it continuously increased significantly between 0 to 30% MVC ranging from 0 to ~200 N. thus differing from the $\vec{f}_{\mathrm{BR}}$ which remains stable from 10% MVC. In this way, the differences in the torque-dependence of the $\vec{f}_i$ and $\vec{F}_i$ values were steeper in the BR than in the BB muscle. This could be due to differences in the relative contribution of passive structures, and it may be related to the fact that the cross-sectional area of the BR tendon represents ~10% of the $PCSA_{BR}$, compared to BB where such ratio is ~5% (Giat et al., 1994). In addition, as we will discuss later, the causes of these gradual differences between each muscle-specific $\vec{f}_i(\tau)$ and $\vec{F}_i(\tau)$ forces during an isometric contraction ramp may also reside in other mechanisms independent of the cross-bridge binding (Ranatunga et al.. 2010).

Based on the above, the proposed model provided plausible individual muscle force values, which agreed qualitatively and quantitatively regarding the biomechanical and functional aspects of the BB, BR, and BA muscles during the isometric flexion of the elbow joint, as discussed in previous elastographic studies (Nordez et al., 2010; Bouillard et al., 2012b; Yoshitake et al., 2014; Lapole et al., 2015; Grinspan et al., 2021, 2023). Thus, for the BA muscle, the results denoted the ability of this muscle to generate the first torque effects at low contraction intensity levels, thus helping to develop precise movements and to guarantee joint stability. This is reasonable since it is a uniarticular muscle having approximately half of the lever arm of the BB at 90° of elbow flexion (Grinspan et al., 2023). Concerning the BB and BR, as also discussed in Chapter 3, the resulting forces reflect their capacity to additionally stabilize the shoulder and wrist joints by producing torques determined by comparable force levels to BA helped by their long-moment arm (Bouillard et al., 2012b). In this way, based on the force development vs. contraction intensity level results for the elbow flexor muscles,

the present model makes significant contributions to the previous efforts of characterizing individual muscle forces by shear wave elastography (Hug et al., 2015a; Ates et al., 2015; Bouillard et al., 2012a, 2012b; Grinspan et al., 2023).

Load sharing and the inflection point of $C_i(\tau)$

As discussed in Chapter 3, the ligand-binding behaviors determine the dynamics of longitudinal deformation of the BB, BR, and BA muscles during the isometric flexion of the elbow joint. The $C_i(\tau)$ coefficients of BB, BR, and in some cases the BA muscle, exhibit sigmoidal curves, which correspond to cooperative positive (C+) dynamics when they contract isometrically between 0 - 30% MVC (Grinspan et al., 2023). In this regard, the inflection points of such sigmoidal $C_i(\tau)$ curves can provide additional valuable information regarding the force production by the synergistic elbow flexor muscles. This inflection point can be calculated from the solution of the second derivative of the saturation fraction (Y) for cooperative receptors given by the Hill model (see Appendix 1C) (Wyman & Gill. 1990). As the Y of molecular receptors corresponds to the $C(\tau)$ coefficients in the skeletal muscle (see section 3.2 of Chapter 3), such an inflection point can be obtained through:

$$C^{\sim} = \sqrt[h]{\left(\frac{h-1}{h+1}\right) k_d} \qquad (4.14)$$

where both h (the slope of the Hill plot) and the dissociation constant k_d can be obtained from the Hill plot (Figure A.2 of Appendix 1C).

Based on the above, Table 4.5 provides the inflection points of the C+ curves of the $C_i(\tau)$ coefficients for BB, BR, and BA (when applicable) muscles in all subjects. Such data are also depicted in Figures 4.2 and 4.3. As observed, both for $\vec{f}_i(\tau)$ and $\overrightarrow{F_i}(\tau)$, the $C_{\widetilde{BB}}$ is often manifested as an intersection between the corresponding curves

of BB and BR. From this curve crossing, such curves follow the behavior described in the previous section concerning the results depicted in Tables 4.2 and 4.2. Thus, beyond $C_{BB}^{\sim}$, $\vec{f}_{\mathrm{BB}}(\tau)$ increases, reaching values higher than $\vec{f}_{\mathrm{BR}}(\tau)$ which remains stable. On the other hand, both $\vec{F}_{\mathrm{BB}}(\tau)$ and $\vec{F}_{\mathrm{BR}}(\tau)$ continue increasing, but the former reaches higher force values. Therefore, based on these results, the $C_{BB}^{\sim}$ seems corresponding to a breakpoint in the force distribution of the elbow flexors, especially between the BB and BR. The above is also depicted by the results of *t*-test 2 (Table 4.3), since $\vec{f}_{\mathrm{BB}}(\tau)$ vs. $\vec{f}_{\mathrm{BR}}(\tau)$ as well as $\vec{F}_{\mathrm{BB}}(\tau)$ vs. $\vec{F}_{\mathrm{BR}}(\tau)$ become significantly different from ~10% MVC, being the average value of $C_{BB}^{\sim}$ 10.90 ± 4.92% MVC (Table 4.5). In this regard, the proposed model retrieves the phenomenology described in previous works concerning the role of the ~ 10% MVC, as a key point in the load sharing between the elbow flexors muscles during their isometric contraction (Bouillard et al., 2012b; Grinspan et al., 2023).

Table 4.5. Inflection points calculated from the $C_i(\tau)$ curves of Chapter 2, for those muscles that exhibited C+ behavior.

# Subject	$C_{BB}^{\sim}$ (% MVC)	$C_{BR}^{\sim}$ (% MVC)	$C_{BA}^{\sim}$ (% MVC)
1	9.97	2.72	--
2	5.32	4.31	1.93
3	9.09	4.35	--
4	6.29	2.12	--
5	16.27	3.88	1.39
6	18.59	5.76	1.89
7	11.33	4.32	0.33
8	12.42	5.20	--
9	17.97	3.66	--
10	8.73	6.47	--
11	15.54	1.72	7.15
12	5.18	7.64	0.80
13	5.06	1.02	--
Mean	10.90	4.09	2.25
SD	4.92	1.90	2.48

As show in Figures 4.2 and 4.3, in several subjects (e.g. #7 and #9) $C\tilde{}_{BR}$ also seems to be a breakpoint, especially concerning the $\vec{f}_{\mathrm{BA}}(\tau)$, $\vec{F}_{\mathrm{BA}}(\tau)$, $\vec{f}_{\mathrm{BR}}(\tau)$, and $\vec{F}_{\mathrm{BR}}(\tau)$ curves. However, as such forces for BA are significantly higher than BR during the entire range of contraction intensity (Table 4.3), such an inflection point does not manifest as an intersection of curves. Thus, a different analysis is needed to discuss the significance of $C\tilde{}_{BR}$. In this regard, we perform an additional *t*-test (*t*-test 4) in order to assess the slope change of the $\vec{f}_i(\tau)$ and $\vec{F}_i(\tau)$ curves in the vicinity of such inflection point, specifically within the immediately pre and post-$C\tilde{}_{BR}$ intervals ([0, $C\tilde{}_{BR}$] and [$C\tilde{}_{BR}, 2C\tilde{}_{BR}$]% MVC, respectively) (Table 4.6). In addition to showing that the slopes of BA were steeper than those of BR and BB, this analysis revealed that the slope of both $\vec{f}_{\mathrm{BA}}$ and $\vec{F}_{\mathrm{BA}}$ curves between [0, $C\tilde{}_{BR}$]% MVC were significantly higher compared to the slope between [$C\tilde{}_{BR}, 2C\tilde{}_{BR}$]% MVC ($p$ = 0.00, both cases). On the other hand, the $\vec{f}_{\mathrm{BB}}$ and $\vec{F}_{\mathrm{BB}}$ did not show a significant slope change at the level of $C\tilde{}_{BR}$, as their pre and post-$C\tilde{}_{BR}$ slopes presented no significant differences (p = 0.18 and 0.10, respectively). Besides, as expected for the BR, the slopes of $\vec{f}_{\mathrm{BR}}$ and $\vec{F}_{\mathrm{BR}}$ changed at the level of $C\tilde{}_{BR}$, increasing slightly but significantly from [0, $C\tilde{}_{BR}$] to [$C\tilde{}_{BR}, 2C\tilde{}_{BR}$]% MVC ($p$ = 0.01 and 0.02, respectively). Therefore, in the context of load sharing, these results suggest that $C\tilde{}_{BR}$ is related to the force distribution between the BR and BA muscles at the beginning of the torque production (~ 0 -10% MVC). In this sense, the $C\tilde{}_{BR}$ seems to indicate the level of contraction intensity from which the torque contribution of BA begins to stabilize around a constant value, and that of the BR and BB increases thus supplementing the torque production between [$C\tilde{}_{BR}$, 30]% MVC. This is consistent with what was discussed in Chapter 3 and is also reflected in Tables 4.1 and 4.2. Finally, concerning the $C\tilde{}_{BA}$, we did not find any association of this point with load sharing, as it

appears at very low contraction intensity levels (~ 3% MVC on average, Table 4.5) and is not present in all subjects. As discussed in Chapter 3, this could be related to some bias in the estimation of $C_{BA}(\tau)$ within 0 - 10% MVC, as most of the increase in the pennation angle of the BA occurs within this range (Hodges et al., 2003).m

Table 4.6. Slope* change of the $\vec{f}_i(\tau)$ and $\vec{F}_i(\tau)$ curves immediately before (pre) and after (post) of $C_{\widetilde{BR}}$ (intervals ranging from [0, $C_{\widetilde{BR}}$] and [$C_{\widetilde{BR}}, 2C_{\widetilde{BR}}$]% MVC, respectively). The results of the corresponding *t*-tests 4 are also shown ($p < 0.05$).

	$\vec{f}_{\text{BB}}$		$\vec{F}_{\text{BB}}$		$\vec{f}_{\text{BR}}$		$\vec{F}_{\text{BR}}$		$\vec{f}_{\text{BA}}$		$\vec{F}_{\text{BA}}$	
# Subj.	pre-$C_{\widetilde{\text{BR}}}$	post-$C_{\widetilde{\text{BR}}}$	pre-$C_{\widetilde{\text{BR}}}$	post-$C_{\widetilde{\text{BR}}}$	pre-$C_{\widetilde{\text{BR}}}$	post-$C_{\widetilde{\text{BR}}}$	pre-$C_{\widetilde{\text{BR}}}$	post-$C_{\widetilde{\text{BR}}}$	pre-$C_{\widetilde{\text{BR}}}$	post-$C_{\widetilde{\text{BR}}}$	pre-$C_{\widetilde{\text{BR}}}$	post-$C_{\widetilde{\text{BR}}}$
1	3.16	-0.23	5.33	2.95	0.58	3.01	3.67	7.52	11.50	5.96	12.87	7.95
2	18.23	17.37	11.42	8.58	4.94	23.37	-0.78	7.01	38.97	27.08	34.69	21.56
2	1.66	-0.96	0.69	2.99	1.52	2.48	0.41	8.10	24.00	2.45	26.00	4.93
4	0.87	2.39	0.00	3.68	0.27	0.63	0.00	0.53	45.60	5.88	34.62	27.57
5	0.61	-0.15	0.39	3.23	0.29	2.54	0.68	6.60	35.82	15.72	35.77	17.84
6	0.50	0.97	3.92	2.20	1.62	2.18	5.57	3.93	18.56	26.39	20.71	27.17
7	1.06	3.91	0.02	1.87	4.75	12.10	1.23	10.98	37.38	15.51	40.03	15.02
8	0.18	3.51	2.96	7.77	2.74	3.58	4.19	9.64	25.60	4.66	27.34	7.34
9	1.10	0.74	0.00	1.95	3.32	8.48	0.00	11.67	44.25	4.45	41.21	11.70
10	2.64	36.29	5.63	28.73	4.20	6.63	7.86	-4.11	12.57	9.52	14.45	4.78
11	3.99	4.42	7.77	4.28	1.21	13.82	6.60	13.61	9.87	2.03	12.25	1.94
12	9.85	13.91	5.54	17.27	1.57	4.66	0.00	2.84	30.88	2.86	30.08	4.98
13	5.64	5.64	0.00	0.00	0.57	0.57	0.00	0.00	48.57	48.57	36.27	36.27
Mean	3.81	6.76	3.36	6.58	2.12	6.47	2.26	6.02	29.50	13.16	28.18	14.54
SD	4.90	10.02	3.50	7.68	1.62	6.31	2.82	4.95	12.99	13.14	9.84	10.39
p	0.18		0.10		0.01		0.02		0.00		0.00	

*The slopes are expressed in N/%MVC.

In summary, the previous results suggest that the inflection points of the cooperative positive $C_i(\tau)$ curves of the BB and BR indicate key points of force distribution between the synergistic elbow flexor muscles. As discussed, these results accounted for the behavior of the BB, BR, and BA muscles during load sharing described in previous elastographic studies (Nordez et al., 2010; Bouillard et al., 2012b; Yoshitake et al., 2014; Lapole et al., 2015; Grinspan et al., 2021). In this way, this work

provides a model able to estimate individual muscle forces, based on elastography measurements, the acousto-elasticity theory, and the ligand-binding approach. The results reinforce the evidence suggesting that the ligand-binding behaviors account for the dynamics of force production and the longitudinal shortening of muscle during the isometric contraction (Grinspan et al., 2023). Thus, in addition to estimating plausible values of individual muscle forces, the present study provides novel aspects related to the analysis of load sharing and their interpretation according to this framework.

The meaning of $\vec{F_i}$ and $\vec{f_i}$ in the context of muscle modeling

The study of mechanical muscle models is one of the major topics within the muscle biomechanics field. This approach is essential to understand how muscles generate the force, and how it can be estimated from direct or indirect measurements (Romero & Alonso, 2016). In this regard, Hill-type muscle models are commonly employed to describe the mechanism of force production (Hill, 1938). They are composed of different elements that describe the mechanical behavior of the tendon-muscle complex in terms of simple relationships (Romero & Alonso, 2016; Valour & Pousson, 2003; Arslan et al., 2019). In the most widely used version of this approach, the muscle is modeled by a contractile element arranged in parallel with an elastic or viscoelastic element, and both are disposed in series regarding an elastic element. In this context, as depicted in Figure 4.4, the results of the model proposed in this study suggest that the force produced by the contractile and the series elastic element, correspond to the $\vec{f_i}$ and $\vec{F_i}$ forces, respectively.

The contractile element of Hill-type muscle models typically represents the processes leading to muscle contraction occurring within the sarcomere. These processes are dependent on the formation of actin-myosin cross-bridges. During an

isometric contraction, the above determines a shortening in the muscle fibers' direction, thus generating the contractile muscular force. As several previous works have

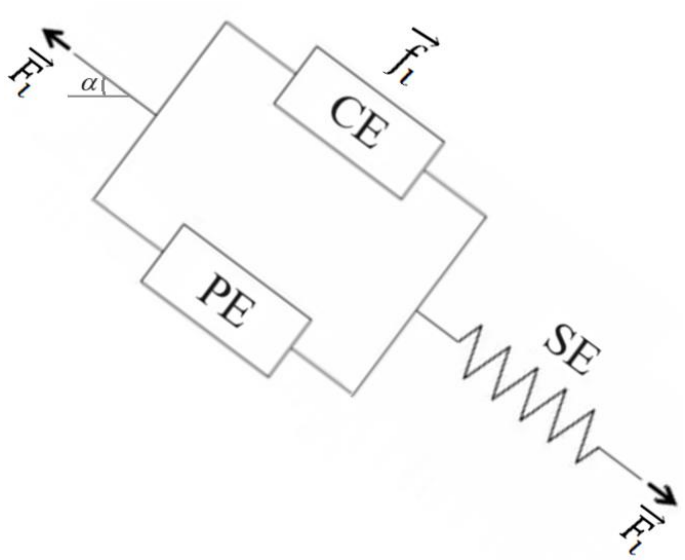

Figure 4.4. Classic three-element Hill-type muscle model. CE: contractile element; PE: parallel element; SE, series elastic element; α: muscle fibers' pennation angle.

pointed out, the ligand-binding dynamics exhibited by the $C_i(\tau)$ coefficients described in Chapter 3, are intimately associated with the reciprocal sliding of the contractile myofilaments during the active muscular force development (Shchepkin et al., 2017; Lehman, 2017; Reshetnyak et al., 2012; Rao et al., 2009; Zot et al., 2009; Tobacman & Butters, 2000; Lehrer & Geeves, 1998; Greene & Eisenberg, 1988; Lehrer & Morris, 1982; Greene & Eisenberg, 1980; Porter & Weber, 1979). According to the SRS property and the acousto-elasticy theory, the longitudinal shortening of the muscle ($\xi_L(\tau)$) is proportional to $C_i(\tau)$ (Eqs. (3.10 – 3.12)) (Grinspan et al., 2023). Likewise, as observed in Figure 3.8A, the averaged $C_i(\tau)$ coefficients of BB, BR, and BA muscles reached values close to ~ 0.8 before or at 20% MVC, which is also reflected concerning the significance of the differences between the corresponding $\vec{f}_i$ for such torque levels (Table 4.2). We will discuss later that this is consistent with the early and steeper tension change observed in skeletal muscle as a response to a ramped length change,

which is related to the characteristics of the cross-bridge cycle discussed in both pioneering and recent studies (Hill, 1949, 1951; Abbott & Ritchie, 1951; Ranatunga et al., 2010). Therefore, based on all the above, the $C_i(\tau)$ coefficients reflect the dynamics of the muscle contractile elements during the active force production. As the $\vec{f}_i$ forces are calculated directly from these coefficients (Eq. (37)), our results suggest that the $\vec{f}_i(\tau)$ values provide the force exerted by the contractile element of a Hill-type muscle model. This element is commonly modeled through the classic force-velocity relationship (Hill, 1938). In this sense, the above could lead to an alternative way of characterizing such a contractile element based on elastography measurements.

As seen in Figure 4.2, the contractile force $\vec{f}_i(\tau)$ of the BB, BR, and BA muscles alone is insufficient to null the net torque. This is because such values represent only the force contribution of the contractile elements, lacking the contribution of the passive elements, as occurs after applying the static optimization algorithm (Figure 4.3). Although, to the best of our knowledge, no previous study has been able to calculate the individual forces exerted by the elbow flexor muscles under the conditions of this study, some works under similar conditions allow performing an approximate comparison concerning the results obtained here. In this regard, the study of Smart et al. (2018) provides stress values developed by the distal BB tendon during the isometric elbow flexion at 2.5, 5, 10, 20, 40, 60, and 80% MVC. Thus, as such values vary linearly with the contraction intensity level with a determination coefficient of $R^2 > 0.99$, and the study provides the cross-sectional areas of the tendon, it is possible to calculate the exerted force and compare it to the $\vec{F}_{\mathrm{BB}}$ values obtained through the present model. In this regard, Table 4.7 depicts that both forces are of the same order, although the $\vec{F}_{\mathrm{BB}}$ values are lower than the respective forces derived from the data of Smart et al. (2018). The causes of such differences may arise from the flexion angle of the elbow joint, as in

the referred study it was 110º while in our protocol 90º. In this concern, it is well known that, both during dynamic and isometric contractions, altering the joint angle, and therefore muscle length, significantly impacts the force produced by the muscle (Zajac, 1989; Doheny et al., 2008). Several studies have accounted for the above based on electromyographic (EMG) activity and shear elastic modulus measurements, which correlate positively with each other and to the muscle force (Nordez et al., 2010; Yoshitake et al., 2014; Lapole et al., 2015; Grinspan et al., 2021, 2024). For example, according to previous works, both the BB as well as other muscles showed a significant increase in the voluntary force–EMG activity relationship concerning the joint angle (Heckathorne & Childress, 1981; Solomonow et al., 1986, 1991; Howard et al., 1986; Guimaraes et al., 1994). On the other hand, Zimmer et al. (2023) have reported a significant increase in the shear elasticity of the BB muscle at 25, 50, and 75% MVC, for elbow flexion angles of 120, 150, and 180º compared to 60º and 90º. In this way, all of the above may explain the differences observed in the force values of Table 4.7. In addition, it is important to note that both forces agree in their behavior with respect to the joint torque level, since both curves fit a straight line with an $R^2 > 0.99$. Therefore, based on all the above, the $\vec{F_i}(\tau)$ forces calculated through the proposed model are plausible individual force values of the BB, BR, and BA muscles during the isometric elbow flexion between 0-30% MVC. Thus, by assuming an arrangement of the elements of the Hill-type muscular model as considered above, our results suggest that such $\vec{F_i}(\tau)$ values correspond to the force exerted by the elastic element in series in each muscle.

Previous findings regarding the tension responses to ramp length changes in skeletal muscle, have described that the slope of the force developed by an active muscle shows an early change (P1 transition) followed by a later gradual change (P2 transition) (Ranatunga et al, 2010). The above provides a complementary framework for

comparing the $\vec{f}_i(\tau)$ and $\vec{F}_i(\tau)$ values obtained through our model. Concerning the P1 transition, using a strain-dependent mechano-kinetic model based on the scheme of Lymn and Taylor (1971) for the cross-bridge cycle, Ranatunga et al. (2010) showed that

Table 4.7. Comparison of the tendon force values of the BB muscle ($\vec{F}_{T_{BB}}$) derived from the data of Smart et al. (2018), regarding the $\vec{F}_{BB}$ values of Table 4.1. The standard deviation of the corresponding values is shown between parentheses.

	% MVC					
	5	10	15	20	25	30
$\vec{F}_{BB}$ (N)	17.22 (14.79)	66.48 (38.76)	128.25 (46.27)	191.20 (35.29)	241.43 (33.69)	282.03 (36.77)
$\vec{F}_{T_{BB}}$ (N)	93.33 (6.59)	192.50 (13.59)	288.37* (20.36)	388.89 (27.45)	482.88* (34.09)	580.14* (40.96)

*Calculated through the stress values obtained by linear regression of the corresponding data of Smart et al. (2018) for 2.5, 5, 10, 20, 40, 60, and 80% MVC.

such a transition reflects the tension change associated with the cross-bridge power stroke. Such a result was coincident with previous experimental findings on intact rat muscle fibers (Pinniger et al., 2006; Roots et al., 2007). In this matter, the steep slope of force described in the P1 transition agrees with the increase depicted by both $C_i(\tau)$ and $\vec{f}_i(\tau)$ for low torque levels (Figures 3.8A, 4.2 and Table 4.1). In addition to the direct dependence of $\vec{f}_i(\tau)$ on the $C_i(\tau)$ coefficients (Eq. 4.9), which reflect the contractile dynamics of the muscle, such correspondence with the contractile nature of the P1 transition provides further evidence in favor that $\vec{f}_i(\tau)$ accounts for the force contribution of the contractile elements of the muscle. On the other hand, Table 4.4 shows that, depending on the muscle, $\vec{F}_i(\tau)$ also corresponds to the contractile force below certain level of contraction intensity (15, 10, and 25% MVC, for the BB, BR, and BA, respectively), since it values does not have statistical difference regarding $\vec{f}_i(\tau)$. As a corollary to the above, this could have useful practical applications, for example, to estimate force production in muscles having a limited functional capacity (such as

during the early stages of rehabilitation), directly by measuring $\vec{f}_i(\tau)$ for low contraction intensities.

Concerning the P2 transition, the results derived of the cross-bridge cycle model of Ranatunga et al. (2010) were different to those of the experimental studies of Pinniger et al. (2006) and Roots et al. (2007). While in the model the tension reached a steady level and no further change in its distribution between the attached cross-bridges was observed, the experimental results showed a continuous increase in tension. As different works has shown, it appears that some non-cross-bridge visco-elastic elements in muscle stiffen upon activation and contribute to the continued tension rise (Edman and Tsuchiya, 1996; Mutungi & Ranatunga, 1996; Ranatunga, 2001; Bagni et al., 2002; Labeit et al., 2003). This continued tension change is a characteristic feature during lengthening and shortening in intact mammalian muscle and it provides a time-dependent feature to the muscle force production (Ranatunga et al., 2010). Similarly, the differences between $\vec{f}_i(\tau)$ and $\vec{F}_i(\tau)$ values along the flexion torque ramp, could also indicate the differential contribution of the contractile and elastic elements of each muscle as the contraction intensity increases. In this regard, our results in Figures 4.2 and 4.3 show that beyond a certain level of contraction intensity and up to the end of the ramp, the behavior of the $\vec{f}_i(\tau)$ and $\vec{\mathrm{F}}_\mathrm{i}(\tau)$ curves diverge since the former has a slight or null increase, being this steeper for $\vec{F}_i(\tau)$ curves. Thus, Table 4.4 shows significant differences between $\vec{f}_i(\tau)$ and $\vec{F}_i(\tau)$ values after 15, 10, and 25% MVC, for the BB, BR, and BA, respectively. In this regard, in light of all the above, our results suggest that such differences between the $\vec{f}_i(\tau)$ and $\vec{F}_i(\tau)$ forces after the referred torque values, correspond to the contribution of the elastic elements to force production in each muscle. In this way, this provides an additional support to the idea that the $\vec{F}_i(\tau)$ values provided by our model correspond to the force exerted by the linear elastic element.

With further work, in addition to individual muscle forces, this model could potentially characterize the contribution of its elements, in the context of a classic three-element Hill-type muscle model.

6 – CHAPTER CONCLUSIONS

This Chapter proposed an elastography-driven static-optimization model to address a long-standing problem in muscle biomechanics, as the estimation of individual muscle forces. The model is based on the framework developed in Chapter 3 by incorporating the $C_i(\tau)$ coefficients into the calculation of the $\vec{f_i}(\tau)$ forces. Thus, the acoustic-elasticity theory, the short-range stiffness, and the ligand-binding approach are considered within the model hypotheses that determine the calculation of their input values. In this way, the model provided plausible $\vec{F_i}(\tau)$ force values for the BB, BR, and BA muscles during the isometric elbow flexion. Such individual force values null the net torque on the elbow joint for each torque level, accounting for the behavior of each muscle according to its anatomical and functional features during the isometric elbow flexion. Likewise, the model also allowed the assessment of muscle load distribution as the level of contraction intensity increased. In this regard, the inflection points of $C_{BB}(\tau)$ and $C_{BR}(\tau)$ curves proved to be significant as a breakpoint in the synergistic action of elbow flexors muscles. On the other hand, the results of the model also suggested that the $\vec{f_i}(\tau)$ and $\vec{F_i}(\tau)$ forces correspond to the force contributions of the contractile and series elastic elements of a classic Hill-type muscle model, respectively. Thus, based on the above, the methodological and conceptual advances developed in this Chapter may have important future derivations in biomechanics and skeletal muscle modeling.

CHAPTER 5

TIME-DEPENDENCE OF LOAD-SHARING ASSESSED THROUGH SURFACE WAVE ELASTOGRAPHY

1 – INTRODUCTION

As seen in previous Chapters, elastography has become a widely accepted methodology to assess the longitudinal shear elastic modulus of skeletal muscle. Particularly, ultrasound shear wave elastography (SWE) methods, such as supersonic shear imaging (SSI), are the gold standard methods used for such a purpose. This has provided a novel way to measure the change in the mechanical properties of such tissue, thus driving a new approach in the studies on muscle biomechanics. The main advantages of the SWE methods are that they combine high-frequency ultrasonic waves (within the order of MHz) with low-frequency waves (100 ~ 1000 Hz), thus exhibiting high spatial resolution (< 1 mm) and good contrast in the characterization of shear elastic modulus (Grinspan et al., 2021, 2024). However, it is important to note that the imaging capabilities of SWE exceed the needs of certain areas of application related to muscle biomechanics (e.g. physiotherapy, sports training). In this sense, it is often sufficient to obtain an average value of the elasticity of the medium, rather than a map of its elastic field. This, in addition to the high cost of this technology, makes the cost-benefit ratio unfavorable, so qualitative methods are usually used to evaluate muscle elasticity (e.g. manual palpation or the assessment of joint range of motion (ROM)).

On the other hand, the proper application of SWE methods for biomechanical research needs some infrastructure, such as those found in a clinic or laboratory. Also, since its limited sample rate (~ 1-2 Hz), it is currently unfeasible to use SWE methods in conditions involving rapid contractions, whether isometric or during dynamic actions (e.g. running, walking, jumping). In this sense, the application of elastography in

biomechanical research is limited in terms of the experimental protocols that can be carried out, which must be performed within a clinic or laboratory. Other types of research are not possible, such as field applications, measurements under dynamic conditions, or evaluating the elastic properties in two or more muscles simultaneously. Such applications are impossible with current SWE methods as well as with other methods described in the literature (Dresner et al., 2001; Zhang and Greenleaf, 2007; Zhang et al., 2011a, 2011b, 2017; Zhang, 2016). In this regard, there is a current need to develop alternative and/or complementary elastographic methods to SWE, which can provide appropriate solutions to these issues and promote novel applications of elastography to assess skeletal muscle biomechanical properties.

In this context, as an alternative to the SWE, other elastography methods based exclusively on low-frequencies (~ 100 Hz) have recently emerged (Courage, 2003; Sabra et al., 2007; Benech et al., 2012; Salman et al., 2013; Martin et al., 2018; Benech et al., 2018; Grinspan et al., 2021). Thus, in the present Chapter, we will first review the essentials and the state of the art of low-frequency elastography. Then, we will focus on the Non-Ultrasound Surface Wave Elastography (NU-SWE), which is a method previously developed by our group at the Laboratory of Acoustical Ultrasound (LAU) of the Faculty of Sciences (University of the Republic (UdelaR), Uruguay) (Benech et al., 2019; Grinspan et al., 2021). We will emphasize the development of new features of the NU-SWE method, in order to overcome the previous limitations of elastographic methods for the biomechanical study of skeletal muscle. Thus, we will finally perform a proof of concept of the above, by using the updated version of the NU-SWE to characterize the synergistic action between the BB and BR muscles. Particularly, we will assess the dependence of the load-sharing between both muscles regarding the isometric elbow flexion velocity.

CHAPTER 5

2 – LOW-FREQUENCY ELASTOGRAPHY

2.1 State of the art

An alternative to SWE methods is the exclusive use of low frequencies (~ 100 Hz). By eliminating ultrasound frequencies, the spatial information is lost, so it is not possible to construct an elastic map of the medium. However, the information regarding the elasticity is preserved, so a numerical value about the mean elasticity of the tissue in a region of interest (ROI) can be obtained (*volume elasticity*). As mentioned above, this is more appropriate to the current needs of those fields related to muscle biomechanics, which currently use qualitative methods to determine skeletal muscle elasticity. In this sense, as we will see below, different works have proposed using laser vibrometry or contact sensors to record the propagation of surface waves (or Rayleigh waves), thus measuring their velocity and calculating the tissue elasticity.

The first work appearing in the scientific literature referring to using surface wave elastography in biomechanics is a paper by Kazarov and Klochkov (1989). Here, an ultrasound-based device is used to record the phase velocity of these vibrations, thus estimating both the shear elasticity and the viscosity of the soft tissues of the arm. Later, Popovic et al. (1992) and Courage (2003) described an elastographic method consisting of three flexural piezoelectric transducers from which it was possible to estimate the surface wave velocity. According to the authors, such a velocity is directly related to the elasticity of the tissue in contact with the sensors, thus reporting results in both skin and frog sartorius muscle *in vitro*. Another related work refers to a "passive" elastographic technique, which does not use external perturbations to induce surface waves on the muscle (Sabra et al., 2007). Instead, this method uses muscle noises produced during muscle contraction. Thus, using skin-mounted accelerometers, the authors estimated the elasticity of the vastus lateralis muscle during knee extension. On the other hand,

Salman and Sabra (2013) developed a technique to measure surface wave velocity using laser vibrometry. This technique enabled them to estimate elasticity in skeletal muscle and soft tissue-mimicking phantoms.

Most of the methods cited previously assume a Rayleigh wave model for the surface waves (Royston et al., 2011). Here, the Rayleigh wave velocity (V_R) has a simple relation to the shear wave velocity ($V_R \cong 0.96V_s$)), and thus to the shear elastic modulus. However, since typical values of shear wave velocity in muscles at rest range between 2-4 m/s, if the excitation frequency is ~100 Hz, the shear wavelength is between 2- 4 cm. This value is of the same order of the muscle depth. Therefore, the muscle cannot be assumed as a semi-infinite but a bounded one, so guided wave propagation takes place (Rayleigh, 1888; Lamb, 1917; Benech et al., 2015). On the other hand, near-field effects can also be present. These effects are caused by constructive and destructive interference from different types of waves when the source is relatively close to the sensors. In this regard, as the wavefield is usually measured close to the source, such effects can also introduce biases into the measurements (Benech et al., 2017; Grinspan et al., 2021). Thus, a model that considers both effects associated with the exclusive propagation of low frequencies is needed to obtain unbiased values of the shear elasticity of skeletal muscle.

In this context, we have previously developed and patented[2] the NU-SWE[3] method, by designing new algorithms that correct the incidence of guided wave propagation and near-field effects on the elasticity estimates (Benech et al., 2017, 2019).

[2]Invention patents:
-Benech, N., Grinspan, G.A., Aguiar, S., Negreira, C.A. "Device and method for determining the elasticity of soft-solids." PCT (Brasil). Grant: 18/07/2023; Registration No: BR2018/050395.
-Benech, N., Grinspan, G.A., Aguiar, S., Negreira, C.A. "Device and method for determining the elasticity of soft-solids." United States. Grant: 24/01/2023; Registration No: US 11,561,201 B2.
- Benech, N., Grinspan, G.A., Aguiar, S., Negreira, C.A. “Método para determinar la elasticidad de sólidos blandos.” Argentina. Grant: 30/04/2024; Registration No: AR113330B1.
-Benech, N., Grinspan, G.A., Aguiar, S., Negreira, C.A. "Device and method for determining the elasticity of soft-solids." Australia. Grant: 26/07/2024; Registration No: AU 2018359026 B2.
[3]This name differentiates the method from ultrasonic shear wave elastography, also known as SWE (Shear Wave Elastography).

This method has the advantages of being small, portable, low-cost, and easy to manipulate. Their first application in skeletal muscle was made by Grinspan et al., 2019, 2021), who assessed the relationship between the change in muscle elasticity, joint torque, and the EMG activity level. This work showed comparable results to those obtained with SWE, thus showing the potential utility of the NU-SWE for biomechanical research. Below, we will detail the main features of the NU-SWE method. Then, we will account for the last enhancements developed in this thesis, from which emerge the results of the present Chapter.

2.2 Non-Ultrasound Surface Wave Elastography

2.2.1 Theoretical basis of NU-SWE and estimation of muscle elasticity

The NU-SWE method consists of exciting low-amplitude, low-frequency (~100 Hz) surface wave propagation on the free surface of the muscle, recording its displacement using the linear array of vibration sensors, and estimating its phase velocity. The shear wave velocity is calculated from the surface wave velocity using inversion algorithms. Thus, the method estimates the shear elasticity of the muscle by calculating the shear wave velocity in a linear regime.

Figure 5.1C displays an example of the received signals in the four sensors for a single emitted pulse. The distance between sensors is d = 8.0 mm (Figure 5.1A). A time delay is clearly observed between sensors, indicating a propagating wave. Figure 5.1D shows the power spectrum of the received signal. The center frequency is around 100 Hz as expected and its -6dB bandwidth (red dotted line in the figure) spans from 80 to 115 Hz. To estimate the shear wave velocity ($V_s^{\parallel}$) we compute the phase velocity V_ϕ of the surface wave for each frequency within the bandwidth. Due to interference between different surface waves, V_ϕ is a function of frequency (Benech et al., 2017, 2019). For instance, this curve can be modeled as the interference of the Rayleigh wave and the

leaky surface wave which arises from the complex roots of the Rayleigh secular equation (Schröder & Scott, 2001; Benech et al., 2022). This last wave is a near-field wave with exponential decay. Its characteristic propagation distance is of the order of one shear wavelength. Figure 5.1E displays the fit of the experimental values of V_ϕ with the theoretical model given in (Benech et al., 2019). Briefly, the phase velocity is computed as:

$$V_\phi = \omega \left(\frac{\partial \phi}{\partial x}\right)^{-1} \qquad (5.1)$$

where $\phi$is the phase of the signal and x is the horizontal distance.

Equation (5.1) is used to compute the phase velocity for each frequency ω within the bandwidth of the signal so a dispersion curve $V_\phi(\omega)$ is obtained. For a low-frequency excitation, most of the energy of bulk waves propagates as shear waves. Due to the large difference between the velocities of compressional and shear waves, there is no mode conversion in boundary reflection. Thus, the shear waves reflect back as a shear wave. Besides, for normal excitation, there is a directivity pattern for shear waves at an angle θ with respect to the normal (Fig. 5.1F) (Miller & Pursey, 1954; Benech et al., 2019). Therefore, if the thickness of the muscle is h, there exists a distance x_c where only surface waves propagate given by:

$$x_c = 2h \tan(\theta) \qquad (5.2)$$

As shown in Benech et al., (2017), if the wavefield is measured at a distance $x \gg x_c$ from the source, the dispersion curve $V(\omega)$ fits the model of Rayleigh-Lamb. However, if $x \leq x_c$, the dispersion curve is due to interference between the Rayleigh and the leaky surface wave. For transversely isotropic solids, the directivity angle is $\theta \approx 60º$. The mean thickness h of each muscle is 3.5 cm for the BB and 2 cm for the

BR (Grinspan et al., 2023). Therefore, $x_c \approx 12$ and 7 cm respectively. Thus, within our simplified model, the vertical component $u_z(x,t)$ of surface wavefield for $x < x_c$ of a monochromatic wave is given by:

$$u_z(x,t) = A_R[e^{-ikx} + A_L e^{-\xi x} e^{-iqx}]e^{i\omega t} \qquad (5.3)$$

where k is the Rayleigh wavenumber, A_R is the amplitude of the Rayleigh wave, A_L is the relative amplitude of the leaky wave with respect to the Rayleigh wave and ξ, q are the imaginary and real part of the leaky wavenumber (k^L), respectively. The later can be calculated as follows (Benech et al., 2017):

$$k^L = \frac{\omega}{V_R} = \frac{\omega}{q + i\xi} \qquad (5.4)$$

On the other hand, the phase ϕ of the field of Eq. (5.3) is given by:

$$\phi(x) = \tan^{-1}\left(\frac{N(x)}{D(x)}\right) \qquad (5.5)$$

where

$$N(x) = -[sin(kx) + A_L e^{-\xi x}\, sin(qx)] \qquad (5.6)$$

$$D(x) = cos(kx) + A_L e^{-\xi x}\, cos(qx) \qquad (5.7)$$

Therefore, the phase velocity is given by:

$$V_\phi = \omega\left(\frac{N'D - ND'}{D^2 + N^2}\right)^{-1} \qquad (5.8)$$

where the prime indicates derivative with respect to x. The above equation allows calculating the phase velocity of a homogeneous, isotropic, and elastic solid. Similar calculations can be made to obtain such a value for a transversely isotropic solid, like the skeletal muscle, as described in Benech et al. (2019). Figure 5.1E displays the

experimental values of V_ϕ and the fit with Eq. (5.8). The output value in this example is $V_s^{\parallel} = 2.26\, m/s$.

As mentioned in previous works, if we consider the muscle like a transversely isotropic solid (Gennisson et al., 2005; Nordez et al., 2010), the longitudinal shear elastic modulus (μ_L) is related to a shear wave propagating in the muscle fibers direction with perpendicular polarization $V_s^{\parallel} = \sqrt{\mu_L/\rho}$ (where ρ is the muscle mass density = 1000 Kg/m^3) (Benech et al., 2019). Due to the arrangement of the wave source and the linear array of vibration sensors (Fig. 5.1A), the NU-SWE retrieves $V_s^{\parallel}$. Thus, in an analogous way to previous works using ultrasound elastography (Gennisson et al., 2005, 2010; Nordez et al., 2009; Nordez & Hug, 2010; Bouillard et al., 2011, 2012a, 2012b; Ateş et al., 2015; Yoshitake et al., 2014; Lapole et al., 2015), we can estimate the muscle shear elasticity through Ec. (3.16):

$$\mu_L = \rho V_s^{\parallel 2} \qquad (3.16)$$

As we have seen previously, this equation assumes that the viscous effects of the tissue are negligible. So, the NU-SWE, as classic elastography studies using echographic and magnetic resonance imaging, assumes that the mechanical behavior of muscle is like that of a linear elastic material (Gennisson et al., 2003, 2005; Heers et al., 2003; Jenkyn et al., 2003; Bercoff et al., 2004a; Uffmann et al., 2004; Catheline et al., 2004; Nordez et al., 2008, 2010; Tanter et al., 2008; Deffieux et al., 2009; Ateş et al., 2015).

2.2.2 Experimental setup of the NU-SWE: first implementation

The NU-SWE device is composed of a linear array of contact vibration sensors, an external wave source, an audio amplifier, an analog-to-digital (A/D) converter board (NI-USB 6009, National Instruments), and a computer. In this case, the external wave source, a shaker with a coupled piston, was driven by ten cycles of a sinusoid with a central

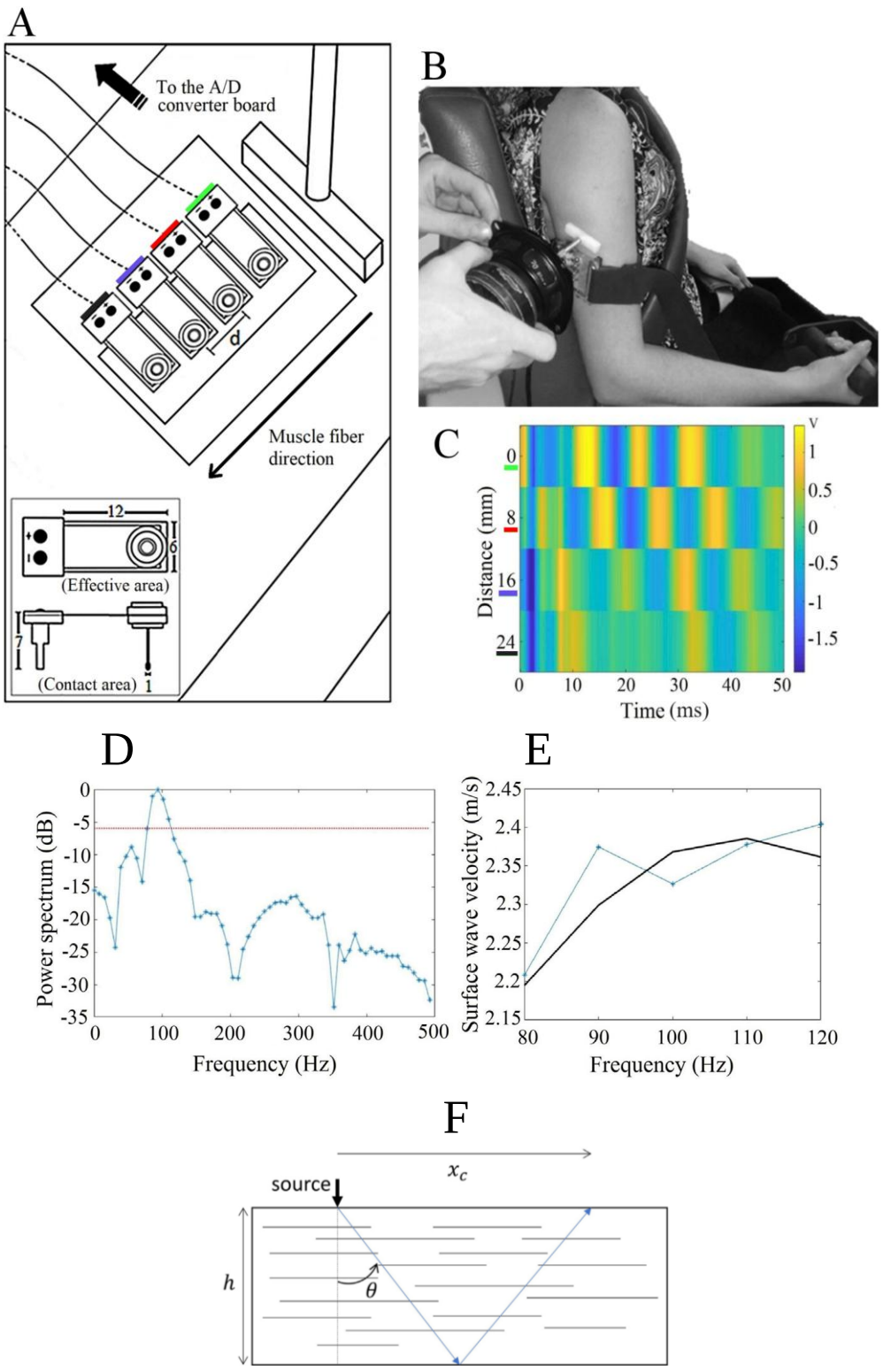

Figure 5.1. A: scheme showing the relative arrangement of the wave source, the underlying muscle fibers direction, and the linear array of vibration sensors (dimensions in mm). B: an example of the NU-SWE prototype placed over the free surface of the triceps brachii muscle. C: Example of the signals received by the corresponding sensors on the linear array for a single pulse emitted (indicated by colors). D: Power spectrum of the received signal. E: Estimation of $V_s^{\parallel}$ from the experimental values of V_ϕ (blue line) and their corresponding fit (black line) based on the model detailed in Benech et al. (2017). F: Directivity pattern of the shear waves for a normal excitation. Adapted from Grinspan et al. (2021, 2024).

frequency varying between 50 and 250 Hz. It vibrates normally to the free surface of the muscle to excite mainly the vertical component of surface waves (Figure 5.1B). This component of the vibrations is recorded by the linear array of sensors, each constituted by a piezoelectric PVDF flexible film. Besides, they possess a mass on the end with a small extension attached to it (Figure 5.1A). Such an extension changes the sensors' inertia to adapt their resonance frequency to that emitted by the wave source. In this way, the NU-SWE uses point-like sensors (contact area ~ 1 mm^2), thus avoiding diffraction effects at the reception (Benech et al., 2012; Grinspan et al., 2016). Furthermore, as is shown in Figure 5.1A, the source is aligned with the array of sensors, which must be equally spaced a distance *d* from each other. According to this, the sensors are arranged on a plate that holds them in the correct configuration and positioned on the arm by a holding brace (Figures 5.1A and 5.1B). Thus, the vibration is captured sequentially by the sensors, producing a signal that is digitized by the A/D converter board and transferred to a computer for processing. As we will see later, some aspects of the referred experimental setup have been improved in the present thesis, to measure in more than one muscle simultaneously and at a higher sampling rate.

3 – COMPARISON OF NU-SWE WITH SSI AND ITS APPLICATION TO STUDYING THE TEMPORAL DEPENDENCE OF MUSCLE SYNERGISM

Both SWE devices and low-frequency elastography methods developed so far cannot measure several muscles simultaneously and have a sampling frequency between 1 and 2 Hz. This limits the biomechanical applications of elastography and determines that the experimental protocols must consider slow and controlled long-time tasks (for example, 20-30 s) to obtain enough data and perform a proper analysis. Thus, for example, it is currently not possible to assess the load-sharing from muscle elasticity estimates for different contraction rates, as is possible for other related variables such as

the electromyographic (EMG) activity. In this regard, some features of low-frequency methods can be used to improve the measurement capabilities of muscle shear elastic modulus and overcome the aforementioned limitations. Particularly, surface wave methods do not need to retrieve the low-frequency field from speckle tracking algorithms, on which SWE methods are based for calculating the displacements (Dickinson & Hill, 1982; Catheline, 1998). On the other hand, they don't measure bulk wave propagation but only the field at the surface of the muscle. Thus, it is possible to increase the sampling rate by sending several short pulses and storing the field for post-processing.

In this way, in this Section we present an updated version of the NU-SWE, which comprises a free-hand device that can measure the shear elasticity without applying pressure on the medium (as with the US probe), in more than one muscle simultaneously and at a higher sampling rate. First, we conducted a direct comparison of the elasticity estimates provided by the NU-SWE and the SSI (*experiment 1* and *2*). Then, we applied the new features of the NU-SWE to characterize the change of the shear elasticity of the biceps brachii (BB) and brachioradialis (BR) muscles during the execution of isometric flexions of the elbow joint at different contraction velocities (*experiment 3*). In this second experiment, we also measured the EMG activity of both muscles during such tasks. This allowed us to account for the temporal dependence regarding the relationship between the elastic and electric behavior of these muscles during their synergistic action, which are emergent properties derived from the new measurement capabilities of the updated NU-SWE method.

3.1 Materials and methods

3.1.1 Subjects

The three experiments comprising the present study involved healthy subjects. First, 28 volunteers participated in *experiment 1* (20 men, 8 women, age 34.25 ± 6.92 yr, height 173.62 ± 9.38 cm, weight 79.05 ± 17.14 Kg). On the other hand, *experiment 2* was carried out with 10 participants (9 men, 1 women, age 35.38 ± 7.17 yr, height 173 ± 7.39 cm, weight 72 ± 14.55 Kg) Finally, seven male volunteers participated in *experiment 3* (age 25.70 ± 3.20 yr, height 177.90 ± 6.28 cm, weight 85.0 ± 11.72 kg). In all cases, volunteers were informed about the methods, procedures, and purpose of the study. All participants provided their written informed consent. The experimental design of the study was conducted according to the last version of the Helsinki statement and approved by the Ethical Committee of the Faculty of Medicine and Clinics Hospital (UdelaR, Uruguay, File No. 071140-001398-11 and File No. 08-20, respectively).

3.1.2 Instrumentation

Shear wave elastography

In *experiments 1* and *2,* an Aixplorer ultrasonic scanner (Supersonic Imagine, Aix en Provence, France) with a linear transducer array (2–10 MHz, SuperLinear 10-2, Vermon, Tours, France) was used in SSI mode to obtain the shear elasticity map of the RF and BF muscles. The basis of this method was already presented in Chapter 3.

Non-ultrasound surface wave elastography

An updated version of the NU-SWE was employed to assess the shear elastic modulus at a high sampling rate (*experiments 1* and *2*) and in more than one muscle simultaneously (*experiment 3*). Compared to the experimental setup detailed in Section

2.2.2, in such a version the sensor signals are amplified, thus allowing a small shaker with a coupled piston to be used as an external wave source (Figure 5.2A). This is attached to the surface of the medium through adhesive patches (Figures 5.5C, 5.5D, and 5.6B), thus avoiding its manipulation during measurements as in the previous NU-SWE device (Figure 5.1B).

In order to be able to measure the elasticity changes in muscles at a higher sampling rate, we used the excitation scheme displayed in Figure 5.2B. A 4-cycle sinusoidal pulse is emitted, which is modulated with a Gaussian function to minimize the transient behavior of the source at the start and the end of the signal (Benech et al., 2019). The time duration of this signal t_s is 40 ms. Then, a rest time t_d is introduced before sending the next pulse with the same characteristics as the previous one. This rest time is introduced to avoid interference between the direct and reflected waves. In this way, the time between two consecutive measurements is $\Delta t = t_s + t_d$, and therefore, the elasticity sampling frequency is $f_e = 1/\Delta t$. This procedure is repeated until the total time T of the experiment is reached. The inversion algorithm described in Section 2.2.1

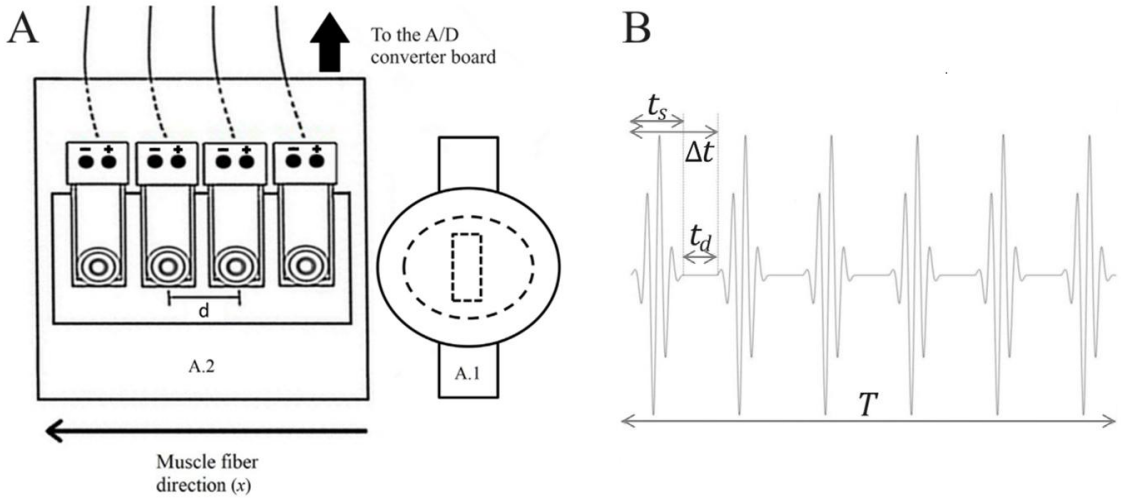

Figure 5.2. A: Scheme showing the configuration of the updated version of the NU-SWE (A.1: reduced-size wave source; A.2: relative arrangement of the linear array of vibration sensors; *x*: muscle fibers' direction; d = 8.0 mm). B: Signal used to excite the source for surface wave generation. The sinusoidal pulse is repeated n times with a time separation t_d between them. The elastic sampling frequency is $f_e = 1/\Delta t$. Adapted from Grinspan et al. (2024).

is applied to each pulse, allowing the shear wave velocity to be calculated at the corresponding f_e. A trade-off exists between the sampling frequency and the accuracy of the shear wave speed estimation. If t_d is decreased, the sampling frequency increases but the signal contains direct and reflected waves, introducing a bias in the estimation of the phase speed. On the other hand, if t_d is increased, the reflection bias is avoided but the sampling frequency may be too low to follow the changes occurring during short-duration tasks. In this work, we found empirically by trial and error, that a 15 Hz sampling frequency (i.e., $t_d \cong 27$ ms) is a compromise value that allow us to follow the elasticity changes with little bias in the phase speed estimation.

The central frequency of the sinusoidal train pulses differed among experiments due to the particularities of each task (see Protocols). Thus, since *experiments 1* and *2* were performed in static conditions, the train pulses comprised a frequency sweep between 100-350 Hz (Figures 5.3 and 5.4). On the other hand, as the muscle elasticity varied as a function of time and the contraction intensity level in *experiment 3*, the central frequency of the sinusoidal pulses emitted was 100 Hz, in agreement with our previous work performed in such conditions (Grinspan et al., 2021).

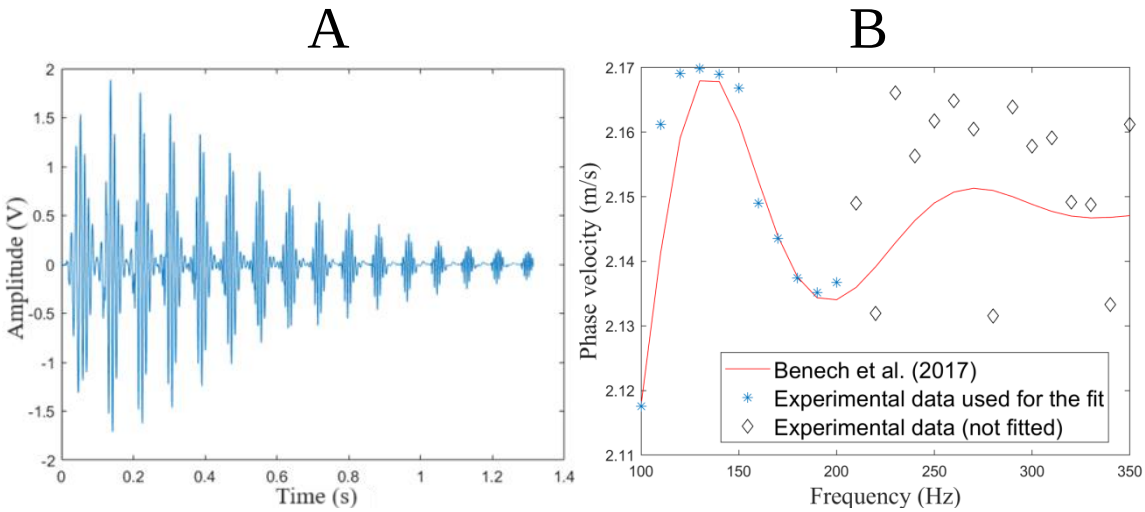

Figure 5.3. Example of the sinusoidal pulses of the frequency sweep (A) and the corresponding phase velocities (B) for the resting measurements performed in *experiments 1* and *2*. Due to the attenuation of the signals for frequencies above 200 Hz, the shear velocity was obtained by fitting the model of Benech et al. (2017) to the data between 100-200 Hz.

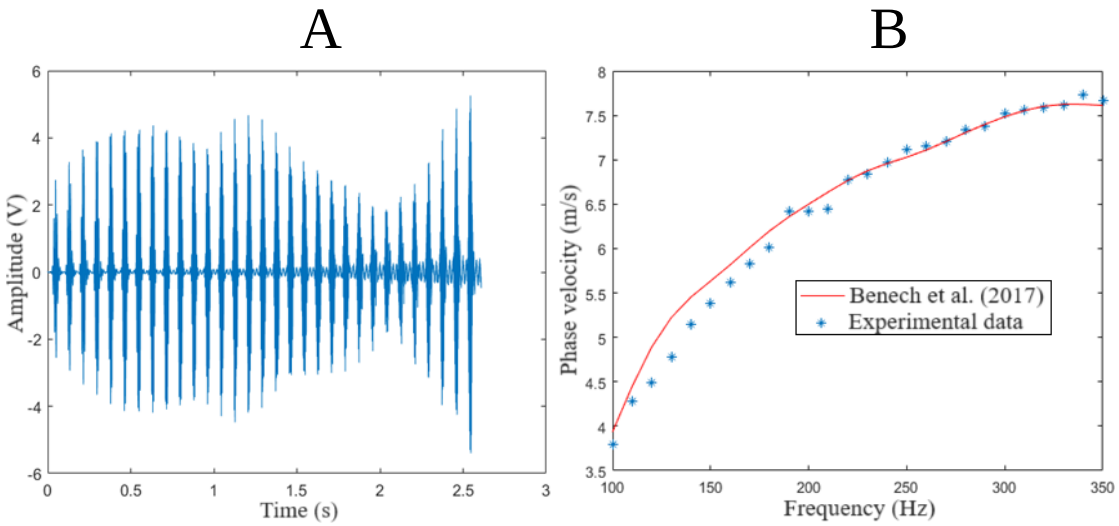

Figure 5.4. Example of the sinusoidal pulses of the frequency sweep (A) and the corresponding phase velocities (B) for the measurements on a stretching condition performed in *experiment 2*. Since the amplitude of the signals is not attenuated with frequency, the shear wave velocity was obtained by fitting the model of Benech et al. (2017) within the entire frequency range.

Ergometry

A research isokinetic dynamometer (Biodex System 4; Biodex Medical, Shirley, NY) was used to measure the angle and torque production of the elbow joint in *experiment 3*. During the data collection, the volunteers were positioned with their right shoulder and elbow flexed at 90º and the forearm supinated. The elbow joint was aligned coaxially with the axis of the dynamometer (Figure 5.7).

Electrode placement, EMG recordings and signal processing

In *experiment 3*, adhesive arrays of sixteen, silver-bar electrodes (8 mm inter-electrode distance; Spes Medica, Battipaglia, Italy) were used to acquire surface EMGs from BB. Likewise, adhesive arrays of eight, silver-bar electrodes (0.5 mm inter-electrode distance) were used for the BR. Firstly, for the BB, the proximal and distal muscle boundaries were identified using ultrasound equipment (2-10 MHz linear transducer; v.11 Supersonic Image, Aix-en-Provence, France). The eighth electrode of the 16 array was positioned at 50% of the length of the BB (Figure 5.7C). For the BR,

the superior and inferior boundaries were identified using the same ultrasound equipment. The fourth electrode of the 8 array was positioned at 50% of the muscle length (Figure 5.7C).

The electrode-skin contact was ensured with conductive paste (AC cream, Spes Medica, Genova, Italy) and the reference electrode was positioned in the olecranon and radium styloid process. Data was collected in monopolar derivation and sampled at 2048 samples/s using a 12-bit A/D converter, with 5V dynamic range. Furthermore, EMGs were amplified by a 2.000-10.000 variable factor using a 10-900 Hz bandwidth amplifier (CMRR > 100 dB; EMG-USB2, OT Bioelettronica, Turin, Italy).

All monopolar EMGs were filtered with a 4^{nd} order, bandpass filter (Butterworth, 15–350 Hz cut-off frequencies). After that, the root mean square (RMS) value, with 250 ms window size, was computed separately for each pair of electrodes, resulting in 15 differential channels for BB and 7 for BR.

3.1.3 Protocols

Experiment 1

Each volunteer was asked to lie down (face up and down) on a stretcher. The elasticity of the RF and BF of both legs at rest were measured with SSI using the Aixplorer ultrasound scanner and with the NU-SWE device (Figure 5.5). Three series of measurements were performed independently with each method, by placing the ultrasonic scanner probe and the linear array of vibration sensors on the corresponding muscle belly at 50% of the thigh distally from the greater trochanter.

Experiment 2

Volunteers were instructed to lie face-up on a stretcher. The placement of the linear array of vibration sensors and the ultrasound scanner probe was performed

according to the same specifications as in *experiment 1*. Thus, in the first place, three series of measurements on the resting RF muscle were performed independently with SSI Aixplorer and NU-SWE. Then, volunteers were instructed to lie facing up with the thigh aligned regarding the torso and forming a 110° angle with the leg at the knee (Figure 5.6). This way, three series of measurements on the stretched RF muscle were performed with each method, with an interval of 120 s between them.

Experiment 3

Initially, the volunteers performed two maximal isometric voluntary elbow flexions (each lasting 5 s and resting 120 s between them) with the shoulder and elbow flexed at 90º to determine the maximal voluntary contraction (MVC) torque. The highest torque value was used to normalize submaximal contractions. Both for the EMG and the NU-SWE measurements, volunteers were asked to perform eight linear torque ramps (120 s rest between tasks) of isometric elbow flexion from 0-40% of MVC over 5, 10, 15, and 20 s (twice each). In this way, depending on the task, the %MVC increased at a rate of 8, 4, 2.67, and 2 %MVC/s, respectively. Since there was not enough space for the NU-SWE device after placing the EMG electrode arrays on the surface of BB and BR muscles, the NU-SWE and the EMG measurements were performed in separate trials. This also avoided the possible contamination of the EMG signals by the surface vibration artifacts. In order to correctly execute the torque ramps, they had to follow the path indicated on a monitor put in front of them. The $V_s^{\parallel}$ of BB and BR muscles was measured simultaneously at 15 Hz during the execution of the tasks in separate trials and in random order. Likewise, the EMG activity of both muscles was also measured in the same way. During measurements, the NU-SWE devices and the EMG electrodes remained fixed on the muscle belly and carefully aligned with respect to the orientation of the muscle fibers. They were placed on the muscle belly, at

70% of the arm's length distally from the acromion for the BB and 35% of the forearm length distally from the elbow for the BR (Figure 5.7A and 5.7B). The locations of the devices were marked using a waterproof pen to guarantee their repeatability between trials.

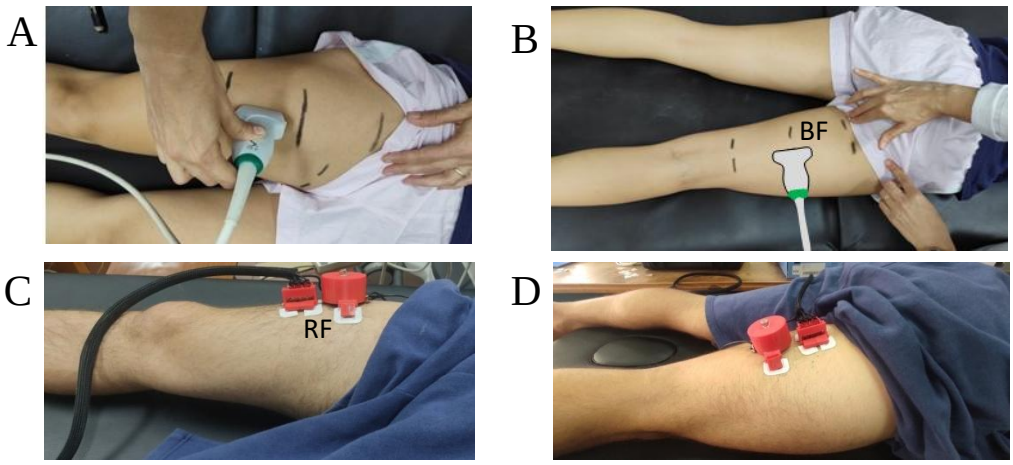

Figure 5.5. Examples of the experimental setup for the resting measurements of *experiments 1* and *2*. The placement of the SSI Aixplorer ultrasonic scanner probe (A, B) and the NU-SWE device (C, D) on the free surface of the RF and BF muscles are shown, respectively.

Figure 5.6. Examples of the experimental setup for the stretch measurements in Experiment 2. The placements of the SSI Aixplorer probe (A) and the NU-SWE device (B) on the free surface of the RF muscle are shown.

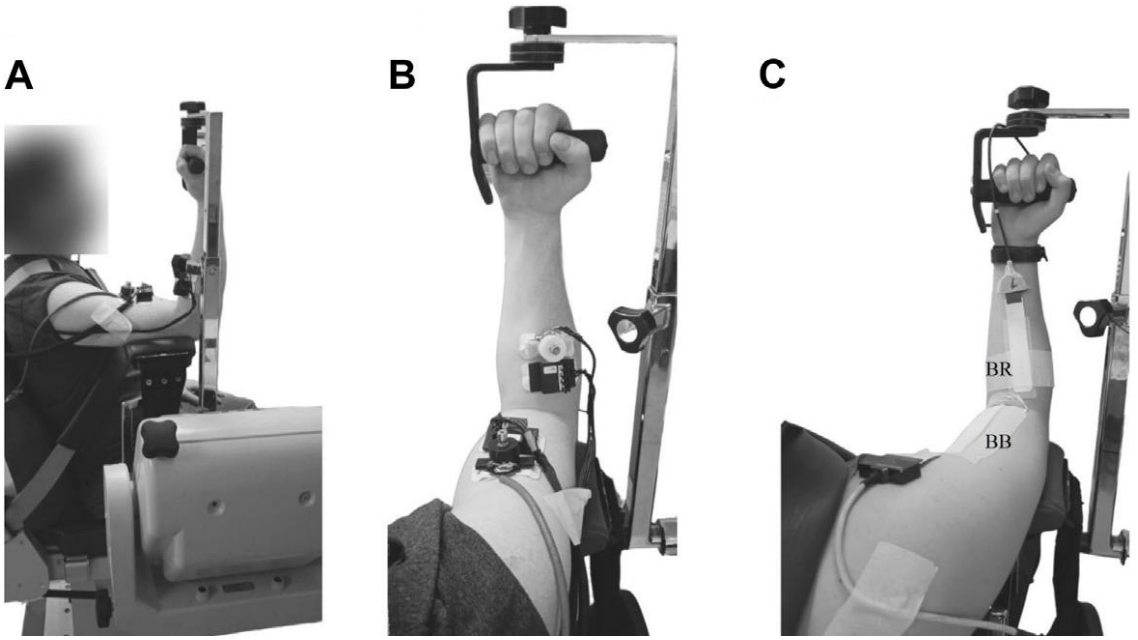

Figure 5.7. Examples of experimental setup for the elastography and electromyography measurements. The placement of the NU-SWE device (A,B) and the EMGs electrode arrays (C) over the free surface of the biceps brachii (BB) and brachioradialis (BR) muscles are shown. Taken from Grinspan et al. (2024).

3.1.4 Data analysis

Experiments 1 and 2

For the resting and stretching measurements performed with the SSI Aixplorer and the NU-SWE, we calculated the mean value and the corresponding standard deviation resulting from the three measurements performed for each subject. From the above, we also calculated the average and standard deviation values corresponding to the entire sample. In addition, for *experiment 2*, we calculated the differences between the shear velocity values in stretched (s) and at rested (r) conditions obtained for each subject with both methods, according to:

$$\Delta V_{T_j}^{\|} = V_{T_j}^{\|}(s) - V_{T_j}^{\|}(r) \qquad (5.9)$$

where j refers to the SSI Aixploirer or NU-SWE.

Experiment 3

Since the exploratory nature of the present study, we considered exclusively the peak values of the $V_s^{\parallel}$ and EMG RMS curves, which occur near the end of the ramps (~40% MVC) for both variables. If the data exhibited good intra-repeatability between both trials for all subjects (see Statistics), the analysis was performed based on the corresponding mean values and the standard deviations of such variables for each condition (5s, 10s, 15s, and 20s). The EMG RMS values were normalized according to the mean activity of the highest amplitude recorded during tasks, for each muscle. For the BR it was on the second trial of 5 s, and for the BB on the second trial of 20 s.

3.1.5 Statistics

Experiments 1 and 2

The variables obtained from the data analysis described in Section 3.1.4 were analyzed according to the Bland-Altman plot, to compare the results obtained with both methods. A correlation analysis was also carried out, involving the realization of the correlation plots and the calculus of the corresponding correlation coefficients.

Experiment 3

To assess the intra-repeatability between both trials for each condition, we calculated the intraclass correlation coefficient (ICC) for each muscle from the peak values of $V_s^{\parallel}$ and RMS EMG obtained in all volunteers. Besides, a two-sample t-test for difference of means was carried out in order to compare the results of the peak $V_s^{\parallel}$ and RMS EMG values vs. task duration at the inter-muscle and the intra-muscle levels. The level of significance was set at $p < 0.05$.

3.2 Results

Experiments 1 and 2

Table 5.1 shows the average results for the measurements performed with the SSI Aixplorer and NU-SWE, both at stretched and rested positions during *experiments 1* and *2*. On the other hand, the Bland-Altman plots corresponding to each experiment revealed a null mean difference, indicating that no systematic bias exists between the measurements obtained with both methods (Figures 5.8A and 5.9A). Thus, as a general picture, the results show a good overall agreement between them. However, the results of *experiment 1* showed a poor correlation between the elasticity values measured with SSI Aixplorer and NU-SWE at rest (Figure 5.8 B). On the contrary, a high correlation between methods was found for the relative elastic change at rested and stretched positions characterized in *experiment 2* (Figure 5.9 B).

Table 5.1. Mean values and standard deviations (between parentheses) of shear velocity measured with SSI Aixplorer and NU-SWE in *experiments 1* and *2*.

$V_s^{\parallel}$ (m/s)	SSI Aixplorer	NU-SWE
Experiment 1		
BF	2.10 (0.29)	2.04 (0.14)
RF	2.14 (0.23)	2.16 (0.20)
Experiment 2		
Rest	2.15 (0.23)	2.43 (0.38)
Stretched	5.66 (1.66)	6.02 (1.07)

Experiment 3

As is shown in Table 5.2, the ICC values obtained for BB and BR muscles denote good reproducibility between the peak $V_s^{\parallel}$ measured in both trials for each condition. In this sense, the averaged values of the peak $V_s^{\parallel}$ and EMG RMS activities from both trials are representative of each task. Therefore, in what follows, the analysis

is performed based on such mean values for both muscles in each condition ($\bar{V}_s^{\|}{}_{BB_{max}}$, $\bar{V}_s^{\|}{}_{BR_{max}}$; $\overline{EMG\ RMS}_{BB_{max}}$, $\overline{EMG\ RMS}_{BR_{max}}$).

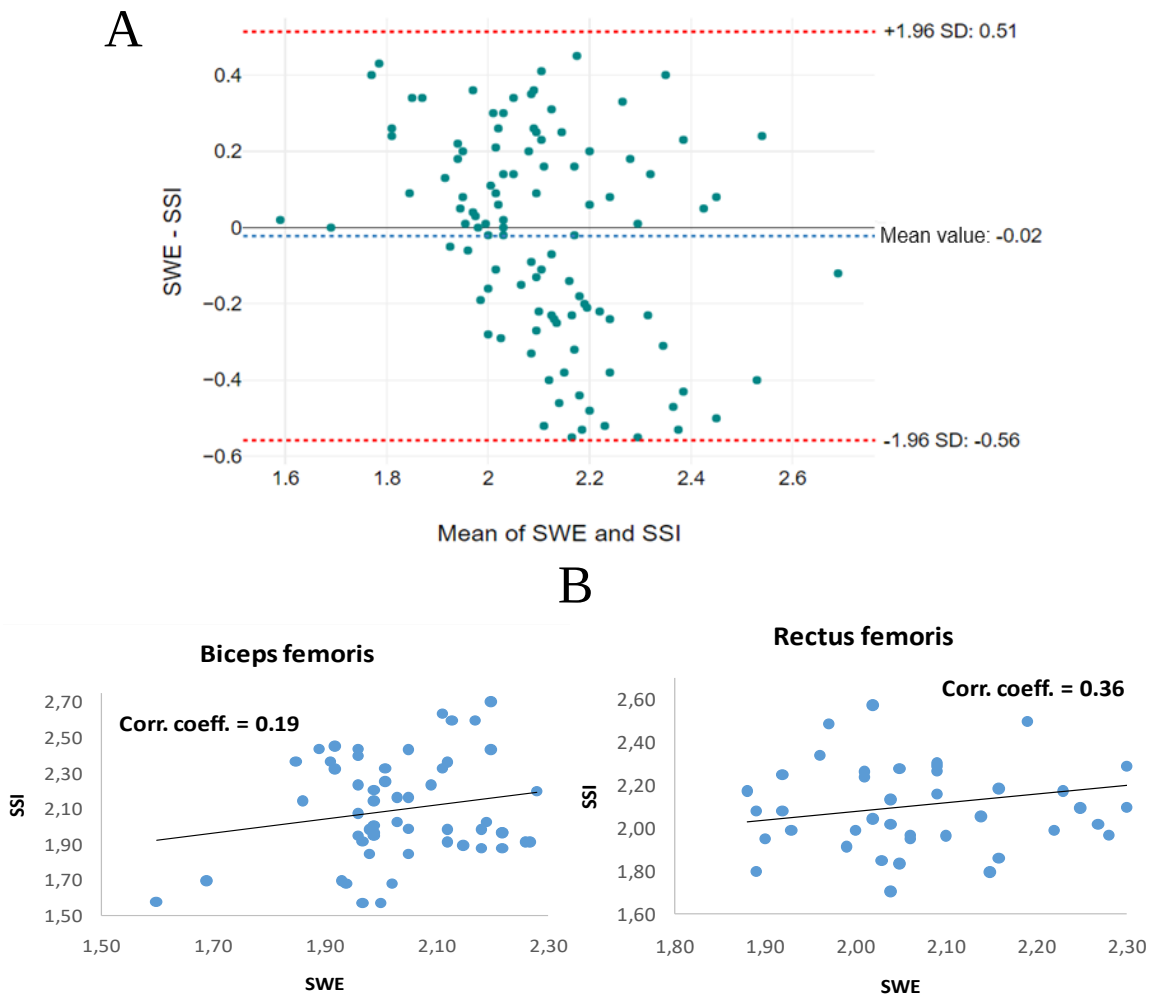

Figure 5.8. Results of *experiment 1*. A: The Bland-Altman plot of the resting values measured on biceps femoris and rectus femoris muscles with SSI Aixplorer and NU-SWE revealed a null mean difference between both methods, indicating no systematic bias between them. B: The correlation analysis performed in each muscle denoted a poor correlation between the shear velocities provided by both elastographic methods in resting conditions. Values in m/s.

Table 5.2. ICC coefficients calculated from the peak $V_s^{\|}$ and EMG RMS values obtained for both trials of each task in the BB and BR muscles of all subjects.

	5 s	10 s	15 s	20 s
Peak $V_s^{\|}$				
ICC_{BR}	0.93	0.94	0.99	0.52
ICC_{BB}	0.89	0.95	0.90	0.78
Peak EMG RMS				
ICC_{BR}	0.73	0.77	0.50	0.66
ICC_{BB}	0.73	0.85	0.72	0.48

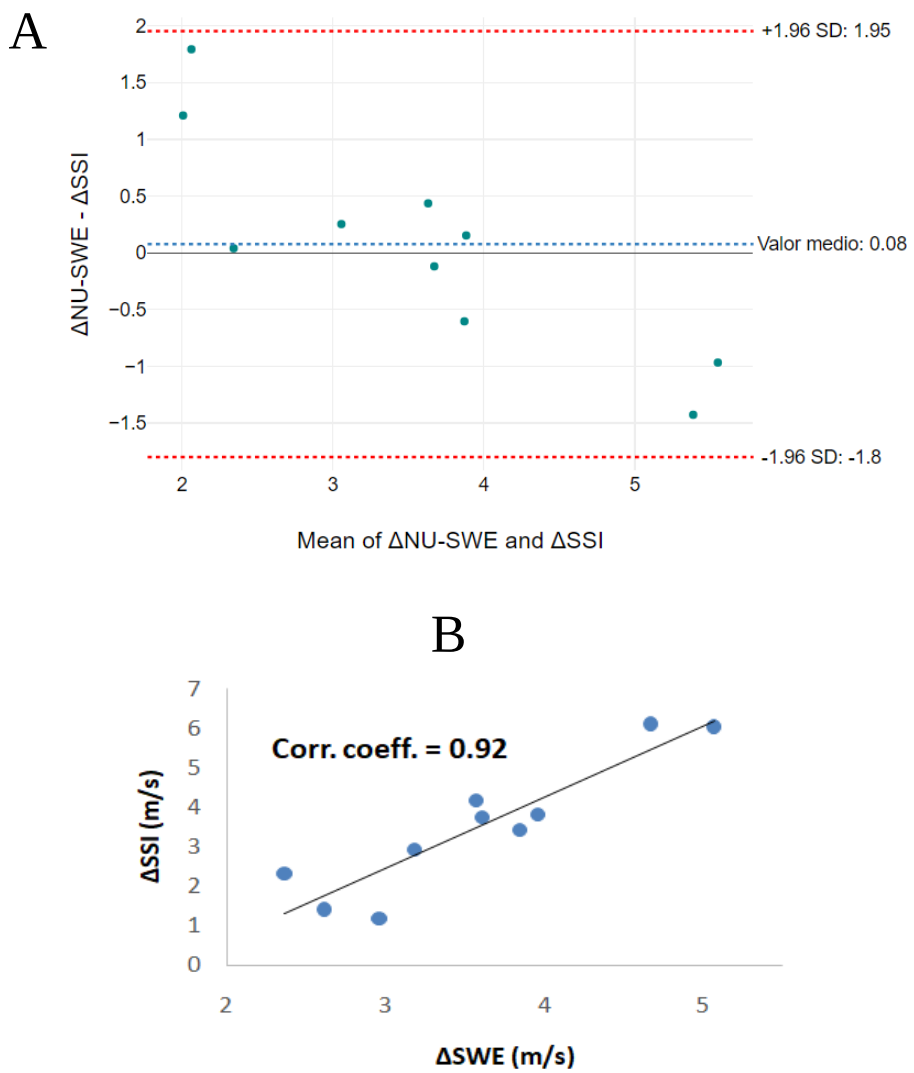

Figure 5.9. Results of *experiment 2*. A: The Bland-Altman plot of the relative elastic change between the rested and stretched positions in the rectus femoris muscle revealed a null mean difference between the SSI Aixplorer and NU-SWE, indicating no systematic bias between such methods. B: The correlation analysis denoted a high correlation of the relative elastic change among rested and stretched conditions characterized by both methods. Values in m/s.

Figure 5.10 shows individual curves of $V_s^{\parallel}$ obtained simultaneously in BB and BR for two volunteers in each condition. In addition to having been obtained simultaneously for each muscle, the $V_s^{\parallel}$ values were measured with a sufficiently temporal resolution, thus allowing an adequate characterization of the contractions during the execution of each task. As is observed for both subjects, when the task duration is shorter, the peak $V_s^{\parallel}$ of BR reaches higher values than BB. As time increases, the peak $V_s^{\parallel}$ of BR decreases while those of BB increase. In this way, for tasks of longer

duration, the relative magnitude of the peak $V_s^{\parallel}$ values tend to invert with respect to tasks performed in shorter times.

Comparing the $\bar{V}_s^{\parallel}{}_{max}$ values at the intra-muscular level, the results for the BB and BR muscles of the entire data set behaved in the same way. Thus, the t-test revealed the existence of significant differences between the $\bar{V}_s^{\parallel}{}_{BR_{max}}$ and $\bar{V}_s^{\parallel}{}_{BB_{max}}$ values obtained between the ramps of 5 vs. 15 and 20 s (p = 0.04 and 0.03, respectively, for BR; p = 0.02 and 0.01, respectively, for BB), not being significant between 5 vs. 10 s, 10 vs. 15 s, 10 vs. 20 s, 15 vs. 20 s (p = 0.12, 0.29, 0.25, 0.44, respectively, for BR; p = 0.05, 0.32, 0.09, 0.16, for BB). On the other hand, inter-muscular comparisons showed the existence of significant differences between the $\bar{V}_s^{\parallel}{}_{BR_{max}}$ and $\bar{V}_s^{\parallel}{}_{BB_{max}}$ values for the 5, 10, and 15 s tasks (p = 0.00, 0.00 and 0.04, respectively), being not significantly different for the 20 s task (p = 0.29). All these results are summarized in Table 5.3 and Figure 5.11.

Table 5.3. $\bar{V}_{s\,max}^{\parallel}$ values and standard deviation (between parentheses) for BB and BR muscles obtained from both trials of each task in all subjects.

	5 s	10 s	15 s	20 s
$\bar{V}_{s\,BB_{max}}^{\parallel}$ (m/s)	5.25 (1.67)	6.55 (2.33)	6.96 (2.51)	8.33 (3.41)
$\bar{V}_{s\,BR_{max}}^{\parallel}$ (m/s)	11.42 (2.91)	9.64 (3.38)	9.02 (3.28)	8.90 (3.28)

The normalized $\overline{EMG\ RMS}_{BR_{max}}$ and $\overline{EMG\ RMS}_{BB_{max}}$ activities showed the same behavior as the $\bar{V}_s^{\parallel}{}_{BR_{max}}$ and $\bar{V}_s^{\parallel}{}_{BB_{max}}$. As seen in Figure 5.12, for each condition, such normalized values decreased and increased with task duration, for BR and BB, respectively. Nevertheless, the results of the t-test did not show significant differences at the intra-muscular level concerning the normalized $\overline{EMG\ RMS}_{BR_{max}}$ (p = 0.37, 0.20,

0.20, for 5 vs. 10, 15, 20 s, respectively; p = 0.32, 0.31, for 10 vs. 15 and 10 vs. 20 s, respectively; p = 0.48, for 15 vs. 20 s). The normalized $\overline{EMG\ RMS}_{BB_{max}}$ only showed a

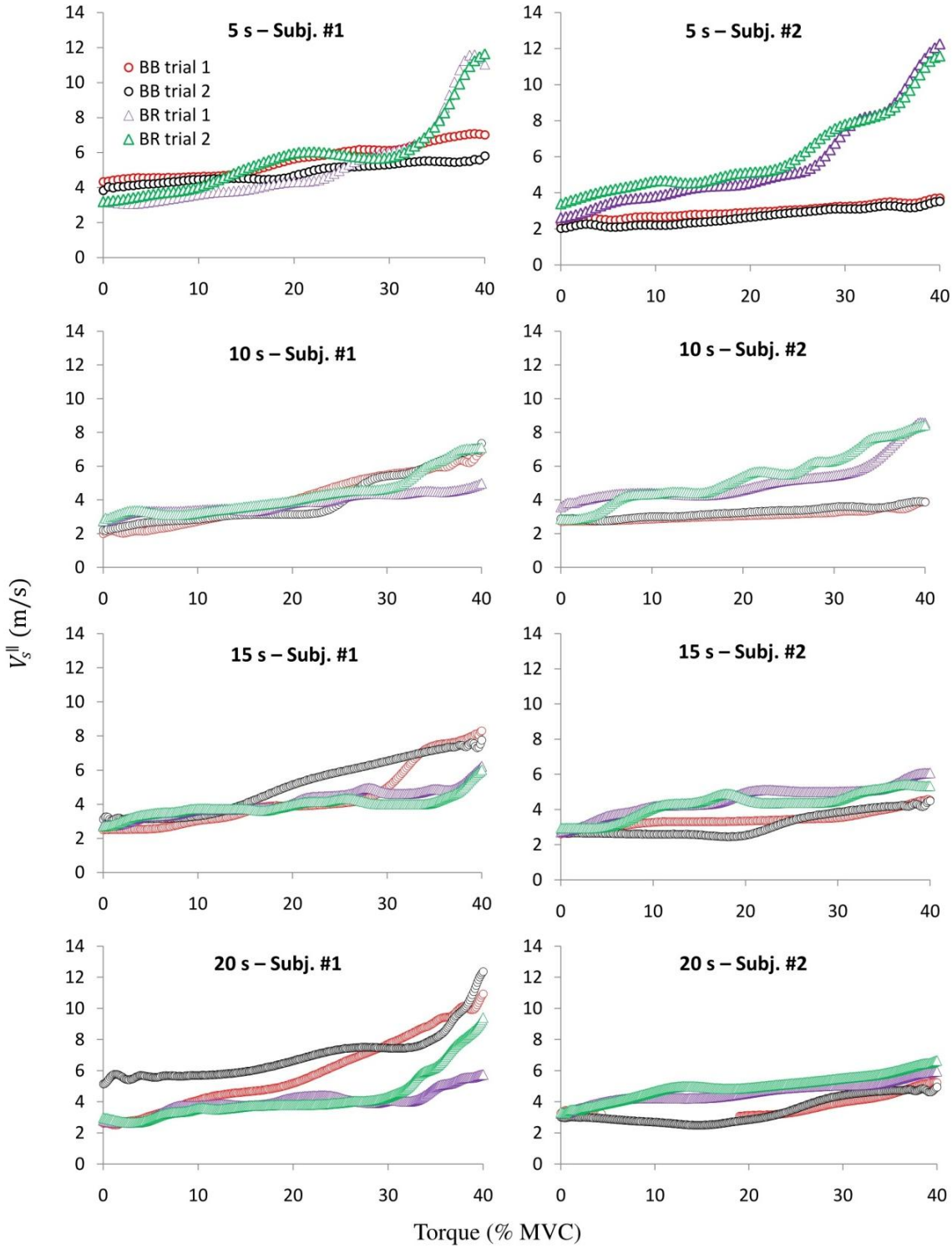

Figure 5.10. Two typical examples of the $\bar{V}_s^{\parallel}$ vs. time data obtained at a high sampling rate in the BB and BR muscles are shown. The corresponding curves to each trial were obtained simultaneously in both muscles during the execution of the tasks at 8, 4, 2.67, and 2 %MVC/s for the 5, 10, 15, and 20 s tasks, respectively.

significant difference between the values at 5 vs. 20 s (p = 0.03), while this was not observed for the other inter-muscle comparisons (p = 0.21 and 0.07 for 5 vs. 10 s and 5 vs. 15 s, respectively; p = 0.22 and 0.13, for 10 vs. 15 and 10 vs. 20 s, respectively; p = 0.37, for 15 vs. 20 s). At the inter-muscular level, significant differences were found between the normalized $\overline{EMG\ RMS}_{BR_{max}}$ and $\overline{EMG\ RMS}_{BB_{max}}$ for 5 s (p= 0.03), while no significant differences were found for 10, 15 and 20 s (p = 0.19, 0.36, 0.24, respectively).

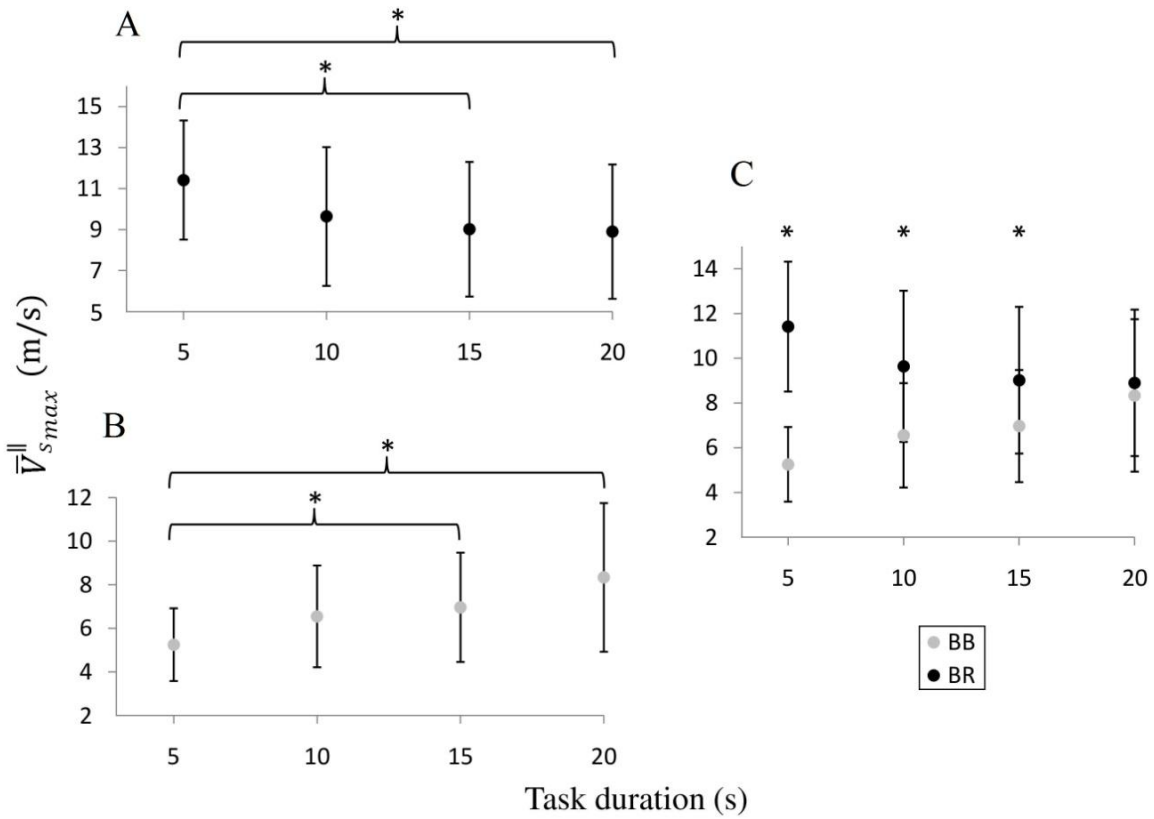

Figure 5.11. Intra (A, B) and inter-muscular (C) comparisons of the $\overline{V}^{\parallel}_{s\,max}$ values obtained for the respective task durations. The symbol * denotes the existence of significant differences.

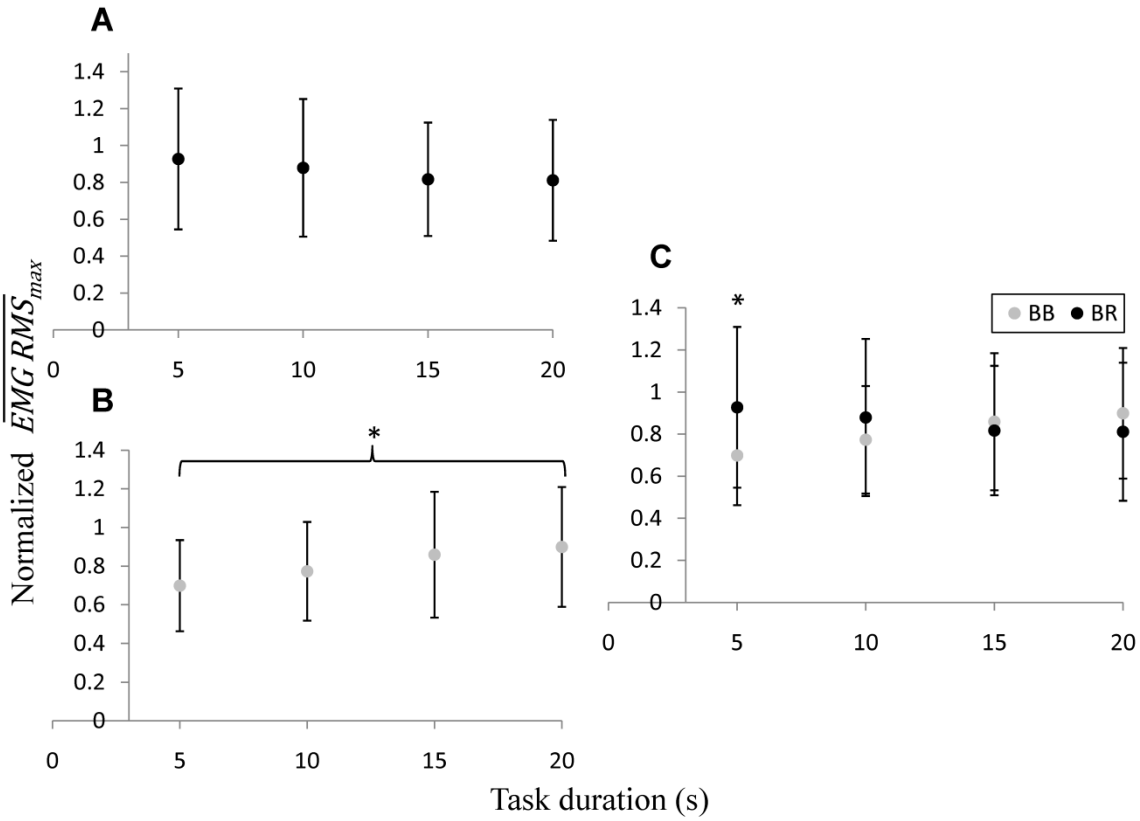

Figure 5.12. Intra (A, B) and inter-muscular (C) comparisons of the normalized $\overline{EMG\ RMS}_{max}$ values obtained for the respective task durations. The symbol * denotes the existence of significant differences.

3.3 Discussion

Comparison between SSI Aixplorer and NU-SWE

As we have seen through the Bland-Altman plots, the shear velocity estimates provided by the NU-SWE showed a good agreement with those of the SSI Aixplorer. This was observed in different experimental conditions, involving measurements both in rest and stretch, where there is a significant change in the mechanical properties of skeletal muscle. Thus, the null mean difference shown by the Bland-Altam plots, for both *experiments* 1 *and* 2 conditions, denotes that the measurement of muscle elasticity with NU-SWE has no systematic bias compared to the estimates provided by the reference SSI Aixplorer method. However, the correlation analysis for the resting measurements of *experiment 1* denoted a very low correlation between them (Figure

5.8B). This is because, in skeletal muscle at rest, the standard deviation of the measurements is comparable to the resolution of both methods, as depicted in Table 5.1. As a result, random fluctuations impede the attainment of a stronger correlation. On the other hand, *experiment 2* was more suitable for establishing a reliable correlation, since the measurement conditions determined well-differentiated results as a function of the resolution of each method (Table 5.1). In this regard, our results showed a high correlation between the SSI Aixplorer and NU-SWE methods, to characterize relative elasticity changes in skeletal muscle, as those presented between rested and stretched conditions (Figure 5.9B).

Therefore, all of the above adds information to the preliminary validations of NU-SWE concerning shear wave elastography, carried out in previous works carried out in soft tissue-mimicking phantoms and beef samples (Benech et al., 2019, 2021; Grinspan et al., 2016). Thus, the results of *experiments 1* and *2* provide answers to pending aspects of NU-SWE development expressed in Grinspan et al., (2021, 2024), regarding the validity of the estimates concerning the standard ultrasound elastography methods. Therefore, in light of all the above, the results of this work show that both methods bring comparable results of the mean value of the shear wave velocity within the ROI.

Novel aspects of NU-SWE for muscle biomechanical research

The purpose of *experiment 3* was to show the performance of the updated version of the NU-SWE method and the novel measuring capabilities that arise from its new features. In this regard, the work showed that this method is able to measure muscle elasticity in experimental conditions that have been impracticable with the current ultrasonic and low-frequency elastographic methods. In this way, interesting mechanical properties of skeletal muscle emerged from using this version of the NU-

SWE. Therefore, the results of the present study could be a first step in order to continue delving into the knowledge of muscle biomechanics based on the application of elastography.

The results of the isometric flexion ramps performed up to 40% MVC in 20 s are the most adequate to compare the results of the previous studies regarding the present work. In this task of our protocol, the contraction rate was 2% of MVC/s, being comparable to most of the biomechanical studies performed in skeletal muscle with others elastographic methods. In these conditions, different works have reported μ_L values for the BB and BR muscles ranging from ~ 10 - 150 and 5 - 60 kPa, respectively, between 0 - 40% MVC, both using SWE as well as the previous version of NU-SWE (Nordez & Hug., 2010; Yoshitake et al., 2014; Lapole et al., 2015; Bouillard et al., 2012b; Grinspan et al., 2023). These values agree, both qualitatively and quantitatively, with the range of shear velocities shown in Figures 5.10 and 5.11.

The tasks performed in 5, 10 and 15 s correspond to rates of contraction of 8, 4 and 2.67% MVC/s, respectively. These rates are higher than those usually induced by the protocols that can be applied with SWE, which must be slow and controlled contractions due to their limited sample frequency (~1-2 Hz). Particularly, the measurements of the present work were carried out at 15 Hz. No previous work has described muscle elasticity measurements at such a sampling frequency, either with surface wave elastography or shear wave elastography. In our previous work with NU-SWE, the highest sampling rate reached in the measurements was 1.4 Hz (Grinspan et al., 2021). On the other hand, the sampling rates reported in the literature regarding the application of the SWE methods in skeletal muscle ranges between 1-2 Hz. The SWE method generates a "push" over most of the tissue using extended sonification times of approximately 200 μs each. The dimension of a typical region of interest (ROI) for

imaging elasticity in muscles is 2 to 3 cm wide and 2 to 3 cm deep. Imaging this area requires several pushes, not less than 8 (4 in lateral dimension and at least 2 in-depth). Therefore, only the pulsation time lasts approximately 1 ms. The duration of the ultrafast sequence to track the propagation of the shear wave depends on the depth of observation of the ROI, but the typical PRF is between 3 and 5 kHz, adding times on the order of 300 μs to each frame. If this information were to be stored in memory for offline processing, the theoretical sampling rate is on the order of 10^2 Hz. However, this theoretical limit cannot be reached in practice, as it would imply sending pushes every ~0.01 s, which could seriously damage the transducer. Besides, in commercially available devices, the time required for memory transfer and online processing for real-time display eventually reduces the frame rate to values of 1-2 Hz. To our knowledge, there are no commercial SWE devices with elasticity frame rates higher than this, so the updated version of the NU-SWE represents a novel alternative in this regard.

The above allows performing protocols involving faster contractions, thus emerging novel muscular elastic behaviors as those described by our results. In this sense, our measurements showed, both at the individual and average level, a temporal dependence regarding the elastic behavior of the BB and BR muscles during the isometric flexion of the elbow joint. Such temporal dependence was manifested both at the inter-muscular and intra-muscular level, through the differences in the peak $\bar{V}_s^{\parallel}{}_{BR_{max}}$ and the $\bar{V}_s^{\parallel}{}_{BB_{max}}$ values. While the maximum shear elasticity reached by the BR decreases with the task duration, the opposite behavior was observed in the BB (Figs. 5.10 and 5.11). Thus, at the intra-muscle level, significant differences were found between the values of the tasks executed in 5 s compared to 15 and 20 s. On the other hand, the inter-muscle comparison showed that the peak $\bar{V}_s^{\parallel}$ values of BB and BR were significantly different between all conditions, except for the 20 s-task, which agrees

with the results of the previously referred works. As far as we know, these behaviors have not been previously described with elastography. Since the muscle elasticity reflects the force exerted by the muscle, the above may have important connotations concerning the motor control of the synergistic elbow flexor muscles and the temporal dependence of the load sharing between them (Bouillard et al., 2012b; Grinspan et al., 2023).

As is depicted in Figure 5.12, the measurements of the EMG RMS showed the same behavior pattern as the elastography concerning the average peak activity as a function of the task duration, exhibiting a correlation factor of 0.96 and 0.95 for the BB and BR, respectively. While the normalized $\overline{EMG\ RMS}_{BR_{max}}$ tends to decrease as the total time of the flexion ramps increases, the normalized $\overline{EMG\ RMS}_{BB_{max}}$ exhibits the opposite trend. This is consistent with previous works that have shown the close relationship between the muscle shear elastic modulus and their EMG activity (Nordez & Hug, 2010; Yoshitake et al., 2014; Lapole et al., 2015; Grinspan et al., 2021; Zimmer et al., 2023). Such studies have suggested the validity of the linear model to describe this relationship, during the isometric flexion of the elbow flexors according to similar contraction intensities to those of the present work. Only the inter-muscular comparison between $\overline{EMG\ RMS}_{BR_{max}}$ and $\overline{EMG\ RMS}_{BB_{max}}$ for the 5 s-task exhibited significant differences. In addition to their corresponding results of $\bar{V}_s^{\parallel}{}_{max}$ for such tasks (Figure 41), this clearly reflects the biomechanical role of the BR muscle in stabilizing the elbow joint at fast contraction velocities, through the coaptation of radius head to the capitulum of the humerus, offering an adequate support for the subsequent action of the BB. This process tends to be balanced out at smoother contractions as task execution time increases. At the intra-muscular level, only the mean activities of the BB muscle between the 5 and 20 s-tasks were significantly different. This denotes the functional

variability of the BB concerning its isometric contraction at different velocities, agreeing with the corresponding results of $\bar{V}_s^{\parallel}{}_{max}$. In the context of our study, the absence of significant differences in the inter and intra-muscular comparisons between the values of the normalized $\overline{EMG\ RMS}_{BR_{max}}$ and $\overline{EMG\ RMS}_{BB_{max}}$, compared to the respective comparisons of $\bar{V}_s^{\parallel}{}_{max}$, does not necessarily indicate the absence of differences in peak EMG RMS activity in such situations. The above could have been conditioned by the limited size of the sample since specific variations in the measurements can significantly affect their standard deviation. Besides, the EMG signals of the BB and BR muscles in each condition may also have been affected by the crosstalk of other adjacent muscles (Solomonow et al., 1994; Hug et al., 2015a, b). This phenomenon does not affect the elastographic measurements since their nature is mechanical and not electrical, which is a possible cause of the discrepancy in the results. In this sense, it has been proposed that elastography can help to reconsider our current understanding of muscle co-contraction (Hug et al., 2015a; Avrillon et al., 2018). Particularly, the updated version of the NU-SWE provides the opportunity to add the simultaneity and the temporal dimension to this approach, unlike other elastographic methods.

All of the above indicates that mean elasticity measurements using surface waves add advantageous features in biomechanical research. The device used in this work is portable, low cost and easy to handle. It allows measuring on several muscles simultaneously and at a high sample rate. If a proper strategy for locating and positioning the wave source and sensors is followed, no significant errors in the results occur due to the placement of the device. This is supported by the repeatability analysis performed in our previous work with NU-SWE where, although the manipulation of the wave source during measurements could have introduced variation between

measurements, it was not reflected in the results (Grinspan et al., 2021). In this sense, the new configuration of the NU-SWE employed in this work overcame such a limitation, adding even more certainty regarding the reproducibility of the measurements. Concerning the relative alignment of the array of sensors and the fibers' orientation, it is important to highlight that, as the BB and BR are parallel and fusiform muscles, knowing their anatomical location on the arm is sufficient to identify the fiber orientation accurately. However, in pennate muscles, identifying the fibers' orientation before measurements by B-mode ultrasound and aligning the sensors accordingly, may be helpful to avoid biases related to wave propagation in more complex media.

Although in the present study, the selected sample rate was 15 Hz as it was considered adequate to characterize the contractions of the different tasks, this can be even higher by adjusting the Δt between signals according to the requirements. Thus, the updated version of the NU-SWE allows obtaining $\mu_L$curves with higher temporal resolution, being able to be used both for isometric estimates, as in the present work, and eventually also for measurements in dynamic conditions (e.g., walking, jumps). In this way, the advantageous features of the present version of the NU-SWE are similar to the low-frequency method proposed by Martin et al. (2018) and Keuler et al. (2019) to measure elasticity in tendons. However, this method cannot measure skeletal muscle elasticity as it is based on the Timoshenko beam model, which does not apply to this tissue (Timoshenko 2021, 2022). Therefore, we think NU-SWE provides a novel and valuable alternative to measure muscle elasticity reliably and in conditions hitherto impracticable with ultrasound elastography. In this sense, the results of the present study could be a first step in order to widen the current applications of elastography in muscle biomechanics.

4 – CHAPTER CONCLUSIONS

This Chapter showed that surface wave elastography has some features that can potentially widen the spectrum of applications of elastography in skeletal muscle. Firstly, it was shown that the NU-SWE is able to quantify the elastic shear modulus analogously to the reference SWE methods. Particularly, we found a strong correlation between NU-SWE and the SSI Aixplorer concerning the characterization of relative elastic changes in skeletal muscle. In addition to the above, the updated NU-SWE has other features that can be extremely useful for biomechanics research, which add to its previous advantages in terms of being a low-cost and portable method. Thus, it has been shown that the current version of NU-SWE is able to measure the elasticity of several muscles simultaneously and with a higher sampling rate than previous surface wave methods and the classic SWE. In this way, in the present study we used these characteristics of the method to perform a proof of concept of an experimental protocol previously impracticable with elastography. We measured the elasticity changes of the BB and BR muscles simultaneously during the isometric flexion of the elbow joint at different contraction velocities. As a result, we found that the peak elasticity value for each muscle has a different behavior depending on the time required for the task. For short times, the peak value for BR is significantly higher than for BB. As the time of the task increases, these values approach each other. Such behavior was also observed at the level of the EMG activity of both muscles, indicating that the elastographic results correlate with other methods for characterizing muscle activity. Considering the above, the methodological advances presented in this study widen the applications of elastography in skeletal muscle *in vivo* to delve into the knowledge of muscle biomechanics.

CHAPTER 6

GENERAL CONCLUSIONS AND PERSPECTIVES FOR FUTURE WORK

The present thesis addressed different aspects of muscle biomechanics, which had not been investigated in depth to date. In this regard, the present work made relevant contributions in terms of novel conceptual and methodological approaches, which allowed to address long-standing problems in elastography and muscle biomechanics. All of the above constitutes the foundation of future research lines, which will tend to deepen the developments and findings of the present thesis. Some of these works are already underway in the LAU. Thus, in the following paragraphs, we will briefly detail some of the main ideas derived from the conclusions of this thesis, which will be addressed in the future through the development of new lines of research.

In this way, in Chapter 3 we developed a novel approach by combining the acousto-elasticity theory, the short-range stiffness property, and the ligand-binding framework. Here, the results of this thesis made relevant contributions to understanding the link between the macroscopic skeletal muscle elasticity estimates and its contraction dynamics at a microscale. Particularly, we showed that muscle can be considered structurally and functionally analogous to a receptor-ligand complex and that $C_i(\tau)$ coefficient is the muscle analog of the saturation fraction (Y) of a molecular receptor. This approach proved very useful for studying the muscle synergy between the BB, BR, and BA muscles during isometric elbow flexion, showing that receptor-ligand dynamics underlie the longitudinal shortening of these muscles during load sharing. This offers the possibility of defining a *muscle quality index* based on elastography. Such a measure essentially refers to the ability of muscles to generate force effectively and efficiently. In recent years, different muscle quality indexes have been described based on local

measures of tensiomyography or muscle echogenicity, and functional assessments such as the sit-to-stand test or the relationship between force/power and the total muscle mass (Heckmatt et al., 1982; Reimers et al., 1993; Takai et al., 2009; Arts et al., 2010; Šimunič et al., 2011, 2019; Pillen et al., 2006, 2009; Barbat-Artigas et al., 2012; Reyes-Ferrada et Al., 2022; Hanney et al., 2022). However, the validity of such muscle quality indexes is currently discussed, given the lack of certainty concerning the association between their results and the contractile capacity of muscles at the individual level. In this regard, novel muscle quality indexes could be defined from further derivations of the findings of Chapter 3 in the context of receptor-ligand framework. Thus, for example, as one of the most commonly used parameters for the study of molecular receptors is $K_{0.5}$, which is the ligand concentration for which Y = 0.5, a possible muscle quality index could be $\tau_{0.5}$, being the torque level for which $C_i(\tau) = 0.5$. Future studies will intend to characterize such an elastography-based muscle quality index for both basic and applied research, as well as for practical applications in areas closely related to muscle biomechanics.

In Chapter 4, the formalisms developed in Chapter 3 constituted the basis for purposing a biomechanical model able to estimate the individual muscle forces produced by the BB, BR, and BA muscles during an isometric elbow flexion ramp. This model provided plausible values for the contractile and total muscle forces exerted by these muscles, also revealing the load-sharing between them as the total torque increases. In this way, the above represented a novel solution for a long-standing challenge hitherto unsolved in muscle biomechanics. Further developments based on these results could have different implications. For example, taking into account that $C_i(\tau)$ is directly proportional to the relative shortening of the muscle (Eq. 3.10) and τ is time-dependent, it would be possible to calculate the muscle force/contraction velocity

ratio by using the individual muscle force values obtained through the model. As such ratio has mass/time dimensions (Alexander, 1999), the effectively *contracted muscle mass* (*cmm*) as a function of time (or τ) might be obtained. Thus, in addition to the muscle quality index discussed in the previous paragraph, an alternative muscle quality index of force/power as a function of cmm could also be obtained for individual muscles. On the other hand, although in this thesis the present model has been applied only under isometric conditions, it is important to point out that, in general terms, it is valid for conditions where the acceleration of the system, and thus the net force on it, is 0. This enables extending the use of the model to situations other than those studied in the present thesis. In this regard, the model could also be used to calculate the individual muscle forces during isokinetic tasks involving concentric contractions. Related to the above, as the anatomical configuration of the knee joint is analogous to the elbow joint, future studies will focus on characterizing the individual forces of the quadriceps femoris muscles during knee extension under both isometric and isokinetic conditions. This could have important connotations in terms of basic research on muscle biomechanics, as well as for practical purposes in the rehabilitation of common locomotor disorders.

Other important contributions of the thesis were also related to overcoming the limitations of current reference ultrasonic elastographic methods. In this way, in Chapter 5 we developed a new version of NU-SWE. In addition to being a free-hand, portable, and low-cost method, it can measure the muscle elasticity of more than one muscle simultaneously and with a high sampling frequency (~15 Hz). This made it possible to perform an experimental protocol that involved simultaneous elasticity measurements at different contraction rates, thus allowing obtaining novel results concerning the time dependence of elasticity changes during isometric contraction.

Therefore, this updated version of NU-SWE has the potential to extend the current applications of elastography in muscle biomechanics, making it possible to carry out experimental protocols unviable with elastography to date. For example, it could be possible to perform experimental protocols in dynamic conditions, like in isokinetic contractions as commented in the previous paragraph. For example, this allows to perform elasticity measurements in dynamic conditions. As an example of the above, Figure 6.1A displays preliminary muscle elasticity measurements of the rectus femoris

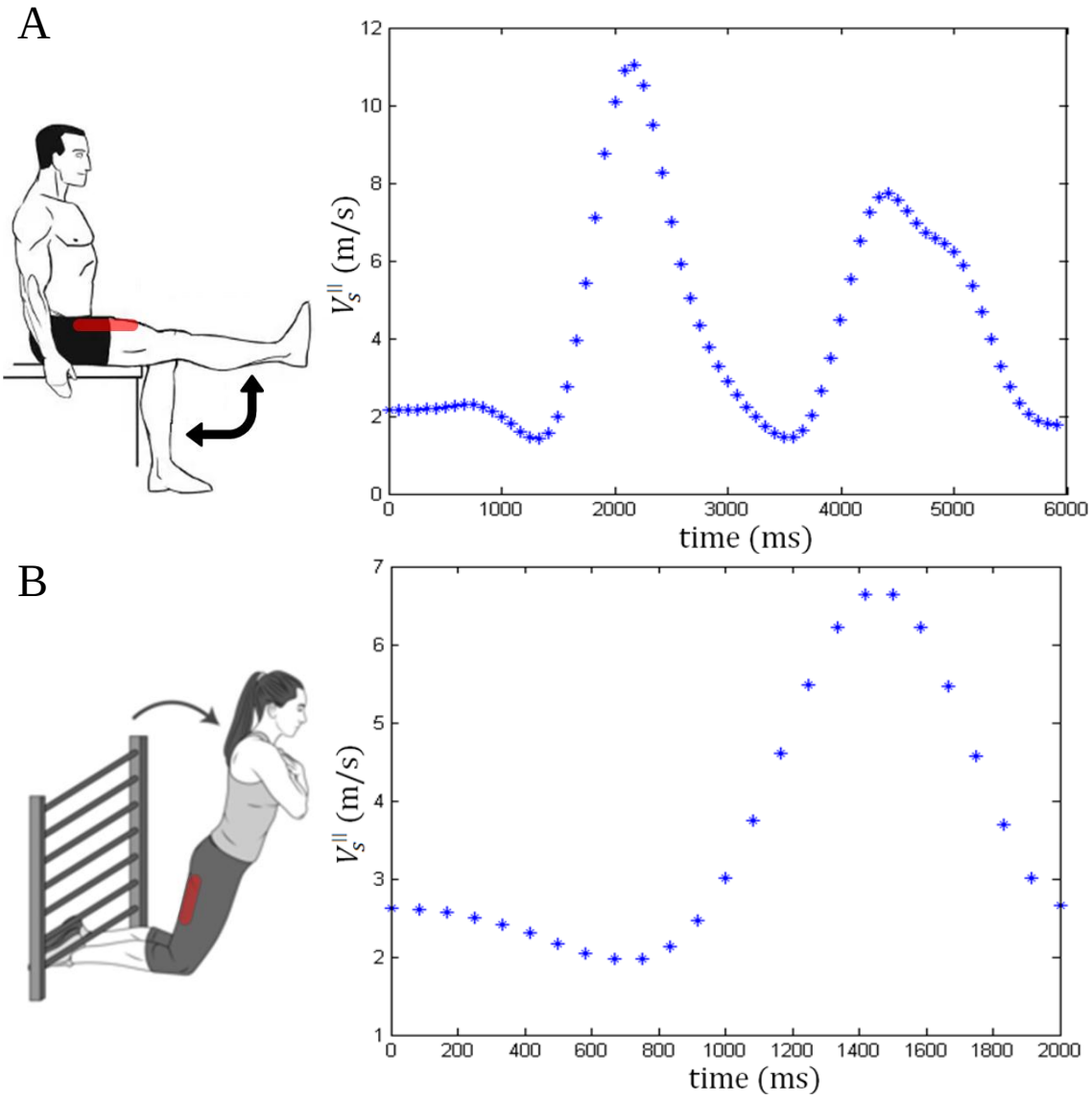

Figure 6.1. Application of the NU-SWE for measuring the elasticity change of the rectus femoris and biceps femoris muscles (indicated in red) during two cycles of flexion-extension of the knee joint (A) and the Nordic curl (B), respectively. In both cases, the sampling frequency was 13 Hz.

muscle characterized during the execution of the flexion-extension of the knee joint. As seen, the NU-SWE allows measuring the elasticity rise of such a muscle during its extension, and it decreases during the extension, in agreement with its biomechanical function. This can be useful to carry out simultaneous measurements of the quadriceps femoris muscles during the isokinetic extension of the knee joint, in order to estimate the individual muscle forces according to the further derivation of the model developed in Chapter 4, as discussed in the previous paragraph. The above is currently in earlier stages of research in the LAU and will be developed in depth in upcoming works. On the other hand, Figure 6.1B shows the application of the updated version of the NU-SWE to measure the elasticity of the biceps femoris muscle during the execution of the Nordic curl, which is considered the gold standard exercise indicated for increasing eccentric strength and injury prevention. This work is currently ongoing in the LAU as a part of the doctoral thesis of Adrian Magallanes[4], showing the potential utility of the updated version of NU-SWE in sports and health.

As described in Chapter 2, most of the elastographic studies in skeletal muscle assume the skeletal muscle is a purely elastic, transversely isotropic tissue. Thus, the shear elasticity values obtained in the present thesis were also based on the realization of such a simplification concerning the material nature of the muscle. In this way, future works derived from the results of the present thesis could include the viscosity in the estimations of the shear elastic modulus of the muscle. This could be done by obtaining $V_s^{||}$ vs. frequency dispersion curves with NU-SWE. Still, it may be difficult due to the uncertainty in determining the area where only Rayleigh waves propagate for the

[4]Magallanes, A. Assessment of functional and mechanical properties of the hamstrings and quadriceps using the Nordic and reverse Nordic curl in elite youth soccer players. Doctoral thesis. PROINBIO (2023-ongoing).

different subjects (Benech et al., 2017). However, another possibility consists of characterizing attenuation curves for the amplitude of the shear waves regarding the distance. Particularly, recent advances in this matter are currently being developed in the LAU (Camargo et al., 2024)[5]. Briefly, a diffraction correction has been introduced by analytically solving the wave equation for a line source in a transversely isotropic tissue. Such a correction was tested both in beef samples as well as in rested and isometrically contracted biceps brachii muscle, showing a good agreement regarding numerical simulations based on a Green's function algorithm for an anisotropic and viscoelastic media (Chatelin et al., 2015). Therefore, with further improvements, this approach will be applied in future works to provide a complementary perspective by considering the viscosity in estimating the shear elasticity based on shear wave velocity measurements.

[5]Camargo, A., Budelli E., Gennisson J-L., Frappart, T., Benech, N., Negreira, C., Brum, J. Shear Wave Attenuation Measurement in Transversely Isotropic Tissue. *IEEE UFFC Latin America Ultrasonics Symposium*. 8-10 de mayo de 2024, Montevideo, Uruguay.

REFERENCES

Abbott, B. C., & Ritchie, J. M. (1951). The onset of shortening in striated muscle. The Journal of physiology, 113(2-3), 336.

Ackermann, M., & Schiehlen, W. (2009). Physiological methods to solve the force-sharing problem in biomechanics. In *Multibody dynamics: Computational methods and applications* (pp. 1-23). Dordrecht: Springer Netherlands.

Adkins, A. N., Fong, R. M., Dewald, J. P., & Murray, W. M. (2022). Variability of in vivo sarcomere length measures in the upper limb obtained with second harmonic generation microendoscopy. *Frontiers in Physiology*, *12*, 817334.

Alexander, R. M. (1999). Energy for animal life. *Oxford University Press*, New York.

Amis, A. A., Dowson, D., & Wright, V. (1980). Elbow joint force predictions for some strenuous isometric actions. *Journal of Biomechanics*, *13*(9), 765-775.

An, K. N., Kwak, B. M., Chao, E. Y., & Morrey, B. F. (1984). Determination of muscle and joint forces: a new technique to solve the indeterminate problem.

Arslan, Y. Z., Karabulut, D., Ortes, F., & Popovic, M. B. (2019). Exoskeletons, exomusculatures, exosuits: dynamic modeling and simulation. *Biomechatronics (Elsevier)*, 305-331.

Arts, I. M., Pillen, S., Schelhaas, H. J., Overeem, S., & Zwarts, M. J. (2010). Normal values for quantitative muscle ultrasonography in adults. *Muscle & Nerve*, *41*(1), 32-41.

Ateș, F., Hug, F., Bouillard, K., Jubeau, M., Frappart, T., Couade, M., Bercoff, M., & Nordez, A. (2015). Muscle shear elastic modulus is linearly related to muscle torque over the entire range of isometric contraction intensity. *Journal of Electromyography and Kinesiology*, *25*(4), 703-708.

Avrillon, S., Hug, F., & Guilhem, G. (2018). Between-muscle differences in coactivation assessed using elastography. *Journal of Electromyography and Kinesiology*, *43*, 88-94.

Avrillon, S., Lacourpaille, L., Hug, F., Le Sant, G., Frey, A., Nordez, A., & Guilhem, G. (2020). Hamstring muscle elasticity differs in specialized high-performance athletes. *Scandinavian journal of medicine & science in sports*, *30*(1), 83-91.

Bagni, M. A., Cecchi, G., Colombini, B., & Colomo, F. (2002). A non-cross-bridge stiffness in activated frog muscle fibers. *Biophysical Journal*, *82*(6), 3118-3127.

Barbat-Artigas, S., Rolland, Y., Zamboni, M., & Aubertin-Leheudre, M. (2012). How to assess functional status: a new muscle quality index. *The journal of nutrition, health and aging*, *16*(1), 67-77.

RERERENCES

Benech, N. "Elastografía ultrasonora de medios viscoelásticos con ondas de cizalla de baja frecuencia," Tesis de Maestría, Laboratorio de Acústica Ultrasonora, Univ. De la República-PEDECIBA, Montevideo, Uruguay, 2004.

Benech, N. "Elastografía Ultrasonora en sólidos blandos. Análisis del proceso de retorno temporal y aplicación al monitoreo de temperatura." Tesis de Doctorado, Laboratorio de Acústica Ultrasonora, Univ. De la República-PEDECIBA, Montevideo, Uruguay, 2008.

Benech, N., Aguiar, S., Grinspan, G. A., Brum, J., & Negreira, C. (2012). In vivo assessment of muscle mechanical properties using a low-cost surface wave method. In *2012 IEEE International Ultrasonics Symposium*, 2571-2574.

Benech, N., Grinspan, G., Aguiar, S., Brum, J., Negreira, C., & Gennisson, J. L. (2015). Analysis of Rayleigh-Lamb modes in soft-solids with application to surface wave elastography. *Physics Procedia*, *70*, 175-178.

Benech, N., Brum, J., Grinspan, G., Aguiar, S., & Negreira, C. A. (2017). Analysis of the transient surface wave propagation in soft-solid elastic plates. *The Journal of the Acoustical Society of America*, *142*(5), 2919-2932.

Benech, N., Grinspan, G., Aguiar, S., & Negreira, C. (2019). Surface wave elastography: device and method. *Measurement Science and Technology*, *30*(3), 035701.

Benech, N., Camargo, A., & Negreira, C. (2022). Simplified Green's function for surface waves in quasi-incompressible elastic plates with application to elastography. *Journal of Physics: Condensed Matter*, *34*(21), 214004.

Bercoff, J., Tanter, M., & Fink, M. (2004a). Supersonic shear imaging: a new technique for soft tissue elasticity mapping. *IEEE transactions on ultrasonics, ferroelectrics, and frequency control*, *51*(4), 396-409.

Bercoff, J. (2004b). *L'imagerie échographique ultrarapide et son application à l'étude de la viscoelasticité du corps humain* (Doctoral dissertation, ESPCI ParisTECH).

Bercoff, J., Tanter, M., & Fink, M. (2004c). Sonic boom in soft materials: The elastic Cerenkov effect. *Applied Physics Letters*, *84*(12), 2202-2204.

Bertsekas, D. P. (2014). Constrained optimization and Lagrange multiplier methods. *Academic press*, New York.

Binder, M.D., Mendell, L.M. (1990) The segmental motor system. *Oxford University Press*, New York.

Blangé, T., Karemaker, J. M., & Kramer, A. E. (1972). Elasticity as an expression of cross-bridge activity in rat muscle. *Pflügers Archiv*, *336*, 277-288.

Bouillard, K., Nordez, A., & Hug, F. (2011). Estimation of individual muscle force using elastography. *PloS one*, *6*(12), e29261.

Bouillard, K., Hug, F., Guével, A., & Nordez, A. (2012a). Shear elastic modulus can be used to estimate an index of individual muscle force during a submaximal isometric fatiguing contraction. *Journal of applied physiology*, *113*(9), 1353-1361.

Bouillard, K., Nordez, A., Hodges, P. W., Cornu, C., & Hug, F. (2012b). Evidence of changes in load sharing during isometric elbow flexion with ramped torque. *Journal of biomechanics*, *45*(8), 1424-1429.

Brinckmann, P., Frobin, W., Leivseth, G. (2002). Musculoesqueletal Biomechanics. *Thieme*, New York.

Brooke, M. H., & Kaiser, K. K. (1970). Muscle fiber types: how many and what kind? *Archives of neurology*, *23*(4), 369-379.

Carrascal, C. A., Chen, S., Urban, M. W., & Greenleaf, J. F. (2017). Acoustic radiation force-induced creep–recovery (ARFICR): A noninvasive method to characterize tissue viscoelasticity. *IEEE transactions on ultrasonics, ferroelectrics, and frequency control*, *65*(1), 3-13.

Carcione, J. M., Kosloff, D., & Kosloff, R. (1988). Wave-propagation simulation in an elastic anisotropic (transversely isotropic) solid. *The Quarterly Journal of Mechanics and Applied Mathematics*, *41*(3), 319-346.

Chatelin, S., Gennisson, J. L., Bernal, M., Tanter, M., & Pernot, M. (2015). Modelling the impulse diffraction field of shear waves in transverse isotropic viscoelastic medium. *Physics in Medicine & Biology*, *60*(9), 3639.

Catheline, S. "Interférométrie-Speckle ultrasonore: Application à la mesure d'élasticité". Doctoral Thesis, Université Paris-Diderot-Paris VII, France, 1998.

Catheline, S., Wu, F., & Fink, M. (1999). A solution to diffraction biases in sonoelasticity: the acoustic impulse technique. *The Journal of the Acoustical Society of America*, *105*(5), 2941-2950.

Catheline, S., Gennisson, J. L., Delon, G., Fink, M., Sinkus, R., Abouelkaram, S., & Culioli, J. (2004). Measurement of viscoelastic properties of homogeneous soft solid using transient elastography: An inverse problem approach. *The Journal of the Acoustical Society of America*, *116*(6), 3734-3741.

Cattoni, D. I., Chara, O., Kaufman, S. B., & González Flecha, F. L. (2015). Cooperativity in binding processes: new insights from phenomenological modeling. *PLoS One*, *10*(12), e0146043.

Chen, X., Sanchez, G. N., Schnitzer, M. J., & Delp, S. L. (2020). Microendoscopy detects altered muscular contractile dynamics in a mouse model of amyotrophic lateral sclerosis. *Scientific Reports*, *10*(1), 457.

Cnockaert, J. C., Lensel, G., & Pertuzon, E. (1975). Relative contribution of individual muscles to the isometric contraction of a muscular group. *Journal of biomechanics*, *8*(3-4), 191-197.

Courage, W. (2003). inventor; Courage, Khazaka Electronic GmbH, assignee. Measuring device for measuring the elastic properties of a surface structure. *United States patent US*, *6619423*.

Creze, M., Nordez, A., Soubeyrand, M., Rocher, L., Maître, X., & Bellin, M. F. (2018). Shear wave sonoelastography of skeletal muscle: basic principles, biomechanical concepts, clinical applications, and future perspectives. *Skeletal radiology*, *47*, 457-471.

Cui, L., Perreault, E. J., Maas, H., & Sandercock, T. G. (2008). Modeling short-range stiffness of feline lower hindlimb muscles. *Journal of biomechanics*, *41*(9), 1945-1952.

De Luca, C. J. (1997). The use of surface electromyography in biomechanics. *Journal of applied biomechanics*, *13*(2), 135-163.

Deffieux, T., Gennisson, J. L., Tanter, M., & Fink, M. (2008). Assessment of the mechanical properties of the musculoskeletal system using 2-D and 3-D very high frame rate ultrasound. *IEEE transactions on ultrasonics, ferroelectrics, and frequency control*, *55*(10), 2177-2190.

Deffieux, T., Montaldo, G., Tanter, M., & Fink, M. (2009). Shear wave spectroscopy for in vivo quantification of human soft tissues visco-elasticity. *IEEE transactions on medical imaging*, *28*(3), 313-322.

Desplantez, A., Cornu, C., & Goubel, F. (1999). Viscous properties of human muscle during contraction. *Journal of biomechanics*, *32*(6), 555-562.

Destrade, M., Gilchrist, M. D., & Saccomandi, G. (2010). Third-and fourth-order constants of incompressible soft solids and the acousto-elastic effect. *The Journal of the Acoustical Society of America*, *127*(5), 2759-2763.

Dickinson, R. J., & Hill, C. R. (1982). Measurement of soft tissue motion using correlation between A-scans. *Ultrasound in medicine & biology*, *8*(3), 263-271.

Doheny, E. P., Lowery, M. M., FitzPatrick, D. P., & O'Malley, M. J. (2008). Effect of elbow joint angle on force–EMG relationships in human elbow flexor and extensor muscles. *Journal of electromyography and kinesiology*, *18*(5), 760-770.

Dresner, M. A., Rose, G. H., Rossman, P. J., Muthupillai, R., Manduca, A., & Ehman, R. L. (2001). Magnetic resonance elastography of skeletal muscle. *Journal of Magnetic Resonance Imaging*, *13*(2), 269-276.

RERERENCES

Eby, S. F., Song, P., Chen, S., Chen, Q., Greenleaf, J. F., & An, K. N. (2013). Validation of shear wave elastography in skeletal muscle. *Journal of biomechanics*, *46*(14), 2381-2387.

Edman, K. A., & Tsuchiya, T. (1996). Strain of passive elements during force enhancement by stretch in frog muscle fibres. *The Journal of physiology*, *490*(1), 191-205.

Edwards, R. G., & Lippold, O. C. J. (1956). The relation between force and integrated electrical activity in fatigued muscle. *The Journal of physiology*, *132*(3), 677.

Erdemir, A., McLean, S., Herzog, W., & van den Bogert, A. J. (2007). Model-based estimation of muscle forces exerted during movements. *Clinical biomechanics*, *22*(2), 131-154.

Fink, M., & Tanter, M. (2010). Multiwave imaging and super resolution. *Physics today*, *63*(2), 28-33.

Fjær, E., Holt, R. M., Horsrud, P., Raaen, A. M., & Risnes, R. (2008). Elasticity. *Developments in Petroleum Science*, *53*, 1-54.

Fung, Y. (1993). Biomechanics: mechanical properties of living tissues. *Springer-Verlag*, New York.

Gajdosik, R. L. (2001). Passive extensibility of skeletal muscle: review of the literature with clinical implications. *Clinical biomechanics*, *16*(2), 87-101.

Garner, B. A., & Pandy, M. G. (2003). Estimation of musculotendon properties in the human upper limb. *Annals of biomedical engineering*, *31*, 207-220.

Gennisson, J. L., Catheline, S., Chaffaı, S., & Fink, M. (2003). Transient elastography in anisotropic medium: application to the measurement of slow and fast shear wave speeds in muscles. *The Journal of the Acoustical Society of America*, *114*(1), 536-541.

Gennisson, J. L., Cornu, C., Catheline, S., Fink, M., & Portero, P. (2005). Human muscle hardness assessment during incremental isometric contraction using transient elastography. *Journal of biomechanics*, *38*(7), 1543-1550.

Gennisson, J. L., Rénier, M., Catheline, S., Barrière, C., Bercoff, J., Tanter, M., & Fink, M. (2007). Acoustoelasticity in soft solids: Assessment of the nonlinear shear modulus with the acoustic radiation force. *The Journal of the Acoustical Society of America*, *122*(6), 3211-3219.

Gennisson, J. L., Deffieux, T., Macé, E., Montaldo, G., Fink, M., & Tanter, M. (2010). Viscoelastic and anisotropic mechanical properties of in vivo muscle tissue assessed by supersonic shear imaging. *Ultrasound in medicine & biology*, *36*(5), 789-801.

Gennisson, J. L., Deffieux, T., Fink, M., & Tanter, M. (2013). Ultrasound elastography: principles and techniques. *Diagnostic and interventional imaging*, *94*(5), 487-495.

Giat, Y., Mizrahi, J., Levine, W. S., & Chen, J. (1994). Simulation of distal tendon transfer of the biceps brachii and the brachialis muscles. *Journal of biomechanics*, *27*(8), 1005-1014.

Gordon, A. M., Huxley, A. F., & Julian, F. J. (1966). The variation in isometric tension with sarcomere length in vertebrate muscle fibres. *The Journal of physiology*, *184*(1), 170-192.

Granzier, H. L., Akster, H. A., & Ter Keurs, H. E. (1991). Effect of thin filament length on the force-sarcomere length relation of skeletal muscle. *American Journal of Physiology-Cell Physiology*, *260*(5), C1060-C1070.

Greene, L. E., & Eisenberg, E. (1980). Cooperative binding of myosin subfragment-1 to the actin-troponin-tropomyosin complex. *Proceedings of the National Academy of Sciences*, *77*(5), 2616-2620.

Greene, L. E., & Eisenberg, E. (1988). Relationship between regulated actomyosin ATPase activity and cooperative binding of myosin to regulated actin. *Cell biophysics*, *12*, 59-71.

Greenleaf, J. F., & Alizad, A. (2017). Viscoelastic tissue characteristics measured by ultrasound. In *Optical Elastography and Tissue Biomechanics IV* (p. 1006705). SPIE.

Grinspan, G. A., Aguiar, S., & Benech, N. (2016). Optimization of a surface wave elastography method through diffraction and guided waves effects characterization. *Journal of Physics: Conference Series, 705*(1), 012014.

Grinspan, G.A. “Propiedades biomecánicas del músculo esquelético evaluadas mediante elastografía por ondas de superficie”. Tesis de Maestría, Laboratorio de Acústica Ultrasonora, Univ. De la República-PEDECIBA, Montevideo, Uruguay, 2019.

Grinspan, G. A., Cabral, H. V., de Souza, L. M., de Oliveira, L. F., Aguiar, S., Blanco, E., & Benech, N. (2021). Surface wave elastography is a reliable method to correlate muscle elasticity, torque, and electromyography activity level. *Physiological reports*, *9*(15), e14955.

Grinspan, G. A., Fernandes de Oliveira, L., Brandao, M. C., Pomi, A., & Benech, N. (2023). Load sharing between synergistic muscles characterized by a ligand-binding approach and elastography. *Scientific Reports*, *13*(1), 18267.

Grinspan, G. A., Oliveira, L. F. D., Brandao, M. C., & Benech, N. (2024). Widening the frontiers of elastography in biomechanics: simultaneous muscle elasticity measurements at high-sample rate with surface wave elastography. *Frontiers in Physics*, *12*, 1329296.

Guimaraes, A. C., Herzog, W., Hulliger, M., Zhang, Y. T., & Day, S. (1994). Effects of muscle length on the EMG–force relationship of the cat soleus muscle studied using non-periodic stimulation of ventral root filaments. *Journal of Experimental Biology*, 193(1), 49-64.

Guyton, A. C., Hall, J. E. (2016). Tratado de Fisiología Médica. Elsevier, España.

Hammer, Ø., & Harper, D. A. (2001). Past: paleontological statistics software package for educaton and data anlysis. *Palaeontologia electronica*, *4*(1), 1-9.

Hanney, W. J., Kolber, M. J., Salamh, P. A., Moise, S., Hampton, D., & Wilson, A. T. (2022). The Reliability of Tensiomyography for Assessment of Muscle Function in the Healthy Population: a systematic review. *Strength & Conditioning Journal*, *44*(6), 18-35.

Haselgrove, J. C. (1973). X-ray evidence for a conformational change in the actin-containing filaments of vertebrate striated muscle. In *Cold Spring Harbor Symposia on Quantitative Biology*, 37, 341-352.

Heintz, S. (2006). Muscular forces from static optimization. Doctoral Thesis. KTH, Stockholm, Sweden, 2006.

Henneman, E., Somjen, G., & Carpenter, D. O. (1965). Functional significance of cell size in spinal motoneurons. *Journal of neurophysiology*, *28*(3), 560-580.

Heckathorne, C. W., & Childress, D. S. (1981). Relationships of the surface electromyogram to the force, length, velocity, and contraction rate of the cineplastic human biceps1. *American Journal of Physical Medicine & Rehabilitation*, 60(1), 1-19.

Heckmatt, J. Z., Leeman, S., & Dubowitz, V. (1982). Ultrasound imaging in the diagnosis of muscle disease. *The Journal of pediatrics*, *101*(5), 656-660.

Heers, G., Jenkyn, T., Dresner, M.A., Klein, M.O., Basford J.R., Kaufman K.R., Ehman R.L., An K.N. (2003). Measurement of muscle activity with magnetic resonance elastography. *Clinical Biomechanics*, *18*(6), 537-542.

Heymsfield, S.B., Lohman, T., Wang, Z., Going, S. B. (2005). Human body composition. *Human Kinetics*, Champaign.

Hill, A. V. (1910). The possible effects of the aggregation of the molecules of hemoglobin on its dissociation curves. *j. physiol.*, *40*, iv-vii.

Hill, A. V. (1938). The heat of shortening and the dynamic constants of muscle. *Proceedings of the Royal Society of London. Series B-Biological Sciences*, *126*(843), 136-195.

Hill, A. V. (1949). The abrupt transition from rest to activity in muscle. *Proceedings of the Royal Society of London. Series B-Biological Sciences*, *136*(884), 399-420.

RERERENCES

Hill, A. V. (1951). The transition from rest to full activity in muscle: the velocity of shortening. *Proceedings of the Royal Society of London. Series B-Biological Sciences*, *138*(892), 329-338.

Hodges, P. W., Pengel, L. H. M., Herbert, R. D., & Gandevia, S. (2003). Measurement of muscle contraction with ultrasound imaging. *Muscle & Nerve*, *27*(6), 682-692.

Howard, J. D., Hoit, J. D., Enoka, R. M., & Hasan, Z. (1986). Relative activation of two human elbow flexors under isometric conditions: A cautionary note concerning flexor equivalence. *Experimental Brain Research*, 62, 199-202.

Hu, X., Murray, W. M., & Perreault, E. J. (2011). Muscle short-range stiffness can be used to estimate the endpoint stiffness of the human arm. *Journal of neurophysiology*, *105*(4), 1633-1641.

Hug, F., Turpin, N. A., Guével, A., & Dorel, S. (2010). Is interindividual variability of EMG patterns in trained cyclists related to different muscle synergies?. *Journal of applied physiology*, *108*(6), 1727-1736.

Hug, F., Tucker, K., Gennisson, J. L., Tanter, M., & Nordez, A. (2015a). Elastography for muscle biomechanics: toward the estimation of individual muscle force. *Exercise and sport sciences reviews*, *43*(3), 125-133.

Hug, F., Hodges, P. W., & Tucker, K. (2015b). Muscle force cannot be directly inferred from muscle activation: illustrated by the proposed imbalance of force between the vastus medialis and vastus lateralis in people with patellofemoral pain. *Journal of orthopaedic & Sports physical therapy*, *45*(5), 360-365.

Hui, F. C., Chao, E. Y., & An, K. N. (1978). Muscle and joint forces at the elbow during isometric lifting. *Orthop Trans*, *2*, 169.

Huijing, P. A. (1999). Muscle as a collagen fiber reinforced composite: a review of force transmission in muscle and whole limb. *Journal of biomechanics*, *32*(4), 329-345.

Huxley, A. F. (1957). Muscle structure and theories of contraction. *Progress in biophysics and biophysical chemistry*, *7*, 255-318.

Huxley, A. F., & Peachey, L. D. (1961). The maximum length for contraction in vertebrate striated muscle. *The Journal of physiology*, *156*(1), 150.

Huxley, A. F., & Simmons, R. M. (1971). Proposed mechanism of force generation in striated muscle. *Nature*, *233*(5321), 533-538.

Huxley, H. E. (1973). Structural changes in the actin-and myosin-eontaining filaments during contraction. In *Cold Spring Harbor Symposia on Quantitative Biology*, 37, 361-376.

Huxley, A. (1988). Muscular contraction. *Annual Review of Physiology*, *50*(1), 1-17.

RERERENCES

Jenkyn, T. R., Ehman, R. L., & An, K. N. (2003). Noninvasive muscle tension measurement using the novel technique of magnetic resonance elastography (MRE). *Journal of biomechanics*, *36*(12), 1917-1921.

Johnson, M., Polgar, J., Weightman, D., & Appleton, D. (1973). Data on the distribution of fibre types in thirty-six human muscles: an autopsy study. *Journal of the neurological sciences*, *18*(1), 111-129.

Kawakami, Y., Ichinose, Y., & Fukunaga, T. (1998). Architectural and functional features of human triceps surae muscles during contraction. *Journal of applied physiology*, *85*(2), 398-404.

Kazakov, V. V., & Klochkov, B. N. (1989). Low frequency mechanical properties of the soft tissue of the human arm. *Biophysics*, *34*(4), 742-747.

Kernel, D. (1986). Organization and properties of spinal motoneurones and motor units. *Progress in brain research*, *64*, 21-30.

Keuler, E. M., Loegering, I. F., Martin, J. A., Roth, J. D., & Thelen, D. G. (2019). Shear wave predictions of achilles tendon loading during human walking. *Scientific Reports*, *9*(1), 13419.

Kijanka, P., Qiang, B., Song, P., Carrascal, C. A., Chen, S., & Urban, M. W. (2018). Robust phase velocity dispersion estimation of viscoelastic materials used for medical applications based on the multiple signal classification method. *IEEE transactions on ultrasonics, ferroelectrics, and frequency control*, *65*(3), 423-439.

Kutch, J. J., & Valero-Cuevas, F. J. (2011). Muscle redundancy does not imply robustness to muscle dysfunction. *Journal of biomechanics*, *44*(7), 1264-1270.

Labeit, D., Watanabe, K., Witt, C., Fujita, H., Wu, Y., Lahmers, S., Funck, T., Labeit, S., Granzier, H. (2003). Calcium-dependent molecular spring elements in the giant protein titin. *Proceedings of the National Academy of Sciences*, *100*(23), 13716-13721.

Lacourpaille, L., Nordez, A., Hug, F., Couturier, A., Dibie, C., & Guilhem, G. (2014). Time-course effect of exercise-induced muscle damage on localized muscle mechanical properties assessed using elastography. *Acta physiologica*, *211*(1), 135-146.

Lamb, H. (1917). On waves in an elastic plate. *Proceedings of the Royal Society of London. Series A*, *93*(648), 114-128.

Landau, L., Lifshitz, E. (1970). Theory of elasticity. *Pergamon Press*, New York.

Lapole, T., Tindel, J., Galy, R., & Nordez, A. (2015). Contracting biceps brachii elastic properties can be reliably characterized using supersonic shear imaging. *European journal of applied physiology*, *115*, 497-505.

Lawrence, J. H., & De Luca, C. J. (1983). Myoelectric signal versus force relationship in different human muscles. *Journal of Applied Physiology*, *54*(6), 1653-1659.

Le Sant, G., Ates, F., Brasseur, J. L., & Nordez, A. (2015). Elastography study of hamstring behaviors during passive stretching. *PloS one*, *10*(9), e0139272.

Lehman, W. (2017). Switching muscles on and off in steps: The McKillop-Geeves three-state model of muscle regulation. *Biophysical Journal*, *112*(12), 2459-2466.

Lehrer, S. S., & Morris, E. P. (1982). Dual effects of tropomyosin and troponin-tropomyosin on actomyosin subfragment 1 ATPase. *Journal of Biological Chemistry*, *257*(14), 8073-8080.

Lehrer, S. S., & Geeves, M. A. (1998). The muscle thin filament as a classical cooperative/allosteric regulatory system. *Journal of molecular biology*, *277*(5), 1081-1089.

Lexell, J., Downham, D., & Sjöström, M. (1984). Distribution of different fibre types in human skeletal muscles: A statistical and computational study of the fibre type arrangement in m. vastus lateralis of young, healthy males. *Journal of the neurological sciences*, *65*(3), 353-365.

Lexell, J., Downham, D., & Sjöström, M. (1986). Distribution of different fibre types in human skeletal muscles: fibre type arrangement in m. vastus lateralis from three groups of healthy men between 15 and 83 years. *Journal of the neurological sciences*, *72*(2-3), 211-222.

Lieber, R. L., Fazeli, B. M., & Botte, M. J. (1990). Architecture of selected wrist flexor and extensor muscles. *The Journal of hand surgery*, *15*(2), 244-250.

Lieber, R. L., Jacobson, M. D., Fazeli, B. M., Abrams, R. A., & Botte, M. J. (1992). Architecture of selected muscles of the arm and forearm: anatomy and implications for tendon transfer. *The Journal of hand surgery*, *17*(5), 787-798.

Linke, W. A., Ivemeyer, M., Olivieri, N., Kolmerer, B., Rüegg, C. J., & Labeit, S. (1996). Towards a molecular understanding of the elasticity of titin. *Journal of molecular biology*, *261*(1), 62-71.

Lloyd, D. G., & Besier, T. F. (2003). An EMG-driven musculoskeletal model to estimate muscle forces and knee joint moments in vivo. *Journal of biomechanics*, *36*(6), 765-776.

Luh, J. J., Chang, G. C., Cheng, C. K., Lai, J. S., & Kuo, T. S. (1999). Isokinetic elbow joint torques estimation from surface EMG and joint kinematic data: using an artificial neural network model. *Journal of electromyography and kinesiology*, *9*(3), 173-183.

Lymn, R. W., & Taylor, E. W. (1971). Mechanism of adenosine triphosphate hydrolysis by actomyosin. *Biochemistry*, *10*(25), 4617-4624.

RERERENCES

Maganaris, C. N. (2003). Force-length characteristics of the in vivo human gastrocnemius muscle. *Clinical Anatomy*, *16*(3), 215-223.

Magnusson, S. P. (1998). Passive properties of human skeletal muscle during stretch maneuvers. *Scandinavian journal of medicine & science in sports*, *8*(2), 65-77.

Mannarino, P., Matta, T. T. D., & Oliveira, L. F. D. (2019). An 8-week resistance training protocol is effective in adapting quadriceps but not patellar tendon shear modulus measured by Shear Wave Elastography. *PLoS One*, *14*(4), e0205782.

Marchese, S. S., Di Bella, P., Sessa, E., Donato, S., & Bramanti, P. (2001). The spasticity evaluation test (SeT): a pilot study. *Journal of Rehabilitation Research & Development*, *38*(1).

Martin, J.A., Brandon, S.C., Keuler, E.M., Hermus, J.R., Ehlers, A.C., Segalman, D.J., Allen, M.S., Thelen, D.G. (2018). Gauging force by tapping tendons. *Nature communications*, *9*(1), 1592.

Menegaldo, L. L., de Oliveira, L. F., & Minato, K. K. (2014). EMGD-FE: an open source graphical user interface for estimating isometric muscle forces in the lower limb using an EMG-driven model. *Biomedical engineering online*, *13*(1), 1-12.

Messier, R. H., Duffy, J. A., Litchman, H. M., Paslay, P. R., Soechting, J. F., & Stewart, P. A. (1971). The electromyogram as a measure of tension in the human biceps and triceps muscles. *International Journal of Mechanical Sciences*, *13*(7), 585-598.

Mijailovich, S. M., Stojanovic, B., Nedic, D., Svicevic, M., Geeves, M. A., Irving, T. C., & Granzier, H. L. (2019). Nebulin and titin modulate cross-bridge cycling and length-dependent calcium sensitivity. *Journal of General Physiology*, *151*(5), 680-704.

Miller, G. F., & Pursey, H. (1954). The field and radiation impedance of mechanical radiators on the free surface of a semi-infinite isotropic solid. *Proceedings of the Royal Society of London. Series A*, *223*(1155), 521-541.

Murray, W. M., Delp, S. L., & Buchanan, T. S. (1995). Variation of muscle moment arms with elbow and forearm position. *Journal of biomechanics*, *28*(5), 513-525.

Murray, W. M., Buchanan, T. S., & Delp, S. L. (2002). Scaling of peak moment arms of elbow muscles with upper extremity bone dimensions. *Journal of biomechanics*, *35*(1), 19-26.

Mutungi, G., & Ranatunga, K. W. (1996). The visco-elasticity of resting intact mammalian (rat) fast muscle fibres. *Journal of Muscle Research & Cell Motility*, *17*, 357-364.

Nicol, A. C. Elbow joint prosthesis design, biomechanical aspects. Doctoral Thesis, University of Strathclyde, 1977.

RERERENCES

Nishikawa, K. (2020). Titin: a tunable spring in active muscle. *Physiology*, *35*(3), 209-217.

Nordez, A., Gennisson, J. L., Casari, P., Catheline, S., & Cornu, C. (2008). Characterization of muscle belly elastic properties during passive stretching using transient elastography. *Journal of biomechanics*, *41*(10), 2305-2311.

Nordez, A., Guével, A., Casari, P., Catheline, S., & Cornu, C. (2009). Assessment of muscle hardness changes induced by a submaximal fatiguing isometric contraction. *Journal of Electromyography and Kinesiology*, *19*(3), 484-491.

Nordez, A., & Hug, F. (2010). Muscle shear elastic modulus measured using supersonic shear imaging is highly related to muscle activity level. *Journal of applied physiology*, *108*(5), 1389-1394.

O'Donnell, M., & Skovoroda, A. R. (2004). Prospects for elasticity reconstruction in the heart. *ieee transactions on ultrasonics, ferroelectrics, and frequency control*, *51*(3), 322-328.

Ophir, J., Cespedes, I., Ponnekanti, H., Yazdi, Y., & Li, X. (1991). Elastography: a quantitative method for imaging the elasticity of biological tissues. *Ultrasonic imaging*, *13*(2), 111-134.

Pauwels, F., Biomechanics of the Locomotor Apparatus. (1980). *Springer-Verlag*, Berlin, Heidelberg, New York, 1980.

Pillen, S., Tak, R. O., Zwarts, M. J., Lammens, M. M., Verrijp, K. N., Arts, I. M., van der Laak, J.A., Hoogerbrugge P. M., van Engelen B. G. M., & Verrips, A. (2009). Skeletal muscle ultrasound: correlation between fibrous tissue and echo intensity. *Ultrasound in medicine & biology*, *35*(3), 443-446.

Pillen, S., van Keimpema, M., Nievelstein, R. A., Verrips, A. A. D., van Kruijsbergen-Raijmann, W., & Zwarts, M. J. (2006). Skeletal muscle ultrasonography: visual versus quantitative evaluation. *Ultrasound in medicine & biology*, *32*(9), 1315-1321.

Pinniger, G. J., Ranatunga, K. W., & Offer, G. W. (2006). Crossbridge and non-crossbridge contributions to tension in lengthening rat muscle: force-induced reversal of the power stroke. *The Journal of physiology*, *573*(3), 627-643.

Popovic, G., Sarvazyan, A., Ponomarjev, V., & Vucelic, D. (1992). *U.S. Patent No. 5,115,808*. Washington, DC: U.S. Patent and Trademark Office.

Porter, M., & Weber, A. (1979). Non-cooperative response of actin-cystein 373 in cooperatively behaving regulated actin filaments. *FEBS letters*, *105*(2), 259-262.

Punkt, K. (2002). Fibre types in skeletal muscles. *Springer-Verlag*, Berlin, Heidelberg.

Qiang, B., Brigham, J. C., Aristizabal, S., Greenleaf, J. F., Zhang, X., & Urban, M. W. (2015). Modeling transversely isotropic, viscoelastic, incompressible tissue-like materials with application in ultrasound shear wave elastography. *Physics in Medicine & Biology*, *60*(3), 1289.

Rack, P. M. (1966). The behaviour of a mammalian muscle during sinusoidal stretching. *The journal of physiology*, *183*(1), 1-14.

Rack, P. M., & Westbury, D. R. (1974). The short range stiffness of active mammalian muscle and its effect on mechanical properties. *The Journal of physiology*, *240*(2), 331-350.

Ranatunga, K. W. (2001). Sarcomeric visco-elasticity of chemically skinned skeletal muscle fibres of the rabbit at rest. *Journal of Muscle Research & Cell Motility*, *22*(5), 399-414.

Ranatunga, K. W., Roots, H., Pinniger, G. J., Offer, G. W. (2010). Crossbridge and non-crossbridge contributions to force in shortening and lengthening muscle. *Muscle Biophysics: From Molecules to Cells*, 207-221.

Rao, V. S., Marongelli, E. N., & Guilford, W. H. (2009). Phosphorylation of tropomyosin extends cooperative binding of myosin beyond a single regulatory unit. *Cell motility and the cytoskeleton*, *66*(1), 10-23.

Raikova, R., & Aladjov, H. (2003). The influence of the way the muscle force is modeled on the predicted results obtained by solving indeterminate problems for a fast elbow flexion. *Computer Methods in Biomechanics and Biomedical Engineering*, *6*(3), 181-196.

Rassier, D. E., MacIntosh, B. R., & Herzog, W. (1999). Length dependence of active force production in skeletal muscle. *Journal of applied physiology*, *86*(5), 1445-1457.

Reimers, K., Reimers, C. D., Wagner, S., Paetzke, I., & Pongratz, D. E. (1993). Skeletal muscle sonography: a correlative study of echogenicity and morphology. *Journal of Ultrasound in Medicine*, *12*(2), 73-77.

Remeniéras, J. P., Bulot, M., Gennisson, J. L., Patat, F., Destrade, M., & Bacle, G. (2021). Acousto-elasticity of transversely isotropic incompressible soft tissues: Characterization of skeletal striated muscle. *Physics in Medicine & Biology*, *66*(14), 145009.

Reshetnyak, Y. K., Prudence, C. N., Segala, J., Markin, V. S., & Andreev, O. A. (2012). Parking problem and negative cooperativity of binding of myosin subfragment 1 to F-actin. *Biochemical and Biophysical Research Communications*, *425*(4), 746-749.

Reyes-Ferrada, W., Rodríguez-Perea, Á., Chirosa-Ríos, L., Martínez-García, D., & Jerez-Mayorga, D. (2022). Muscle quality and functional and conventional ratios of

trunk strength in young healthy subjects: a pilot study. *International journal of environmental research and public health*, *19*(19), 12673.

Romero, F., & Alonso, F. J. (2016). A comparison among different Hill-type contraction dynamics formulations for muscle force estimation. *Mechanical Sciences*, *7*(1), 19-29.

Roots, H., Offer, G. W., & Ranatunga, K. W. (2007). Comparison of the tension responses to ramp shortening and lengthening in intact mammalian muscle fibres: crossbridge and non-crossbridge contributions. *Journal of muscle research and cell motility*, *28*, 123-139.

Rose, J.L. (1999). Ultrasonic Waves in Solid Media.*Cambridge University Press*, New York.

Rosen, J., Fuchs, M. B., & Arcan, M. (1999). Performances of Hill-type and neural network muscle models—toward a myosignal-based exoskeleton. *Computers and Biomedical Research*, *32*(5), 415-439.

Rayleigh, L. (1888). On the free vibrations of an infinite plate of homogeneous isotropic elastic matter. *Proceedings of the London Mathematical Society*, *1*(1), 225-237.

Rouze, N. C., Knight, A. E., & Nightingale, K. R. (2021). Uniqueness of shear wave modeling in an incompressible, transversely isotropic (ITI) material. *Physics in Medicine & Biology*, *66*(21), 21NT04.

Royer, D., Deulesaint, E. (2000). Elastic waves in solids I: Free and guided propagation. *Springer Verlag*, Berlin.

Royston, T. J., Dai, Z., Chaunsali, R., Liu, Y., Peng, Y., & Magin, R. L. (2011). Estimating material viscoelastic properties based on surface wave measurements: A comparison of techniques and modeling assumptions. *The Journal of the Acoustical Society of America*, *130*(6), 4126-4138.

Rudenko, O. V., & Sarvazyan, A. P. (2014). Wave anisotropy of shear viscosity and elasticity. *Acoustical Physics*, *60*, 710-718.

Ryu, J., & Jeong, W. K. (2017). Current status of musculoskeletal application of shear wave elastography. *Ultrasonography*, *36*(3), 185.

Sabra, K. G., Conti, S., Roux, P., & Kuperman, W. A. (2007). Passive in vivo elastography from skeletal muscle noise. *Applied physics letters*, *90*(19).

Salman, M., & Sabra, K. G. (2013). Surface wave measurements using a single continuously scanning laser doppler vibrometer: application to elastography. *The Journal of the Acoustical Society of America*, *133*(3), 1245-1254.

RERERENCES

Sanchez, G. N., Sinha, S., Liske, H., Chen, X., Nguyen, V., Delp, S. L., & Schnitzer, M. J. (2015). In vivo imaging of human sarcomere twitch dynamics in individual motor units. *Neuron*, *88*(6), 1109-1120.

Sarvazyan, A. (1993). Shear acoustic properties of soft biological tissues in medical diagnostics. *The Journal of the Acoustical Society of America*, *93*(4_Supplement), 2329-2330.

Schöllhorn, W. I. (2004). Applications of artificial neural nets in clinical biomechanics. *Clinical Biomechanics*, *19*(9), 876-898.

Schröder, C. T., & Scott Jr, W. R. (2001). On the complex conjugate roots of the Rayleigh equation: The leaky surface wave. *The Journal of the Acoustical Society of America*, *110*(6), 2867-2877.

Seow, K. N., & Seow, C. Y. (2022). Molecular events of the crossbridge cycle reflected in the force–velocity relationship of activated muscle. *Frontiers in Physiology*, *13*, 846284.

Shao, Q., Bassett, D. N., Manal, K., & Buchanan, T. S. (2009). An EMG-driven model to estimate muscle forces and joint moments in stroke patients. *Computers in biology and medicine*, *39*(12), 1083-1088.

Shchepkin, D. V., Nabiev, S. R., Kopylova, G. V., Matyushenko, A. M., Levitsky, D. I., Bershitsky, S. Y., & Tsaturyan, A. K. (2017). Cooperativity of myosin interaction with thin filaments is enhanced by stabilizing substitutions in tropomyosin. *Journal of Muscle Research and Cell Motility*, *38*, 183-191.

Simpson, D. An examination of the design of an endoprosthesis for the elbow. Doctoral dissertation, M. Sc. Thesis. University of Strathclyde, Glasgow, 1975.

Šimunič, B., Degens, H., Rittweger, J., Narici, M., Mekjavic, I., & Pisot, R. (2011). Noninvasive estimation of myosin heavy chain composition in human skeletal muscle. *Medicine and science in sports and exercise*, *43*(9), 1619-1625.

Šimunič, B., Koren, K., Rittweger, J., Lazzer, S., Reggiani, C., Rejc, E., Pišot, R., Narici, M., & Degens, H. (2019). Tensiomyography detects early hallmarks of bed-rest-induced atrophy before changes in muscle architecture. *Journal of applied physiology*, *126*(4), 815-822.

Smart, R. R., Baudry, S., Fedorov, A., Kuzyk, S. L., & Jakobi, J. M. (2018). Influence of biceps brachii tendon mechanical properties on elbow flexor force steadiness in young and old males. *Scandinavian journal of medicine & science in sports*, *28*(3), 983-991.

Smith, D. R., Helm, C. A., Zonnino, A., McGarry, M. D., Johnson, C. L., & Sergi, F. (2023). Individual Muscle Force Estimation in the Human Forearm Using Multi-Muscle

MR Elastography (MM-MRE). *IEEE Transactions on Biomedical Engineering*, *70*(11), 3206-3215.

Solomonow, M., Guzzi, A. L., Baratta, R., Shoji, H., & d'Ambrosia, R. (1986). EMG-Force model of the elbows antagonistic muscle pair: The effect of joint position, gravity and recruitment. *American Journal of Physical Medicine & Rehabilitation*, 65(5), 223-244.

Solomonow, M., Baratta, R. V., & D'Ambrosia, R. (1991). EMG-force relations of a single skeletal muscle acting across a joint: Dependence on joint angle. *Journal of Electromyography and Kinesiology*, 1(1), 58-67.

Solomonow, M., Baratta, R., Bernardi, M., Zhou, B., Lu, Y., Zhu, M., & Acierno, S. (1994). Surface and wire EMG crosstalk in neighbouring muscles. *Journal of Electromyography and Kinesiology*, *4*(3), 131-142.

Spector, S. A., Gardiner, P. F., Zernicke, R. F., Roy, R. R., & Edgerton, V. R. (1980). Muscle architecture and force-velocity characteristics of cat soleus and medial gastrocnemius: implications for motor control. *journal of Neurophysiology*, *44*(5), 951-960.

Strang, G. (1988). Linear Algebra and its Applications. *Harcourt Brace Jovanovich Collage Publishers*, Orlando, Florida.

Takai, Y., Ohta, M., Akagi, R., Kanehisa, H., Kawakami, Y., & Fukunaga, T. (2009). Sit-to-stand test to evaluate knee extensor muscle size and strength in the elderly: a novel approach. *Journal of physiological anthropology*, *28*(3), 123-128.

Tanter, M., Bercoff, J., Athanasiou, A., Deffieux, T., Gennisson, J. L., Montaldo, G., ... & Fink, M. (2008). Quantitative assessment of breast lesion viscoelasticity: initial clinical results using supersonic shear imaging. *Ultrasound in medicine & biology*, *34*(9), 1373-1386.

Timoshenko, S. P. (1921). LXVI. On the correction for shear of the differential equation for transverse vibrations of prismatic bars. *The London, Edinburgh, and Dublin Philosophical Magazine and Journal of Science*, *41*(245), 744-746.

Timoshenko, S. P. (1922). X. On the transverse vibrations of bars of uniform cross-section. *The London, Edinburgh, and Dublin Philosophical Magazine and Journal of Science*, *43*(253), 125-131.

Tobacman, L. S., & Butters, C. A. (2000). A new model of cooperative myosin-thin filament binding. *Journal of Biological Chemistry*, *275*(36), 27587-27593.

Uffmann, K., Maderwald, S., Ajaj, W., Galban, C. G., Mateiescu, S., Quick, H. H., & Ladd, M. E. (2004). In vivo elasticity measurements of extremity skeletal muscle with MR elastography. *NMR in Biomedicine*, *17*(4), 181-190.

Valour, D., & Pousson, M. (2003). Compliance changes of the series elastic component of elbow flexor muscles with age in humans. *Pflügers Archiv*, *445*, 721-727.

Van Eesbeek, S., De Groot, J. H., Van der Helm, F. C., & De Vlugt, E. (2010). In vivo estimation of the short-range stiffness of cross-bridges from joint rotation. *Journal of biomechanics*, *43*(13), 2539-2547.

Wang, L., & Buchanan, T. S. (2002). Prediction of joint moments using a neural network model of muscle activations from EMG signals. *IEEE transactions on neural systems and rehabilitation engineering*, *10*(1), 30-37.

Weijs, W. A., & Hillen, B. (1985). Cross-sectional areas and estimated intrinsic strength of the human jaw muscles. *Acta morphologica neerlando-scandinavica*, *23*(3), 267-274.

Wells, J. B. (1965). Comparison of mechanical properties between slow and fast mammalian muscles. *The Journal of Physiology*, *178*(2), 252-269.

Wyman, J., & Gill, S. J. (1990). *Binding and linkage: functional chemistry of biological macromolecules*. *University Science Books*.

Yamaguchi, G. T., Moran, D. W., & Si, J. (1995). A computationally efficient method for solving the redundant problem in biomechanics. *Journal of biomechanics*, *28*(8), 999-1005

Yoshitake, Y., Takai, Y., Kanehisa, H., & Shinohara, M. (2014). Muscle shear modulus measured with ultrasound shear-wave elastography across a wide range of contraction intensity. *Muscle & nerve*, *50*(1), 103-113.

Zajac, F. E. (1989). Muscle and tendon: properties, models, scaling, and application to biomechanics and motor control. *Critical reviews in biomedical engineering*, *17*(4), 359-411.

Zatsiorsky, V.M., Prilutsky, B.I. (2012). Biomechanics of Skeletal Muscles. *Human Kinetics*, Champaign.

Zhang, X., & Greenleaf, J. F. (2007). Estimation of tissue's elasticity with surface wave speed. *The Journal of the Acoustical Society of America*, *122*(5), 2522-2525.

Zhang, X., Qiang, B., & Greenleaf, J. (2011a). Comparison of the surface wave method and the indentation method for measuring the elasticity of gelatin phantoms of different concentrations. *Ultrasonics*, *51*(2), 157-164.

Zhang, X., Qiang, B., Hubmayr, R. D., Urban, M. W., Kinnick, R., & Greenleaf, J. F. (2011b). Noninvasive ultrasound image guided surface wave method for measuring the wave speed and estimating the elasticity of lungs: A feasibility study. *Ultrasonics*, *51*(3), 289-295.

RERERENCES

Zhang, X. (2016). Identification of the Rayleigh surface waves for estimation of viscoelasticity using the surface wave elastography technique. *The Journal of the Acoustical Society of America*, *140*(5), 3619-3622.

Zhang, X., Osborn, T., Zhou, B., Meixner, D., Kinnick, R. R., Bartholmai, B., Greenleaf, J. F., Kalra, S. (2017). Lung ultrasound surface wave elastography: a pilot clinical study. *IEEE transactions on ultrasonics, ferroelectrics, and frequency control*, *64*(9), 1298-1304.

Zhao, Y., Ding, S., & Todoh, M. (2022). Validate the force-velocity relation of the Hill's muscle model from a molecular perspective. *Frontiers in Bioengineering and Biotechnology*, *10*, 1006571.

Zhou, P., & Rymer, W. Z. (2004). Factors governing the form of the relation between muscle force and the EMG: a simulation study. *Journal of neurophysiology*, *92*(5), 2878-2886.

Zimmer, M., Kleiser, B., Marquetand, J., & Ateş, F. (2023). Shear wave elastography characterizes passive and active mechanical properties of biceps brachii muscle in vivo. *Journal of the Mechanical Behavior of Biomedical Materials*, *137*, 105543.

Zonnino, A., Smith, D. R., Delgorio, P. L., Johnson, C. L., & Sergi, F. (2019). MM-MRE: a new technique to quantify individual muscle forces during isometric tasks of the wrist using MR elastography. In *2019 IEEE 16th International Conference on Rehabilitation Robotics (ICORR)*, 270-275.

Zot, H. G., Hasbun, J. E., & Van Minh, N. (2009). Striated muscle regulation of isometric tension by multiple equilibria. *PloS one*, *4*(12), e8052.

APPENDICES

1 – QUANTITATIVE METHODS FOR THE RECEPTOR-LIGAND SYSTEMS ANALYSIS

A. Linearization methods for rectangular hyperbolas

As we have seen in Section 3.1 of Chapter 3, the simplest ligand binding scheme for an unsaturated molecular receptor and its corresponding saturation fraction can be represented as follows:

$$R + L \rightleftharpoons RL \implies K_a = \frac{[RL]}{[R][L]} = \frac{1}{K_d} \qquad (3.13)$$

$$Y = \frac{occupied\ sites}{total\ sites} = \frac{[RL]}{[R] + [RL]} \qquad (3.14)$$

Note that from Eqs. (3.13) and (3.14) Y can be written in terms of K_a or K_d by substituting $[RL]$ accordingly:

$$Y = \frac{K_a[L]}{K_a[L] + 1} = \frac{[L]}{K_d + [L]} \qquad (A.1.1)$$

where $K_a = 1/K_d$, being K_d the dissociation constant. On the other hand, in Section 3.2 of Chapter 3, we showed that Y corresponds to the $C(\tau)$ coefficient in the skeletal muscle. In this sense, Eq. (A.1.1) can be written in terms of such coefficients as:

$$C = \frac{\tau}{K_d + \tau} \qquad (A.1.2)$$

A denoted in Figure 3.2 of Chapter 3, a molecular receptor presents hyperbolic ligand-binding dynamics when its saturation curve describes a rectangular hyperbola. Thus, as is done in molecular receptors from $Y(L)$ data, to effectively determine the presence of this type of ligand-binding behavior in skeletal muscle, the following

linearization methods can be applied from experimental values of $C(\tau)$ (Figure A.1) (Wyman & Gill. 1990).

Lineweaver-Burk (LB): $1/C$ *vs.* $1/\tau$

$$\frac{1}{C} = \frac{K_d + \tau}{\tau} = \frac{K_d}{\tau} + 1 \qquad \text{(A. 1.3)}$$

Therefore, if $C(\tau)$ is a rectangular hyperbola, the LB linearization gives a straight line with slope K_d and independent term 1.

Langmuir-Hanes (LH): τ/C *vs.* τ

$$\frac{\tau}{C} = \frac{\tau(K_d + \tau)}{\tau} = K_d + \tau \qquad \text{(A. 1.4)}$$

As follow from the above, if $C(\tau)$ is a rectangular hyperbola, the LH linearization gives a straight line with slope 1 and K_d as independent term.

Scatchard (S): C *vs.* C/τ

$$C = \frac{\tau}{K_d + \tau} \rightarrow \frac{CK_d + C\tau}{\tau} = 1$$

$$\Rightarrow \quad C = \frac{-K_d C}{\tau} + 1 \qquad \text{(A. 1.5)}$$

Thus, if $C(\tau)$ is a rectangular hyperbola, the S linearization gives a straight line with slope $-\mathrm{K_d}$ and 1 as independent term.

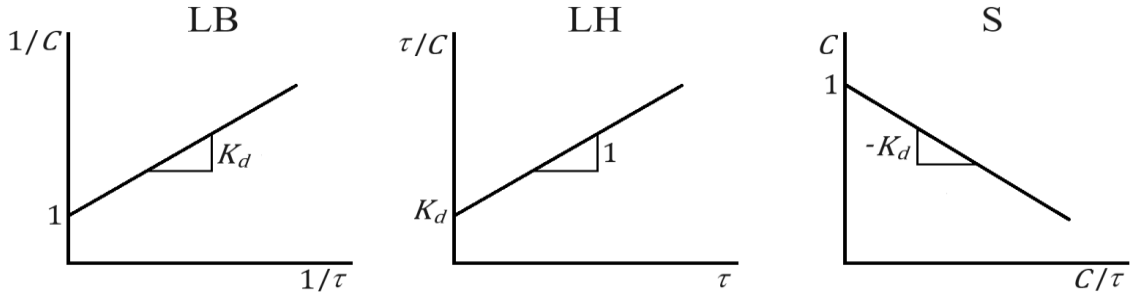

Figure A.1. Linearization methods for rectangular hyperbolic $\mathrm{C}(\tau)$ curves.

B. Hill plot for cooperative receptors

A cooperative molecular receptor typically exhibits the saturation curves shown in Figure 3.2 of Chapter 3. In this regard, the Hill plot offers a quantitative way to determine the presence of such ligand-binding behavior and classify the specific type of cooperativity involved (C+ or C-). According to the Hill model (Hill, 1910), a cooperative molecular receptor associates with its corresponding h ligands in a single step (concerted binding). The above can be represented through the following general ligand-binding scheme:

$$R + hL \rightleftharpoons RL_h \implies K_a = \frac{[RL_h]}{[R][L]^h} = \frac{1}{K_d} \qquad \text{(A. 1.6)}$$

$$Y = \frac{occupied\ sites}{total\ sites} = \frac{[RL_h]}{[R] + [RL_h]} \qquad \text{(A. 1.7)}$$

As we made for hyperbolic receptors, Y can be written in terms of K_a or K_d by substituting $[RL_n]$ of Eq. (A.1.6) into Eq. (A.1.7):

$$Y = \frac{K_a[L]^h}{K_a[L]^h + 1} = \frac{[L]^h}{K_d + [L]^h} \qquad \text{(A. 1.8)}$$

In turn, given the correspondence between Y and $C(\tau)$ (Ec. (3.15)) for skeletal muscle, the above can be written as:

$$C = \frac{\tau^h}{K_d + \tau^h} \qquad \text{(A. 1.9)}$$

From this point, the following transformations must be made:

$$\frac{1}{C} = \frac{K_d}{\tau^h} + 1$$

$$\rightarrow \frac{C}{1 - C} = \frac{\tau^h}{K_d} \qquad \text{(A. 1.10)}$$

Then, applying ln to both sides of Ec. (A.1.10) we obtain the characteristic equation of the Hill plot (Figure A.2):

$$ln\left(\frac{C}{1-C}\right) = ln\left(\frac{\tau^h}{K_d}\right) = hln(\tau) - ln(K_d) = hln(\tau) + ln\left(\frac{1}{K_d}\right) \qquad (A.1.11)$$

As seen, if $C(\tau)$ has a cooperative ligand-binding dynamics, the Hill plot is a straight line with slope h and $ln\left(\frac{1}{K_d}\right)$ as independent term. Particularly, h is termed as the *Hill number* (Wyman & Gill. 1990). Although it is well known that it actually does not correspond to the number of ligands interacting with the binding sites of the molecule, this parameter is very useful to classify the type of cooperativity as described in Figure 3.4 of Chapter 3.

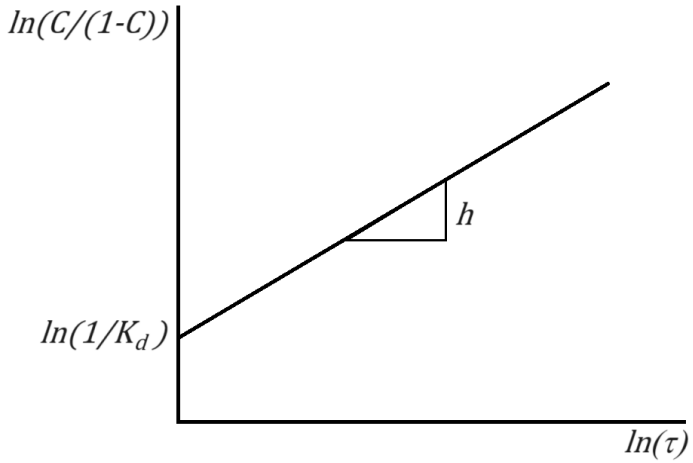

Figure A.2. Hill plot. Linearization method for cooperative C(τ) curves.

C. Determining the inflection point of the sigmoidal $C(\tau)$ curves

When a $C(\tau)$ curve corresponds to a C+ ligand-binding behavior, it exhibits a sigmoidal shape whose inflection point ($C^{\sim}$) can be informative regarding the kinetics of the underlying binding process. Such an inflection point can be calculated by solving the second derivative of Eq. (A.1.9):

$$C^{\sim} = \frac{d^2C(\tau)}{d\tau^2} = 0 \qquad (A.1.12)$$

To address the above, we first solve the first derivative of Eq. (A.1.9) as follows:

$$\frac{dC(\tau)}{d\tau} = \frac{h\tau^{h-1}(K_d + \tau^h) - h\tau^{h-1}(\tau^h)}{(K_d + \tau^h)^2} = \frac{hK_d\tau^{h-1}}{(K_d + \tau^h)^2} \qquad (A.1.13)$$

Then, the second derivative of Eq. (A.1.9) can be found by deriving the Eq. (A.1.13):

$$\frac{d^2C}{d\tau^2} = \frac{d}{dt}\left(\frac{dC(\tau)}{d\tau}\right) = \frac{hK_d(h-1)\tau^{h-2}(K_d + \tau^h)^2 - 2(K_d + \tau^h)^2 h\tau^{h-1}hK_d\tau^{h-1}}{(K_d + \tau^h)^4}$$

$$= \frac{hK_d(h-1)\tau^{h-2}(K_d + \tau^h) - 2h\left(\frac{\tau^{h-1}}{\tau}\right)hK_d\tau^{h-1}\tau}{(K_d + \tau^h)^4}$$

$$= \frac{hK_d(h-1)\tau^{h-2}(K_d + \tau^h) - 2h\tau^{h-2}hK_d\tau^h}{(K_d + \tau^h)^4}$$

$$= \frac{hK_d\tau^{h-2}((h-1)(K_d + \tau^h) - 2h\tau^h)}{(K_d + \tau^h)^4} \qquad (A.1.14)$$

As seen from the Eq. (A1.14), it is only necessary that the following term of the numerator be 0 to satisfy Eq. (A.1.12):

$$C^{\sim} = \frac{d^2C(\tau)}{d\tau^2} = 0 \Leftrightarrow \left((h-1)(K_d + \tau^h) - 2h\tau^h\right) = 0 \qquad (A.1.15)$$

Therefore, by solving the previous equation, it is possible to obtain Eq. (4.14), thus being possible to calculate $C^{\sim}$:

$$\left((h-1)(K_d + \tau^h) - 2h\tau^h\right) = (h-1)K_d + (h-1)\tau^h - 2h\tau^h$$

$$= (h-1)K_d - \left((h-1) - 2h\right)\tau^h = (h-1)K_d - (2h - h + 1)\tau^h$$

$$= (h-1)K_d - (h+1)\tau^h = 0$$

$$\Rightarrow \quad C^{\sim} = \sqrt[h]{\left(\frac{h-1}{h+1}\right)k_d} \qquad (4.14)$$

2 – DATA AVAILABILITY

The links below provide access to the experimental data set of the measurements that give rise to the results of Chapters 3, 4, and 5 of the present thesis:

- https://www.frontiersin.org/articles/10.3389/fphy.2024.1329296/full#supplementary-material

- https://static-content.springer.com/esm/art%3A10.1038%2Fs41598-023-45037-y/MediaObjects/41598_2023_45037_MOESM1_ESM.xlsx

3 – PUBLICATIONS

The links below provide access to the publications derived from this thesis:

- Grinspan, G. A., Fernandes de Oliveira, L., Brandao, M. C., Pomi, A., & Benech, N. (2023). Load sharing between synergistic muscles characterized by a ligand-binding approach and elastography. *Scientific Reports*, *13*(1), 18267.

https://www.nature.com/articles/s41598-023-45037-y

- Grinspan, G. A., Oliveira, L. F. D., Brandao, M. C., & Benech, N. (2024). Widening the frontiers of elastography in biomechanics: simultaneous muscle elasticity measurements at high-sample rate with surface wave elastography. *Frontiers in Physics*, *12*, 1329296.

https://www.frontiersin.org/journals/physics/articles/10.3389/fphy.2024.1329296/full

- Grinspan, G. A., Pomi, A., & Benech, N. (2024). A Possible Molecular Basis of the Change in Load Sharing Between Synergistic Muscles Characterized by Elastography. *IFMBE Proceedings*, 100, 86 - 89.

https://link.springer.com/chapter/10.1007/978-3-031-49407-9_9

- Grinspan, G. A., de Oliveira, L. F., Brandao, M. C., & Benech, N. (2024, May). An Elastography-Driven Biomechanical Model for Individual Muscle Force Estimation. In *2024 IEEE UFFC Latin America Ultrasonics Symposium (LAUS)* (pp. 1-4). IEEE.

https://ieeexplore.ieee.org/document/10553215